國 立 交 通 大 學

光 電 工 程 學 系 博 士 班

博 士 論 文

原子層沉積法成長單晶氧化鋅薄膜

之光學與晶體結構特性研究

Optical and Structural Properties of ZnO Epitaxial Films Grown

by Atomic Layer Deposition

研 究 生：楊松

指導教授：謝文峰 教授

中 華 民 國 一 0 一 年 十 二 月

原子層沉積法成長單晶氧化鋅薄膜

之光學與晶體結構特性研究

Optical and Structural Properties ZnO Epitaxial Films Grown by Atomic Layer Deposition

研 究 生：楊松　　Student：Song Yang

指導教授：謝文峰　　Advisor：Dr. Weng-Feng Hsieh

國 立 交 通 大 學

光電工程學系博士班

博 士 論 文

A Dissertation

Submitted to Department of Photonics and Institute of Electro-Optical Engineering

College of Electrical Engineering and Computer Science

National Chiao Tung University

In Partial Fulfillment of the Requirements

For the Degree of

Doctor of Philosophy

in

Electro-Optical Engineering

December 2012

Hsinchu, Taiwan, Republic of China

中華民國一百零一年十二月

原子層沉積法成長單晶氧化鋅薄膜之光學與晶體結構特性研究

研究生: 楊松　　　　　　　　　　指導教授: 謝文峰

國立交通大學光電工程學系博士班

摘要

我們成功地利用原子層沉積法成長纖維鋅礦結構單晶氧化鋅薄膜於 *c*-plane 與 *m*-plane 藍寶石基板，並且利用 X-ray 繞射與穿遂式電子顯微鏡研究其晶體結構特性。　經過高溫退火處理之後的氧化鋅單晶薄膜，其晶體品質顯示明顯的改進，並發現基面堆疊缺陷(basal stacking fault)為其主要的晶體結構缺陷。我們在 *c*-plane 藍寶石基板上成長出單晶氧化鋅薄膜，其磊晶面關係為 $(0001)\{10\bar{1}0\}_{ZnO} \parallel (0001)\{10\bar{1}0\}_{Al_2O_3}$；而在 *m*-plane 藍寶石基板上之磊晶面關係為 $(10\bar{1}0)<0001>_{ZnO} \parallel (10\bar{1}0)<\bar{1}2\bar{1}0>_{Al_2O_3}$。以光激螢光光譜觀察到以 3.325 eV 為中心的主要發光波段，可能來自於基面堆疊缺陷。由於基面堆疊缺陷的原子結構可視為一層非常薄的閃鋅礦晶體內嵌在纖維鋅礦結構之中，形成的基面堆疊缺陷量子井結構。我們也研究了熱退火處理對單晶氧化鋅薄膜的晶體結構特性和發光特性所造成的影響。另外，我們也透過時間解析光激螢光實驗來測定此基面堆疊缺陷量子井結構的發光機制與近能帶間隙發光的特性。我們觀察到光激載子被基面堆疊缺陷量子井結構局限後，形成量子局限激子。而此量子局限激子更持續地受到由許多局限能態所形成的局限效應所束縛。這些局限

能態可能是由隨機分佈的基面堆疊缺陷之間的量子耦合效應所形成；量子耦合效應是由於局限在不同量子井中的電子之間發生波函數交疊的關係，此現象亦形成了局限能態。由於測得的氧化鋅薄膜的低施子濃度以及近能帶能隙發光並無激子遷移的現象，所以我們排除了靠近基面堆疊缺陷的施子以及離子成份濃度擾動這兩個因素形成局限能態的可能性。

Optical and Structural Properties of ZnO Epitaxial Films Grown by Atomic Layer Deposition

Student: Song Yang   Advisor: Wen-Feng Hsieh

Department of Photonics and Institute of Electro-Optical Engineering

National Chiao Tung University

Abstract

We have successfully grown mono-crystalline ZnO epitaxial films on *c*-plane and *m*-plane sapphire substrates by using the atomic layer deposition. X-ray diffraction and transmission electron microscopy were employed to verify the structural properties of the ZnO thin films. The structure of the ZnO epi-films exhibits significantly improvement upon thermal annealing and intrinsic types of basal plane stacking faults (BSFs) are the predominant structural defects in the ZnO films after thermal treatment. The ZnO epi-films grown on the *c*-plane and *m*-plane sapphires have the epitaxial relationships of $(0001)\{10\bar{1}0\}_{ZnO} \parallel (0001)\{10\bar{1}0\}_{Al_2O_3}$ and $(10\bar{1}0)<0001>_{ZnO} \parallel (10\bar{1}0)<\bar{1}2\bar{1}0>_{Al_2O_3}$, respectively. The BSF is found to contribute to the emission at 3.325 eV in the photoluminescence (PL) spectra of the annealed ZnO films. This is attributed to quantum-well (QW) structure formed by

the BSF, which has the thin layer of zinc blend structure embedded in the wurtzite structure ZnO layer. The influence of thermal annealing to the structural and optical properties of the ZnO epi-films was also investigated. Through the time-resolved PL, we determined the decay times of the BSF related emission and the near-band-edge (NBE) emission. The QWs formed by the BSFs are found to trap the carriers to form BSF-bound excitons. The PL measurements revel that the BSF-bound excitons are influenced by the localization effect, which consists of localization states, and these bound excitons migrate among these localization states. Such localization states are attributed to the quantum coupling effect among the random distributed BSFs; the quantum coupling effect results from the wave function overlapping of the electrons bound in QWs and leads to the localization states. Because of the obtained low donor concentration and near band emission without the phenomenon of exciton migration, we exclude the donors in the vicinity of BSFs and the alloy density fluctuation from the origins of these localization states.

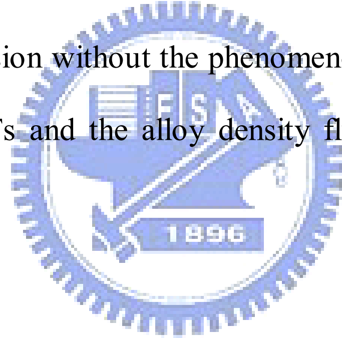

Acknowledgement

在學校攻讀碩博士學位的這一段歷程裡，感謝我的指導教授謝文峰老師這一路上的耐心支援與指導，讓我在尋找題目、實驗與理論探討的過程當中學習到很多。也感謝徐嘉鴻老師在同步輻射資源上的支援與 X-ray 實驗與理論上的指導，讓學生得以在晶體材料的研究上有著非常大的幫助。也感謝口試委員們對的指正與建議，使本論文更臻完善，也讓我對於研究的未來的方向有更進一步的想法與做法。也感謝實驗室裡面的伙伴們長久以來的互相支持，並一起渡過了大大小小像是工安環安的難關。感謝阿政學長的大力幫忙，還在關鍵時刻從瑞典帶回來了珍貴的量測資料，幫助我通過最後的畢業門檻。這一段艱辛的過程之中，也非常感謝黃董、維仁、至賢、智章學長們從碩士班以來這一段時間裡無數的討論、大餐、咖啡、是非與八卦，讓我在課業繁忙之餘培養了許多興趣與嗜好，並讓我不負菸酒生的威名。小郭、碧軒、厚仁、智雅，一起攻讀博士班的同伴們，在眼花撩亂的實驗室事務和實驗操作上給了我很多的幫忙。

我要感謝我的雙親，在這一路上無私的支持與鼓勵，讓我能夠在這漫長的求學過程中能夠得以持續的走下去。

最後感謝國科會的計劃，讓此論文得以順利的完成。

Table of Contents

Abstract in Chinese……………………………………………………………I
Abstract in English……………………………………………………………III
Acknowledgement………………………………………………………………V
Table of Contents………………………………………………………………VI
List of Figure Captions…………………………………………………………X
Chapter 1 Introduction…………………………………………………………1
1.1 Overview of ZnO……………………………………………………………1
1.1.1 ZnO Properties……………………………………………………………1
1.1.2 Growth of ZnO Thin Film………………………………………………3
1.2 Atomic Layer Deposition……………………………………………………3
1.2.1 Application of ALD………………………………………………………4
1.2.2 ZnO grown by ALD………………………………………………………5
1.3 Motivation……………………………………………………………………5
1.3.1 The Growth Mechanism of the ALD Reaction…………………………6
1.3.2 Epitaxial Growth of Polar and Non-Polar ZnO Films…………………6
1.3.3 Research of the Basal Stacking Faults in Wurtzite ZnO………………8
1.4 Organization of this Dissertation……………………………………………8

Chapter 2 Theoretical Background……………………………………………12
2.1 Atomic Layer Deposition Growth Mechanism………………………………12
2.2 Photoluminescence of ZnO…………………………………………………14
2.2.1 Free Exciton (FX)…………………………………………………………14

2.2.2 Bound Exciton Complex..15

2.2.3 Basal Stacking Faults Emission..16

2.3 XRD Measurement..17

2.3.1 X-ray Diffraction Theory..17

2.3.2 Radial Scan..19

2.3.3 Rocking Curve..20

2.3.4 Azimuthal Scan..21

2.3.5 X-ray Reflectivity..22

2.4 Transmission Electron Microscope..24

2.4.1 TEM setup..25

2.4.2 Dark Field Imagination..26

2.4.3 Basal Stacking Fault Analysis by TEM..27

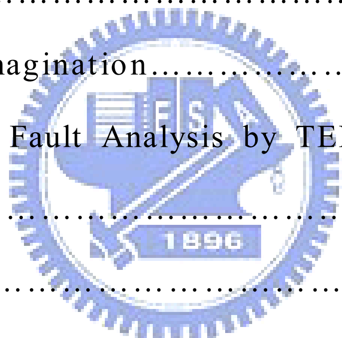

2.5 AFM..30

Chapter 3 Experiments..33

3.1 Atomic Layer Deposition System and Growth Procedure..33

3.2 X-ray Diffraction..33

3.3 Atomic Force Microscope..34

3.4 Transmission Electron Microscopy..35

3.5 Photoluminescence..36

3.5.1 Low Temperature Photoluminescence..36

3.5.2 Time Resolved Photoluminescence Measurement..37

Chapter 4 *C*-plane ZnO grown on *c*-plane Sapphire by ALD..39

4.1 XRD Measurements..39

4.1.1 $2\theta/\theta$ Scan..39

4.1.2 ω-rocking Curve..41

4.1.3 Azimuthal Cone Scans..43

4.2 TEM Analysis..46

4.3 AFM Measurements...50

4.4 Photoluminescence...51

4.4.1 Temperature Dependent Photoluminescence..........................53

4.4.2 Power Dependent Photoluminescence..................................56

4.5 Conclusions..58

Chapter 5 *m*-plane ZnO grown on *m*-plane Sapphire by ALD 65

5.1 XRD measurements...66

5.1.1 2θ/θ scan and ω-rocking curve..66

5.1.2 Azimuthal cone scans..68

5.1.3 X-ray Reflectivity...70

5.2 TEM...71

5.2.1 Cross Section Images with Zone Axis $[\bar{1}2\bar{1}0]_{ZnO}$ 71

5.2.2 Cross Section Images with Zone Axis $[0001]_{ZnO}$ 74

5.2.3 Fourier Filtered Images Analysis.....................................76

5.3 AFM...78

5.4 Photoluminescence...79

5.4.1 Low-Temperature Photoluminescence..................................79

5.4.2 Time-Resolved Photoluminescence....................................81

5.5 Conclusions..82

Chapter 6 Recombination dynamics of localized exciton in Basal Stacking Faults.........86

6.1 Temperature Dependent and Power Dependent Photoluminescence..............87

6.2 Time-Resolved Photoluminescence..89

6.3 Spectra Dependent Decay Times...91

6.4 Conclusions...97

Chapter 7 Conclusions and Prospective..100

7.1 Conclusions...100

7.2 Prospective...102

List of Figures

Figure 1-1 Stick and ball representations of three ZnO crystal structures……………………2

Figure 2-1 Schematics of one cycle of ALD growth steps……………………..…………..13

Figure 2-2 The schematic plot of the band alignment of ZnO at WZ/ZB/WZ regions…………..17

Figure 2-3 Bragg diffraction condition in real space and reciprocal space……………………18

Figure 2-4 The radial scan situation in the real space and reciprocal space……………………20

Figure 2-5 θ-rocking scan situations in the real and reciprocal spaces for ideal and non-ideal lattice structures……………………………………………………………………………21

Figure 2-6 Azimuthal angle scan situations in the real and reciprocal spaces for ideal and non-ideal lattice structures……………………………………………………………………22

Figure 2-7 X-ray reflectivity measurement of the thin film structure and the analysis of the obtained data………………………………………………………………………………23

Figure 2-8 Simulated XRR curves of the ZnO films on sapphire substrate with different R_{rms} values…………………………………………………………………………………..24

Figure 2-9 The measurement setup of TEM in bright field imaging and selected area diffraction modes………………..……………………………………………………………………26

Figure 2-10 The measurement setup of dark filed imaging with the selected spots with specific diffraction vector g……………..………………………………………………………27

Figure 2-11 Three kinds of planes with different atom stacking arrangements in ZnO material marked as A-, B-, and C- planes……………………………………………………………28

Figure 2-12 Four types of stacking faults in ZnO…………………...………………………29

Figure 2-13 The measurement setup of the atomic force microscope…………………………31

Figure 3-1 The four-circle diffractometer in NSRRC at beamline BL13A……………………34

Figure 3-2 Veeco Dimension 5000 Scanning Probe Microscope……….................…………...35

Figure 3-3 The TEM measurement instruments: the focused ion beam and Philips TECNAI-20 field emission gun type TEM……………………………………………………….…………36

Figure 3-4 The sketch of the photoluminescence measurement setup………………………37

Figure 3-5 The sketch of the TRPL measurement setup……………………………………….38

Figure 4-1 The radial scans (θ-2θ scan) along surface normal of the as-deposited and annealed ZnO films……………………………………………………………………………………40

Figure 4-2 The θ-rocking curves of the as-deposited and annealed ZnO layers and the variation of the FWHM of P_S and P_B as a function of annealing temperature……………………………...42

Figure 4-3 The ϕ-scan across the off-normal ZnO $\{10\bar{1}1\}$ reflection of as-deposited and annealed ZnO layers, together with the ϕ-scan across sapphire $\{11\bar{2}6\}$ ………………………44

Figure 4-4 The cross sectional TEM image of the as-deposited ZnO epi-layer along the $[11\bar{2}0]$ zone axis, the SAED pattern, and the image of 800°C annealed sample taken under the same pole………………………………………………………………………………………...47

Figure 4-5 The bright-filed images of the ZnO layer annealed at 800°C with diffraction vector g set to $(10\bar{1}1)$, (0002), and $(10\bar{1}0)$ ……………………………………………………………46

Figure 4-6 The AFM images of the as-deposited and annealed ZnO layers with the scan image profiles of the as-deposited and annealed samples…………………………………….………51

Figure 4-7 Low temperature PL spectra taken at 10 K of the ZnO films grown by ALD and PLD methods……………………………………………………………………………………52

Figure 4-8 Temperature dependent PL spectra of the ZnO film taken between 10 and 280 K and the energy versus temperature plot of the BSF and NBE emissions…………………………...55

Figure 4-9 The power dependent PL spectra recorded at 10 K of the ZnO film grown by ALD and annealed at 800°C…………………………………………………………………………56

Figure 5-1 XRD radial scans along the surface normal (θ-2θ scan) of an as-deposited ZnO film and a 800ºC annealed sample, and the ω rocking curves across the $(10\bar{1}0)_{ZnO}$ specular reflection……………………………………………………………………………………67

Figure 5-2 The azimuthal reflection scan across the $\{10\bar{1}2\}_{ZnO}$ and $\{30\bar{3}0\}_{Al_2O_3}$ planes………………………………………..……………………………………………69

Figure 5-3 X-ray reflectivity of the as-deposited ZnO films and those after annealed at 400, 600, and 800 ºC…………………………………………………………………………………71

Figure 5-4 The cross sectional TEM image and the SAED pattern taken along the $[\bar{1}2\bar{1}0]_{ZnO}$ zone axis, and the bright field images recorded with diffraction vector g equal to $(10\bar{1}0)_{ZnO}$ and $(0002)_{ZnO}$ ………………………………………………………………………73

Figure 5-5 The cross sectional TEM image and the selected area electron diffraction (SAED) pattern taken along the zone axis of $[0001]_{ZnO}$, and the bright field images taken with diffraction vector g equal to $(10\bar{1}0)_{ZnO}$ and $(\bar{1}2\bar{1}0)_{ZnO}$ ……………………………………………75

Figure 5-6 The high resolution images of the interface with the zone axis of $[\bar{1}2\bar{1}0]_{ZnO}$ and $[0001]_{ZnO}$, and the inset is the corresponding Fourier filtered image…………….…………….74

Figure 5-7 AFM images of the as-deposited and annealed *m*-ZnO films with surface roughness (R_{rms}) of 1.62 and 1.38 nm, respectively………………………………………………………77

Figure 5-8 The time integrated photoluminescence at 5 K of the as-deposited sample and sample annealed at 400 and 800°C with the inset of the annealing temperature dependent intensity ratio of NBE band to BSF band……………………………………………………………………81

Figure 5-9 The time resolved photoluminescence at 5 K of the NBE and B band in the sample annealed at 800°C………………………………………………………………………………81

Figure 6-1 The power dependent TI-PL spectra recorded at 5 K of the ZnO film grown by ALD and annealed at 600°C and the intensity versus the excitation power of the BSF and NBE emissions……………………………………………………………………………………87
Figure 6-2 The temperature dependent TI-PL spectra of the ZnO film taken between 10 and 200 K, the energy versus temperature plot of the BSF and NBE emissions…………………………88
Figure 6-3 The TR-PL spectra at temperature 10 K with excitation power of 100 μW, and each curve is integrated with time interval of 6 ps after pulsed excitation……………………………90
Figure 6-4 The decay curves of the intensity integrated from the BSF and NBE emissions in energy ranges of 3.280 ~ 3.345 eV and 3.345 ~ 3.397 eV, respectively…………………………91
Figure 6-5 The spectra dependent decay times are the plots with the same excitation power 100μW at different temperature 5 and 90 K, and with different excitation power 10 and 1020 μW at the same temperature 5 K…………………………………………………………………92
Figure 6-6 The potential fluctuation due to the fluctuation of alloy density……………………94
Figure 6-7 The wave functions of the lowest two energy levels of the symmetric QWs with a central barrier width of 4 nm, and the confinement energies of the lowest two states as function of the central barrier width…………………………………………………………………95
Figure 6-8 Band profiles (black curve), electron envelope functions (red curve) and energy (dotted red line) for electron confined on a D^0-BSF complex with distance d of 2.5 nm between donor and BSF plane……………………………………………………………………96

Chapter 1 Introduction

1.1 Overview of ZnO

The ZnO material is II-VI semiconductor and attracts much research attention for decades because of its wide direct band gap about 3.374 eV and large exciton binding energy about 60 meV, which leads the high emission efficiency and the lasing action based on exciton recombination at room temperature. In addition, the other properties of the ZnO such as the non-toxicity, high physical stability, and piezoelectricity also reveal the potential for industrial and advanced optics-electro applications [1-9]. Over the past decade, in order to perform the properties of the quantum physics many efforts are put into the topic of fabricating the nano-scale structures of ZnO such as nano-rods [10], quantum-dots [11] and quantum-wells. [12]

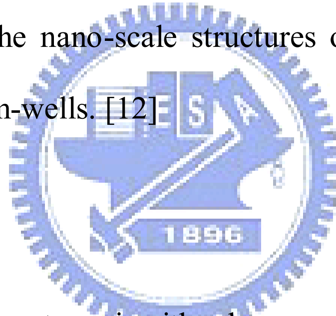

1.1.1 Properties of ZnO

The ZnO has the crystal structures in either hexagonal wurtzite, cubic zinc-blende, or cubic rocksalt structure, they are shown in Fig. 1-1. [13] At the ambient conditions, the thermodynamically stable ZnO structure is wurtzite structure, which belongs to the space group C_{6v}^{4} and has the lattice constants a = 3.243 and c = 5.203 Å. The ZnO with zinc-blende crystal structure could be formed on cubic substrates and the estimated lattice constant ranges from 4.37 ~ 4.47 Å. The basal stacking faults can be considered as a thin layer of zinc-blende structure being embedded in the wurtzite ZnO. According to the arrangement of atoms in basal stacking fault, the lattice constant of zinc-blende could be estimated as about 4.586 Å from the lattice constants of wurtzite ZnO. Besides, the rocksalt ZnO structure could be obtained at relatively high pressures from the wurtzite

structure due to the phase transition, and the estimated lattice constant ranges from 4.271 to 4.294 Å. [13]

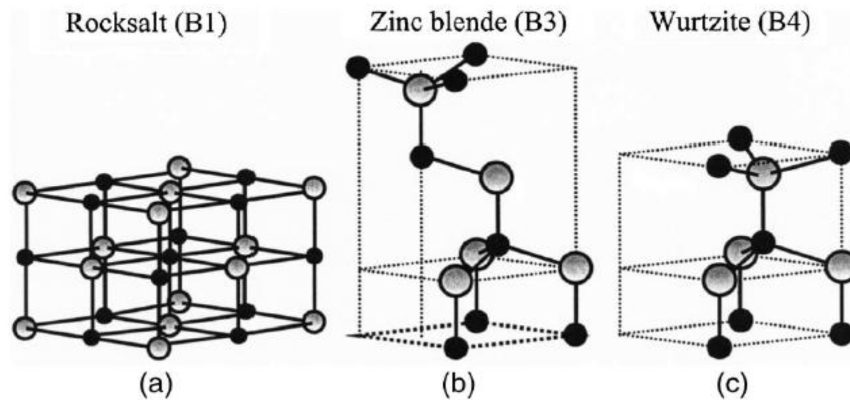

Fig. 1-1 Stick and ball representation of ZnO crystal structures: (a) cubic rocksalt (B1), (b) cubic zinc blend (B3), and (c) hexagonal wurtzite (B4). The shaded gray and black spheres denote Zn and O atoms, respectively.

As the structures shown in Fig. 1-1, the atomic arrangement of zinc-blende structure is similar to that of the wurtzite structure, but the zinc-blende ZnO structure is metastable and is reported to be grown on cubic substrates such as ZnS. [31] Many efforts have been put onto the research of wurtzite ZnO epitaxy, while a few experimental and theoretical literatures had reported on zinc-blende ZnO growth and its fundamental properties. The zinc-blende structure has the highest symmetry compatible with the existence of piezoelectric polarization under the strain in the [001] directions, which offers an attractive platform for exploring the excitonic systems without the perturbation field. [14]

The ZnO crystal in wurtzite structure contains polar and non-polar crystallographic

planes, which determine the optical and electrical properties of the films. Strong spontaneous polarization and piezoelectric polarization at the interfaces of ZnO based heterostructures induce a large internal electric field along the *c*-axis that results in the quantum-confined Stark effect leading to a spectral red-shift and a dramatic decrease in the luminous efficiency. In order to avoid this problem, many efforts have been put to enhance the luminous efficiency by taking advantage of the non-polar *m*-plane orientated ZnO layers [15].

1.1.2 Growth of ZnO Thin Films

The traditional methods of fabricating the ZnO films include the metal-organic chemical deposition (MOCVD), molecular beam epitaxial (MBE), radio-frequency sputter (RF-sputter), and pulse-laser deposition (PLD), which usually demand high growth temperature and high vacuum environment. In addition, many kinds of substrates are used to fabricate these ZnO structures. The *c*-plane sapphire substrate is usually adopted for fabricating the *c*-plane ZnO films. For reducing the strains, diminishing dislocation density, and obtaining high quality of epitaxial crystalline, ZnO are also fabricated on other substrates, such as Si, SiC, GaAs, CaF_2, and $ScAlMgO_4$. [13] Nonetheless, in order to fabricate the non-polar orientated ZnO layers the non-polar sapphire such as *r*- and *m*-plane sapphires are adopted as the substrates. [16]

1.2 Atomic Layer Deposition

Atomic layer deposition (ALD) is a chemical vapor deposition technique, which is used to manufacture inorganic material layer with thickness down to a fraction of a

monolayer. ALD is able to deposit a conformal layer with high quality on extremely complex shapes that is the unique feature among various deposition techniques. ALD based on sequential self-terminating gas-solid reactions has been applied for about four decades. In recent years, the increasing research interest in use of ALD is attributed to the scaling down microelectronic devices.

1.2.1 Application of ALD

Because of the ability of controlling thickness, ALD has been studied for depositing the gate insulator layer of the transistor. The gate insulator layer, traditionally made by silicon dioxide to separate the gate terminal of a transistor from the source and drain terminals as well as the conductive channel that connects source and drain when the transistor is turned on. The gate oxide layer sustaining electric field to modulate the conductance of the channel should be made as thin as possible to increase performance. However, while the thickness of the gate layer is down to few nanometers the quantum mechanical phenomenon of electron tunneling occurs between the gate and channel and leads to increase power consumption. In order to overcome the increase in power consumption, the high-κ dielectric materials such as Al_2O_3, ZrO_2, and HfO_2 are used instead of silicon dioxide for higher gate capacitance and lower leakage effects. [17,18] Besides, in the development of DRAM capacitor, the high conformal depositing requirement leads ALD to the most promising depositing technique. [19] In order to assure sufficient data retention time of DRAM, high charge storage capacitance is required. Three-dimensional capacitor structures with high aspect ratios are therefore commonly used in the DRAM industry for small cell size and thus reduce chip cost. For the three-dimensional structures of nano-rods, and nano-particles, ALD also shows excellent conformal depositing ability. [20,21]

1.2.2 ZnO grown by ALD

Recently years, the research interest in fabricating the ZnO thin film by ALD is increasing, and it is able to obtain the epitaxial quality. Depending on the different substrates, the epitaxial ZnO thin films have been grown on different surface planes. There has been reported that the *c*-plane ZnO thin films could be grown on the *c*-plane sapphire, *c*-plane GaN, or yttria-stabilized zirconia with (111) layer; and the *m*-plane ZnO has been grown on the *m*-plane sapphire. [22,23,24] For the precursors, the sources of zinc atoms could be the diethyl-zinc (DEZ) or zinc acetate, and the sources of oxygen could be the water or nitrous oxide. [25,26]

The ALD method is also able to deposit the functional ZnO layer by doping other material such as Mg, Al, Ga, P, and N. For doping Mg, Al, Ga, and P, the cyclopentadienylmagnesium, trimethy-aluminum, triethylgallium, and trimethylphosphite are used as the precursors, respectively, to provide the dopants. Controlling the doping ratio has been implemented by manipulating the number ratio of ZnO and dopant-oxide layers, or by using the mixed precursor of DEZ and dopant sources. [32-35] For N doping, the ammonium hydroxide and ammonia have been used as the precursor, and the doping ratio controlling is implemented by the number ratio of depositing layers or mixing the dopant precursor with the carrier gas. [36,37]

1.3 Motivation

The ALD has usually been used for the deposition of the insulator layer of the DRAM and transistors. These growth features of the ALD are very powerful for fabricating electronic devices; especially for the dimension downscales to the few

nanometers in the complex three-dimensional structures. However, the ALD on the respect of fabricating the electro-optic device is still very lack of understanding and needs more efforts on research.

1.3.1 The Growth Mechanism of the ALD Reaction

ALD growth mechanism bases on the sequential self-terminating chemical reactions that is a kind of chemical style/way. Such a growth technique is different from the deposition techniques based on the physical style/way such as PLD, MBE, and RF-sputtering, which decompose the material into particles or plasma in high temperature for following deposition. The demand of depositing particles and/or plasma is very high vacuum to prevent from colliding with the undesired gas molecules that raises the difficulty of deposition. Besides, the dissolving problem is usually the problem for depositing the alloy material with high concentration by using the techniques in physical ways. Therefore, the depositing with sequential self-terminating chemical reactions is reasonably considered to make sure that the different materials of alloy would be deposited layer-by-layer along growing direction. The concentration of the alloy material could be expected to closely 50 %, in theory, and in the meanwhile the demand of the growth temperature and vacuum condition would be rather low. In addition, the controlling of depositing thickness in few atoms and the conformal depositing layer on complex structure could be reached. Such features of ALD technique are reasonably expected and worthy of investing in effort to research.

1.3.2 Epitaxial Growth of Polar and Non-Polar ZnO Films

As mentioned previously, the non-polar ZnO thin films traditionally grown in use of

MBE, PLD, MOCVD, and RF-sputter require high growth temperature, high vacuum, high precursor consuming, or high electrical power. In ALD, the growth temperature depends on the reaction temperature of the precursors. For growing the ZnO thin film, diethyl-zinc (DEZ) and water are used as the precursors for providing the source of zinc and oxygen atoms with suitable growth temperature at 200 ^{o}C. The precursors reacting can occur at the pressure of about few Torrs, which means that the low requirement of vacuum. The consumption of the precursors depends on the reaction surface area and the capacity of reaction chamber.

In addition to the requirement of growth conditions, to fabricate *m*-plane ZnO epi-films with high structural perfection and smooth surface morphology is still difficult for these tradition deposition techniques. One common problem is the coexistence of minor domains with $(10\bar{1}3)$ which are difficult to eliminate. [27,28,29] Moreover, surface morphologies of the deposited *m*-plane ZnO films on foreign substrates often exhibit stripe features elongated along a direction either parallel or normal to the ZnO *c*-axis depending on the growth conditions. These features strongly hamper the applications of ZnO-based heterostructures. For the ALD technique, the sequential self-terminating gas-solid reactions are expected to lead to the layer-by-layer growth mechanism, which is a two-dimensional growth mode. It is expected to grow the polar and non-polar ZnO thin films with epitaxial quality, high flatness, high uniform thickness, and without the co-existing domains. Therefore, to investigate the fabrication process, chemical reaction situation, influence of lattice mismatch, and crystalline structure property are very import issues for the developing the fabrication technique.

1.3.3 Research of the Basal Stacking Faults in Wurtzite ZnO

The growth mechanism of ALD is considered to influence the structure of the as-grown ZnO thin films and leads to specific crystalline features such as the high-density basal stacking fault (BSF). Theoretical study showed that the BSF structure embedded in the ZnO thin film leads to the band alignment in the form of type-II quantum wells, and influences the photoluminescence properties. [30] Such a specific band alignment is attributed to that BSFs in the material of wrutzite (WZ) structure has the lattice structure of zinc blend (ZB). For the research of ZnO material, the ZB structure is very difficult to be grown, which leads to that the understanding of ZB ZnO material is still insufficient and desired. As the development of the *ab initio* technique, many properties the ZB ZnO are calculated such as the lattice constants, and band gaps. The ZB ZnO is also predicated to have lower carrier scattering and higher doping efficiencies than the WZ ZnO. [14] Therefore, such high density of the BSFs in the ZnO thin films makes measuring and observing the properties of ZB ZnO thin film possible. Through the photoluminescence measurements, we investigate the ZB ZnO thin film by observing the dynamic of the excitons in the BSFs.

1.4 Organization of this Dissertation

In this thesis, we present the growth of ZnO thin films by ALD, and investigate the influence of the thermal annealing treatment. And we study the structural properties of these ZnO films through the measurements of X-ray diffraction (XRD), transmission electron microscope (TEM), and atomic force microscope (AFM). In Chapters 4 and 5, we present the results of the *c*- and *m*-plane ZnO thin films, and discuss how the growth

mechanism of ALD influences the crystalline structure. As high density of BSFs are observed in the *m*-plane ZnO, in Chapter 6 we take the advantages of the temperature dependent, power dependent, and time-resolved photoluminescence measurements to observe the excitons dynamics in BSFs—ZB ZnO thin films.

References

[1] A. Tsukazaki, A. Ohtomo, T. Onuma, M. Ohtani, T. Makino, M. Sumiya, K. Ohtani, S. F. Chichibu, S. Fuke, Y. Segawa, H. Ohno, H. Koinuma, M. Kawasaki, *Nat. Mater.* 4, 42 (2005)

[2] J. H. Lim, C. K. Kang, K. K. Kim, I. K. Park, D. K. Hwang, and S. J. Park, *Adv. Mater.* 18, 2720 (2006)

[3] A. Smith, *Thin Solid Films* 376, 47 (2000)

[4] X. T. Hao, L. W. Tan, K. S. Ong, and F. R. Zhu, *J. Cryst. Growth* 287, 44 (2006)

[5] R. K. Shukla, A. Srivastava, A. Srivastava, K. C. Dubey, *J. Cryst. Growth* 294, 427 (2006)

[6] J. Jo, O. Seo, H. Choi, B. Lee, *Appl. Phys. Express* 1, 041202 (2008)

[7] I. T. Tang, Y. C. Wang, W. C. Hwang, C. C. Hwang, N. C. Wu, M. P. Houng, Y. H. Wang, *J. Cryst. Growth* 252, 190(2003)

[8] R. Tena-Zaera, A. Katty, S. Bastide, C. Levy-Clement, *Chem. Mater.* 19, 1626 (2007)

[9] C. Platzer-Bjorkman, I. Torndahl, A. Hultqvist, J. Kessler, M. Edoff, *Thin Solid Films* 515, 6024 (2007)

[10] J. C. Johnson, H. Yan, R. D. Schaller, L. H. Haber, R. J. Saykally, and P. D. Yang, *J. Phys. Chem. B* 105, 11387 (2001)

[11] S. Monticone, R. Tufeu, and A. V. Kanaev, *J. Phys. Chem. B* 102, 2854 (1998)

[12] Z. L. Wang, J. Phys.: Condens. Matter 16, R829 (2004)

[13] U. Ozgur, Ya. I. Alivov, C. Liu, M. A. Reshchikov, S. Dogan, V. Avrutin, S.-J. Cho, and H. Morkoc, J. Appl. Phys. 98, 041301 (2005)

[14] A. Ashrafi, C. Jagadish, J. Appl. Phys. 102, 071101 (2007)

[15] M. M. C. Chou, L. Chang, H.-Y. Chung, T.-H. Huang, J.-J. Wu, and C.-W. Chen, *J. Crystal Growth* 308, 412 (2007)

[16] J.-M. Chauveau, P. Vennegues, M. Laugt, C. Deparis, J. Zuniga-Perez, and C. Morhain, J. Appl. Phys. 104, 073535 (2008)

[17] P. D. Ye, G. D. Wilk, B. Yang, J. Kwo, S. N. G. Chu, S. Nakahara, H.-J. L. Gossmann, J. P. Mannaerts, M. Hong, K. K. Ng, and J. Bude, *Appl. Phys. Lett.* 83, 180 (2003)

[18] G. D. Wilk, R. M. Wallace, and J. M. Anthony, *J. Appl. Phys.* 89, 5234 (2001)

[19] M. Rinkiö, A. Johansson, G. S. Paraoanu, and P. Törmä, *Nano Lett.* 9, 643 (2009)

[20] D. M. King, X. Liang, C. S. Carney, L. F. Hakin, P. Li, and A. W. Weimer, *Adv. Funct. Mater.* 18, 607 (2008)

[21] B. Min, J. S. Lee, J. W. Hwang, K. H. Keem, M. I. Kang, K. Cho, M. Y. Sung, S. Kim, M.-S. Lee, S. O. Park, and J. T. Moon, *J. Crystal Growth* 252, 565 (2003)

[22] S. Yang, B. H. Lin, W.-R. Liu, J.-H. Lin, C.-S. Chang, C.-H. Hsu, and W. F. Hsieh, *Cryst. Growth Des.* 9, 5184 (2009)

[23] S. Yang, B. H. Lin, C. C. Kuo, H. C. Hsu, W.-R. Liu, M. O. Eriksson, P.-O. Hotz, C.-S. Chang, C.-H. Hsu, and W. F. Hsieh, *Cryst. Growth Des.* 12, 4745 (2009)

[24] C.-W. Lin, D.-J. Ke, Y.-C. Chao, L. Chang, M.-H. Liang, and Y.-T. Ho, *J. Crystal Growth* 298, 472 (2007)

[25] P.-Y. Lin, J.-R. Gong, P.-C. Li, T.-Y. Lin, D.-Y. Lyu, D.-Y. Lin, H.-J. Lin, T.-C. Li,

K.-J. Chang, and W.-J. Lin, *J. Crystal Growth* 310, 3024 (2008)

[26] W. WóJicik, M. Godlewski, E. Guziewicz, R. Minikayev, and W. Paszkowicz, *J. Crystal Growth* 310, 284 (2008)

[27] J. W. Lee, J. H. Kim, S. K. Han, S. K. Hong, J. Y. Lee, S. I. Hong, T. Yao, *J. Cryst. Growth* 312, 238–244 (2010)

[28] J. H. Kim, S. K. Han, S. I. Hong, S. K. Hong, J. W. Lee, J. Y. Lee, J. H. Song, J. S. Park, T. Yao, *J. Vac. Sci. Technol. B* 27, 1625–1630 (2009)

[29] T. Moriyama, S. Fujita, *Jpn. J. Appl. Phys.* 44, 7919– 7921 (2005)

[30] Y. Yan, G. M. Dalpian, M. M. Al-Jassim, S.-H. Wei, Phys. Rev. B. 70, 193206 (2004).

[31] T. Kogure, and Y. Bando, J. Electron Microsc. 47, 7903 (1993)

[32] C. Platzer-Bjökman, T. Torndahl, A. Hultqvist, J. Kessler, and M. Edoff, Thin Solid Films 515, 6024 (2007)

[33] K. Saito, Y. Hiratsuka, A. Omata, H. Makino, S. Kishimoto, T. Yamamoto, N. Horiuchi, and H. Hirayama, Superlattices and Microstructures 42, 172 (2007)

[34] J. W. Elam, and S. M. George, Chem. Mater. 15, 1020 (2003)

[35] H. Yuan, B. Luo, S. A. Campbell, and W. L. Gladfelter, Electrochemical and Solid-State Letters 14, H181 (2011)

[36] C. Lee, S. Y. Park, J. Lim, and H. W. Kim, Mater. Lett. 61, 2495 (2007)

[37] S. J. Lim, S.-J. Kwon, H. Kim, and J.-S. Park, Appl. Phys. Lett. 91, 183517 (2007)

Chapter 2 Theoretical Background

2.1 Growth Mechanism of Atomic Layer Deposition

Atomic Layer Deposition (ALD) is a chemical vapor deposition technique with layer-by-layer growth mechanism and the features of low growth temperature, high uniformity, low vacuum demand, and thickness controlling in the nanometer range. Such features are the results of the sequential and self-terminating chemical reactions of the precursors on substrate surface. For depositing the epitaxial ZnO thin film, the reacting temperature of the chemical reaction is ranged from room temperature to about 250 ºC, and the most suitable growing temperature is about 200 ºC. The precursor for providing zinc is the diethyl-zinc (DEZ), which is the colorless liquid contained in the bubbler and has vapor pressure about 15 torr at 25 ºC and boiling point at 118 ºC under 1 atm.

The sequential self-terminating gas-solid reactions for growing ZnO layers by ALD consist of the following four steps:

(a) The introducing and the self-terminating reaction of the first precursor A -- DEZ.

(b) Purging the residual precursor and the by-products, and then evacuating the reaction chamber.

(c) The introducing and self-terminating reaction of the second precursor B -- water (H_2O).

(d) Purging the residual precursor and the by-products, and then evacuating the reaction chamber.

One *reaction cycle* consists of the steps 1 to 4, which would deposit amount of ZnO material to the surface.

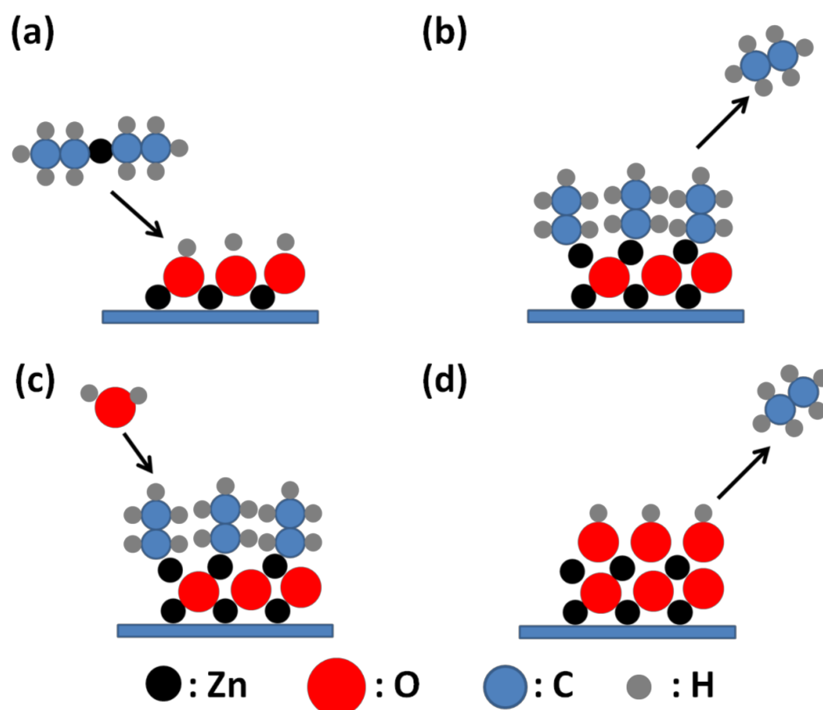

Fig. 2-1 One cycle of ALD growth consists of the four steps: (a) introducing DEZ, (b) purging by-products, (c) introducing water (H_2O), and (d) purging by-products.

1896

The illustration of one ALD reaction cycle is sketched in Fig. 2-1. Each reaction cycle adds a given amount of ZnO onto the surface. To grow a ZnO layer, reaction cycles are repeated until the desired thickness of layer achieved. The ALD process starts when the substrate surface is in a stabilized state with the desired temperature and hydroxyl group on the substrate surface. The ALD growth mechanism bases on the self-terminating reactions, which means the dominating factor is the surface-state control while the other process parameters (such as the precursor flow rate and chamber pressure) have little or no influence.

2.2 Photoluminescence of ZnO

The wurtzite ZnO material has the wide direct band gap of about 3.37 eV and the high binding energy of the free-exciton (FX) about 60 meV. The properties of the emission transitions in ZnO attract variety of research attention. The main intrinsic excitonic emission transition is free exciton (FX), which is usually bound by the donors and/or acceptors to form donor-bound exciton (D^0X) and/or acceptor-bound exciton (A^0X), respectively. In certain conditions, the transitions of the two-electron satellites (TES) related to the D^0X, LO-phonon replica of the main excitonic transitions, and the donor-acceptor-pair (DAP) transitions could be observed. Recently, the basal stacking fault (BSF) is found to form the type-II quantum well in the wurtzite structure and trap the excitons. Such excitons bound by the BSF is possibly influenced by intrinsic defects such donor and acceptor, which leads to a complex transition mechanism. [2] Through the Mg-doping technique, the energy band gap and band alignment could be engineered to fabricate the quantum wells (QWs) structure. By taking advantage of the designed micro-cavity to enhance the coupling of excitons and photons, the transition of excion-polaritons was observed. [3]

2.2.1 Free Exciton (FX)

The FX is a bound state of an electron and a hole, which attract to each other by the Coulomb interaction. It is taken as an electrically neutral quasi-particle. An FX could result from an excited electron from the valence band into the conduction band and leaves a positively charged hole. Such electron and hole pair is in the form of hydrogenic system, which provides a stabilizing energy state slightly less than the energy of

unbounded electron and hole. The binding energy is the difference of energy between the stabilizing energy of the hydrogenic system and the unbounded electron and hole. The binding energy of the FX in ZnO is about 60 meV that prevents the FX from thermal ionization at room temperature while the thermal energy at room temperature is about 25 meV.

2.2.2 Bound Exciton Complex

The exciton as a quasi-particle is usually bound by the dopants or native defects, which results in the bound exciton complex and discrete electronic states in the band gap. The exciton bound by the neutral or charged donors and acceptors forms the neutral donor bound exciton (D^0X), charged donor bound exciton (D^+X), neutral acceptor bound exciton (A^0X), and charged acceptor bound exciton (A^-X). In high quality bulk ZnO, the D^0X often dominates because of the unintentional impurities and/or shallow donor-like defects, and the A^0X is usually observed in ZnO containing acceptors due to the intentionally p-type doping technique. Therefore, the transition of D^0X is usually observed to dominate the PL spectra at low temperature, at which the thermal energy is able to ionize into FX. At low temperature under 10 K, the transition energy of the D^0X is in the range of 3.360~3.368 eV and the transition energy of the A^0X is in the range of 3.348~3.374 eV.

Another characteristic of the neutral D^0X is the two electron satellites (TES). For the ZnO material, the transition energy of TES is in the range of 3.32~3.34 eV. The transition of TES results from an exciton bound to a neutral donor in excited state, and is usually observed in the samples with extreme crystalline quality, and has the intensity weaker than the D^0X.

Donor-acceptor pairs (DAP) can be considered as "polycentric" bound excitons.

When an electron on a donor has the wave function overlap with a hole on an acceptor, the transition of DAP would occur. The energy of the transition of the DAP is given by

$$E_{DAP} = E_g - (E_D + E_A) + \frac{e^2}{4\pi\varepsilon_0 \varepsilon r} - m\hbar\omega_{LO} ,$$

where r is the separation value of donor-acceptor pair, E_D and E_A are the respective ionization energies of the donor and the acceptor as isolated impurities. E_g is energy band gap of the ZnO and the last term presents the LO phonon replica. Therefore, the energy of the DAP transition E_{DAP} depending on the separation value r of the donor-acceptor pair. With increasing excitation power, the number of occupied donor and acceptor centers increases and their average distance necessarily decreases, which lead to the DAP blue-shift of the DAP transition energy E_{DAP}.

2.2.3 Basal Stacking Faults Emission

According to the atomic stacking sequence of the BSFs, each BSF embedded in wurtzite structures can be taken as a thin zinc-blende layer surrounded by the wurtzite barriers. The band structure of a zinc-blende ZnO is still under debate since a few papers have been reported. Based on the *ab initio* calculation [4], the BSFs as the zinc blend layer leads to the QW-like region act as type-II QWs with 147 and 37 meV negative band offsets of the conduction band minimum and the valance band maximum to those of the barriers, respectively. The sketch of the band alignment is plot in Fig. 2-2. This means that the BSF structure would be a potential barrier at the valence band and a potential well in the conduction band to capture the electrons, which attract the holes in wurtzite structure via Coulomb interaction to form the BSF confined exciton [5].

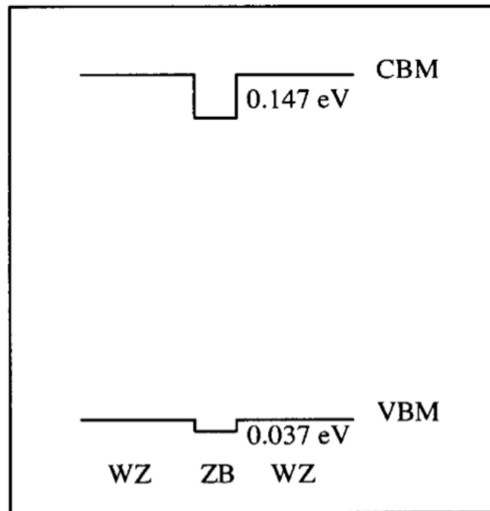

Fig. 2-2 The schematic plot of the band alignment of ZnO at WZ/ZB/WZ regions.

2.3 XRD Measurement

The X-ray measurements were conducted using a four-circle diffractometer at beamline BL13A of National Synchrotron Radiation Research Center (NSRRC) Taiwan with incident wavelength 1.02473 Å. Two pairs of slits located between the sample and a NaI scintillation detector were employed and yielded a typical resolution of better than 1×10^{-3} Å^{-1}. The X-ray Diffraction measurements are the powerful technique to observe and determine the structural properties of the deposited crystalline film in the theory of diffraction.

2.3.1 X-ray Diffraction Theory

For the crystalline material, the periodical structural information can be determined by analyzing the reflected X-ray from the material. In Fig. 2-3, the incident X-rays are

reflected from the adjacent atomic planes with spacing of d in the crystalline material, and the reflected rays result in the constructive interference while match the condition of the Bragg's law: $n\lambda = 2d\sin\theta$, where the λ is the wavelength of X-ray and θ is the angle between incident X-rays and reflecting planes.

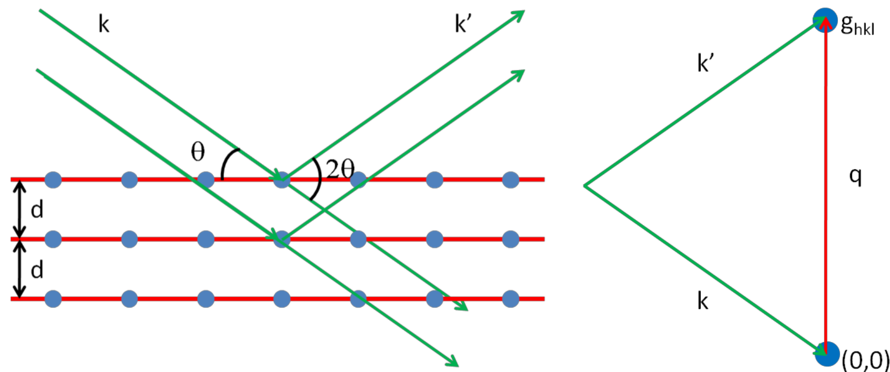

Fig. 2-3 Bragg diffraction condition in (a) real space and (b) reciprocal space.

In the elastic scattering process, the incident and emergent X-rays with wave vectors k and k', both of which have the magnitude of $2\pi/\lambda$, and the scattering vector q can be obtained by the equation: $q \equiv k' - k = 2k\sin\theta$. In reciprocal space, every periodical plane with spacing d in real space is transformed as a point with a lattice spacing of $2\pi/d$, while $q = 2\pi/d$ the diffraction condition match the Bragg's Law. Therefore, each set of periodical parallel planes in real space can be represented by the Miller indices (hkl), and be expressed by corresponding lattice vector: g_{hkl}, where the $|g_{hkl}|$ value is equal to $2\pi/d_{hkl}$. The ZnO crystal structure is hexagonal with lattice parameters $a = 3.243$ Å and $c = 5.203$ Å ($\alpha = \beta = 90°, \gamma = 120°$). The reciprocal lattice vector g_{hkl} of a hexagonal lattice can be expressed by

$$|g_{hkl}| = \frac{2\pi}{d_{hkl}} = \pi\sqrt{\frac{4}{3}\left(\frac{h^2+hk+k^2}{a^2}\right)+\frac{l^2}{c^2}}.$$

Conventionally, for crystals with hexagonal and rhombohedral symmetry, crystallographic planes are denoted using the four indices based on a four-axis Miller-Bravias coordinate system, consisting of three basal plane axes (a_1, a_2, a_3) at $120°$ angles to each other and the fourth axis c perpendicular to the basal plane. The Miller-Bravias indices $(hkil)$ satisfy the conditions $i = -(h+k)$. In this thesis, 4-digit Miller-Bravias indices are used for materials with hexagonal and rhombohedral symmetries including ZnO and sapphire to distinguish them from those with cubic symmetry.

For determining the crystalline structure properties, the four-circle diffractormeter is used which consists of four rotatable circles: θ, 2θ, χ and ϕ. The 2θ circle is the detector axis controlling the magnitude of scattering vector q. The θ, χ, and ϕ circles control the sample orientation. When the q vector coincides with the specific reciprocal lattice vector g, the Laue condition is satisfied. The ϕ angle is equivalent to the azimuthal angle and the χ angle is related to the polar angle of the crystal film. Different scan methods could perform the macro observation with different respect. The $\theta/2\theta$ scan could observe the coherent length along the surface normal. The orientation of the deposited film could be observed through the θ rocking curve scan, and the ϕ scan could determine the symmetry. The XRR method could confirm the roughness and thickness of the deposited layers.

2.3.2 Radial Scan

Radial scan is performed by driving the two rotatable circles: θ and 2θ, which is

shown in Fig. 2-4, to vary the q vector to scan the reciprocal space in the surface normal direction. The most commonly performed radial scan is the one along sample surface normal, which is often known as $\theta-2\theta$ or $\omega-2\theta$ scan as shown Fig. 2-4. From the positions of diffraction peaks we can determine the corresponding interplanar spacing along the direction of q and the line width of the diffraction peak can yield the structural coherence length (grain size) and inhomogeneous strain along the same direction.

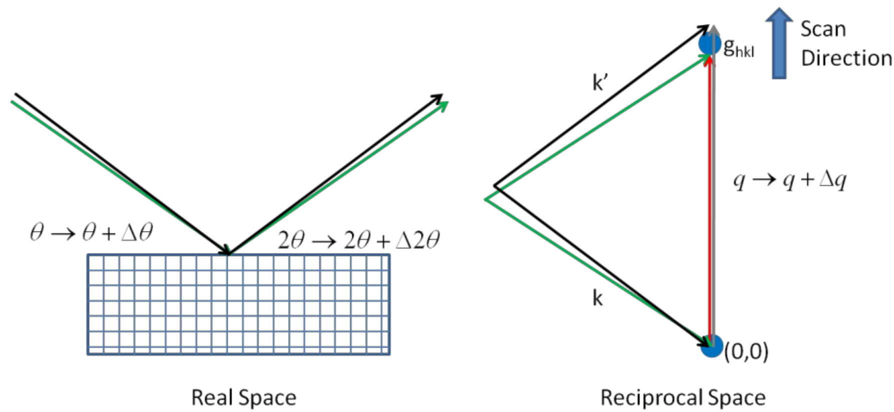

Fig. 2-4 The radial scan situation in the real space and reciprocal space.

1896

2.3.3 Rocking Curve

As shown in Fig. 2-5 for a given incident x-ray direction, a detector is placed at the position of a diffraction spot with certain lattice vector, the scattered x-ray collected while the crystal is rotated by means of scanning the θ angle, which is also called "θ rocking curve". The width of a rocking curve $\Delta\theta$ is a direct measurement of the width of the diffraction spot in the reciprocal space. The $\Delta\theta$ also presents the distribution of the sub-grains' orientation in the film; the wide distribution leads to the larger $\Delta\theta$.

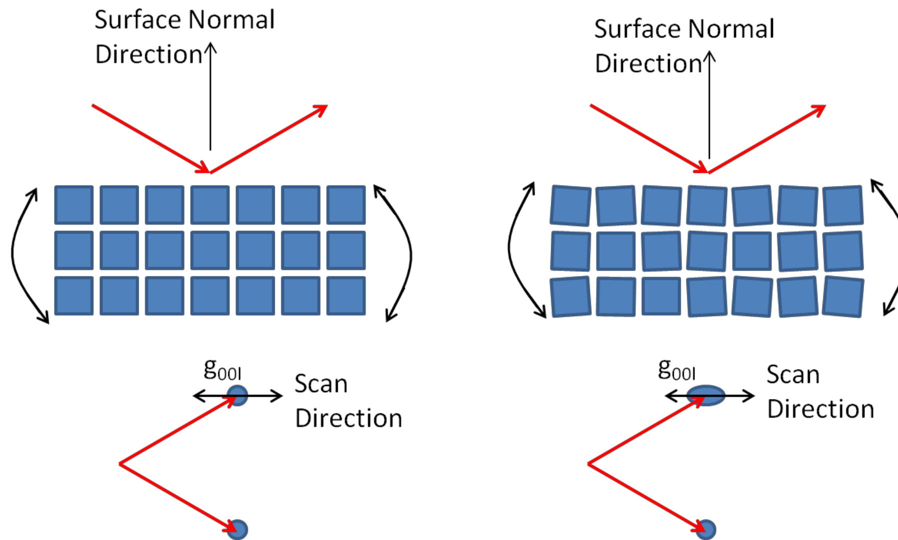

Fig. 2-5 θ-rocking scan situations in the real space and reciprocal for ideal and non-ideal lattice structures.

2.3.4 Azimuthal Scan

Azimuthal scan means measuring the diffraction intensity as a function of azimuthal angle ϕ by rotation the sample along an axis, which is usually parallel to surface normal or, in some cases, to a specific crystallographic axis. Figure 2-6 illustrates the scheme of the Azimuthal scan which can used to study the symmetry and crystal quality of the grown film and determine its relative orientation with substrate in epitaxy.

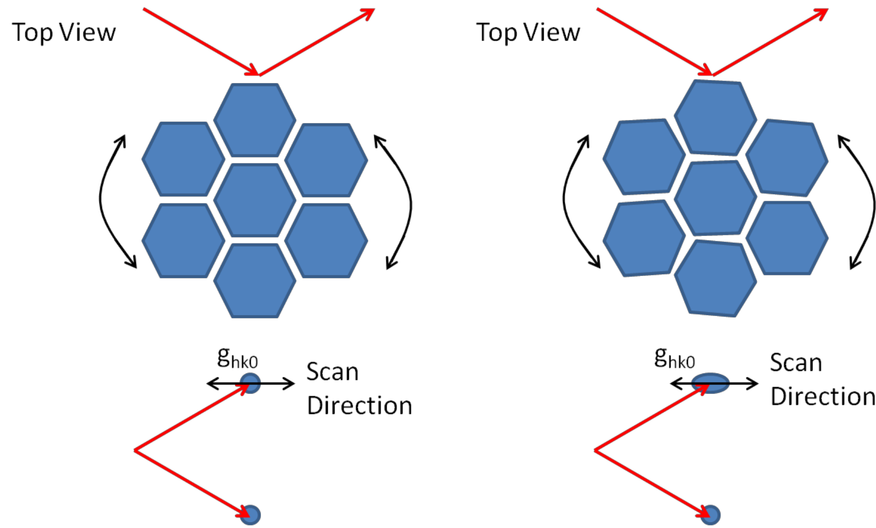

Fig. 2-6 Azimuthal angle scan situations in the real space and reciprocal for ideal and non-ideal lattice structures.

2.3.5 X-ray Reflectivity

X-ray reflectivity (XRR) is a surface-sensitive and non-destructive analytical technique to estimate the density, thickness and roughness of thin film structures by analyze the reflection of the X-rays from the surface and interfaces among layers. The setup of the XRR is sketched in Fig. 2-7(a). [6] Through scanning of the incident X-ray, the reflected X-rays result in interference that leads to the periodic interference stripes in Fig. 2-7(b). For the X-ray beam, the index of refraction n is defined as:

$$n = 1 - \delta + i\beta = 1 - \frac{\lambda^2}{2\pi} r_e \rho_e + i \frac{\lambda}{4\pi} \mu_x ,$$

where is the x-ray wavelength, r_e is the classical electron radius, ρ_e is the electron density of the material, and μ_x is the absorption length. According to the Fresnel reflection equation, the total external reflection of X-ray occurs at the angle of incidence smaller than the critical angle, $\theta_c = \sqrt{2\delta}$, which depends on the electron density of the material. [17]

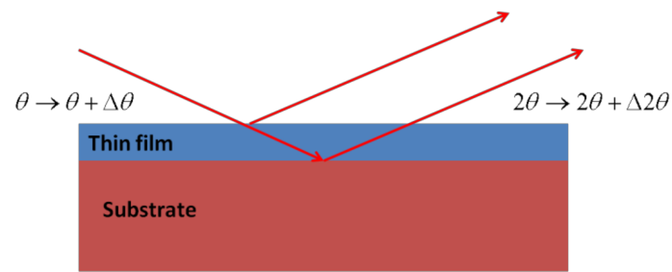

(a)

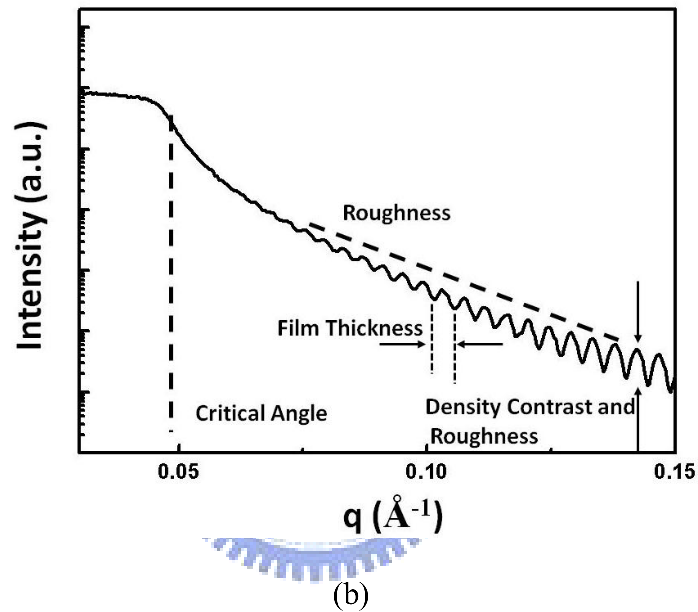

(b)

Fig. 2-7 X-ray reflectivity measurement situation of (a) the thin film structure and (b) the analysis of the obtained data.

For an incident angle θ, which is half of the scattering angle 2θ in the reflectivity measurements, the X-ray momentum transfers along the surface normal could be presents as $q = \frac{4\pi}{\lambda} \sin \theta$. Hence the period of interference fringes of the reflected X-ray beams is related to the thickness d of the film via $2\pi / d$. And the roughness of the interfaces, which results in the dampling of reflevitity intensity, can be taken into account. [17] Fig.

2-8 shows the simulation results of reflectivity with different situations: ideal surface and film/substrate interface, surface roughness of 1 nm and ideal film/substrate interface, and ideal film surface with interfacial roughness of 1 nm. The simulated results reveal that the surface roughness of ZnO film has negative influence on the decay rate of the reflectivity curve, and the substrate roughness manily affects the amplitude of interference fringes.

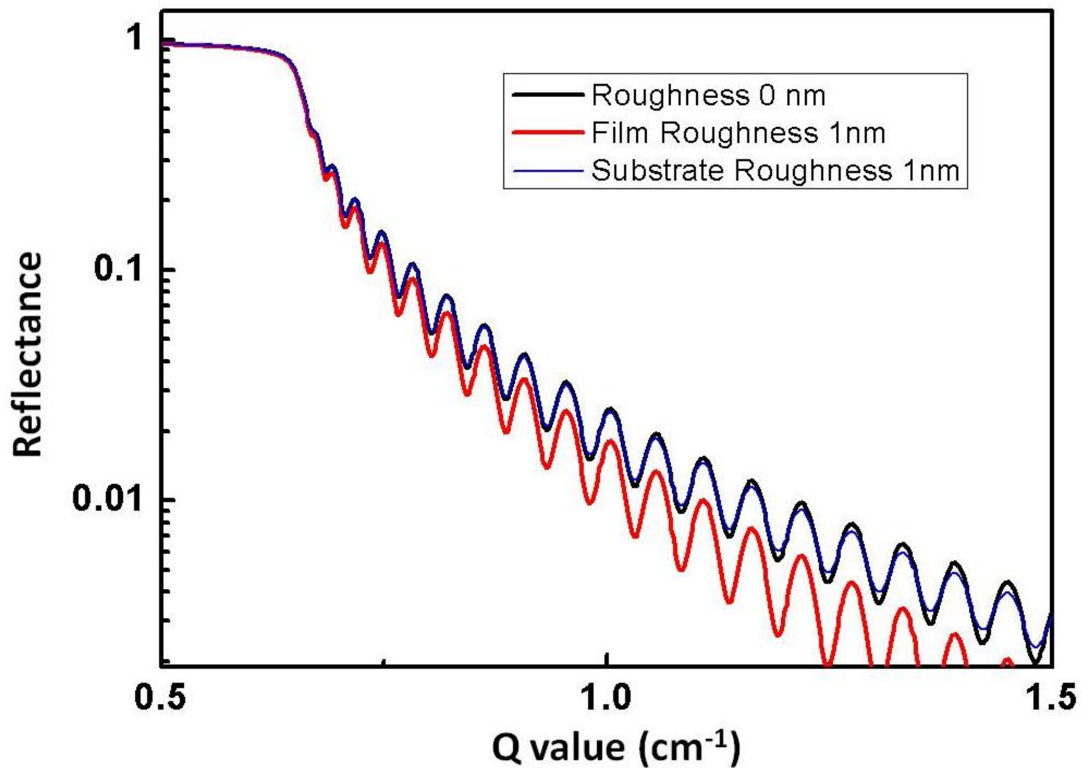

Fig. 2-8 Simulated XRR curves of the ZnO films on sapphire substrate with different R_{rms} values: ideal interface and surface, film roughness of 1 nm with ideal substrate roughness, and ideal surface with substrate roughness of 1 nm.

2.4 Transmission Electron Microscope

The TEM is a very powerful method to analyze the structure characteristics of the

crystalline material in the atomic level, which make implementation of the direct observation of crystal defect possible.

2.4.1 TEM setup

A schematic presentation of the microscope is shown in Fig. 2-9. [7] The TEM instrument consists of an electron gun connecting to a high voltage (typically about 100-300 kV) accelerating electronic filed to emit electrons. By using condensor lenses (magnetic lens), the electron beam is focused to a spot of the order of 1 mm on the specimen. The image is magnified more than 10^6 times in the bright filed image mode (Fig. 2-9 (a)). In selected area diffraction mode (Fig. 2-9 (b)), the electron diffraction patterns are formed on the final image screen. In bright field imaging, the image of a thin sample is formed by the electrons, which pass the film without diffraction, the diffracted electrons being stopped by a diaphragm. In the corresponding dark-field-imaging mode, a diffracted beam is used for imaging.

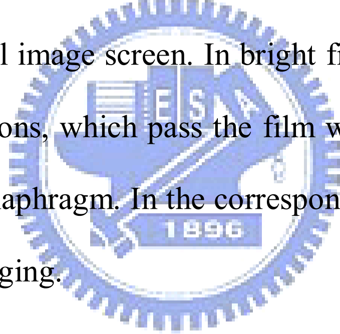

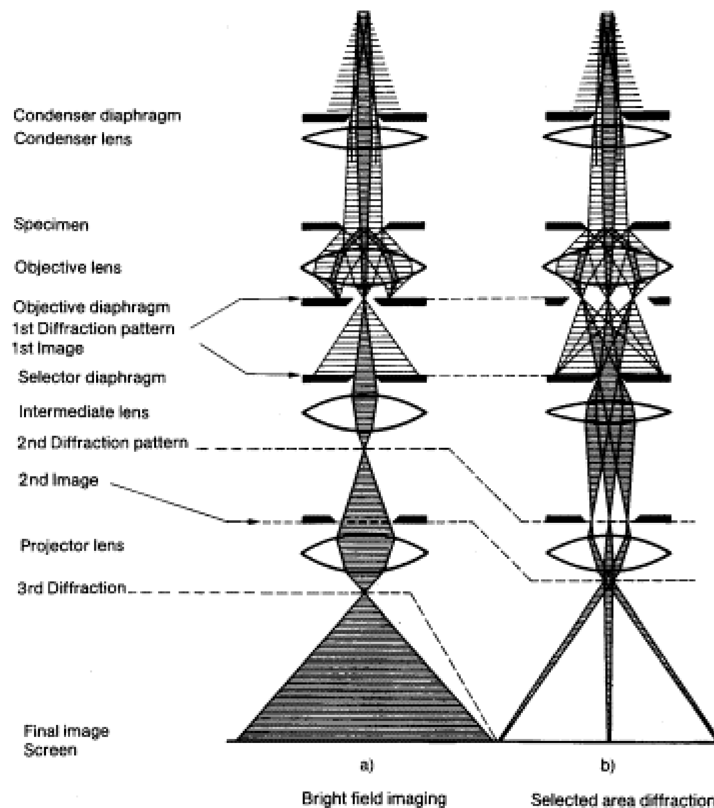

Fig. 2-9 The measurement setup of TEM in (a) bright field imaging and (b) selected area diffraction modes.

1896

2.4.2 Dark Field Image

Selected area electron diffraction (SAED), is a crystallographic experimental technique, which selects certain area of the specimen to obtain the diffraction pattern. The crystalline specimen is subjected to a parallel beam of high-energy electrons. Because the wavelength of high-energy electrons is close to the spacing of atoms in a crystal, the periodic atoms act as a diffraction grating to the electrons. As a result, the image on the screen of the TEM will be a series of diffraction spots (diffraction pattern), and each diffraction spot is corresponding to a satisfied diffraction condition of the crystal structure.

As a diffraction technique, SAED can be used to identify crystal structures and examine crystal defects. As shown in Fig. 2-10 below, the specimen holder is an objective aperture, which can be inserted into the beam path to block the electron beam except for the selected diffraction spot. [8] The diffraction spot, which is selected by the objective aperture can form the image on the screen is called dark-field (DF) images. Such an imaging mode is called the DF mode. In addition, the image formed by the unblocked spots including the direct beam and specific selected diffraction spots is called the bright filed (BF) image and the imaging mode is called the BF mode. Through these modes the TEM image can be formed by only the selected spot with a specific diffraction vector g.

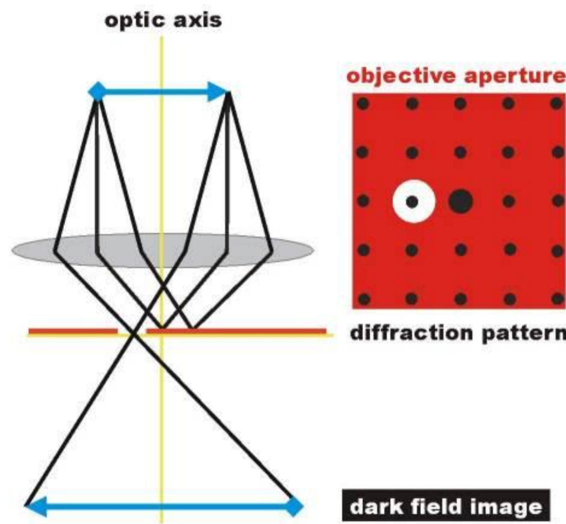

Fig. 2-10 The measurement setup of dark filed imaging with the selected spots with specific diffraction vector g.

2.4.3 Basal Stacking Fault Analysis by TEM

The most common crystal structure of ZnO epitaxial film is wurtzite structure, which has the atoms stacking sequence …$AaBbAaBbAaBb$… along the [0001] direction (c-axis direction), where Aa and Bb represent the planes with specific stacking positions of atom

layer and the capital letters represent the zinc atoms and the lowercase letters represent the oxygen atoms, the positions are shown in Fig. 2-11. [9] The stacking fault means that the ideal stacking sequence of wurtzite structure (…*AaBbAaBb*…) has the faults, such as the sequence …*AaBbAaBbCcBbCc*… which is termed as the *type-I* stacking fault. In addition, the stacking sequence of the zinc blend structure of ZnO is …*AaBbCcAaBbCc*… along the [111] direction.

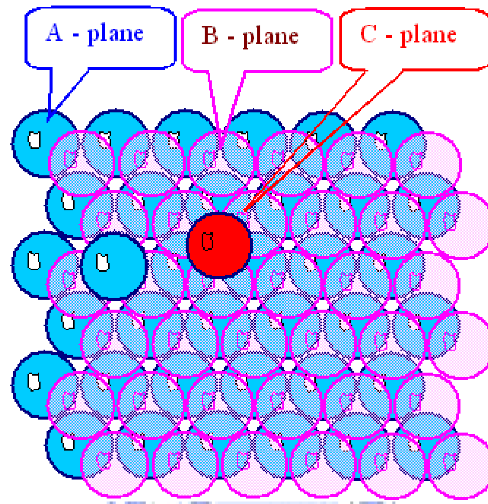

Fig. 2-11 Three kinds of planes with different atom stacking arrangements in ZnO material marked as A-, B-, and *C*-planes.

The BSF can be classified into four types: *type-I*, *type-II*, *type-III*, and *Extrinsic* SF. The scheme of the four types of stacking sequences are shown in Fig. 2-12. [10]

(a) *Type-I stacking fault* (I_1):

The type-I BSF is shown in Fig. 2-12(a). It is commonly expected to have the lowest formation energy. For the type-I SF, two stacking sequences are considered: …*AaBbCcBbCc*… and …*AaBbAaCcAaCc*…, both types of SF stacking sequences have the same energy.

(b) *Type-II stacking fault* (I_2):

The BSF has the stacking sequence of …*AaBbAaBbCcAaCcAaCc*…, which has the second lowest formation energy.

(c) *Type-III stacking fault*:

These are intrinsic BSFs, in which one of the Aa or Bb layers occupied by the Cc position: …AaBbAaCcAaBb….

(d) *Extrinsic stacking fault*:

These SFs have the additional Cc layer inserted in the midst of the normal stacking sequence: …AaBbCcAaBb….

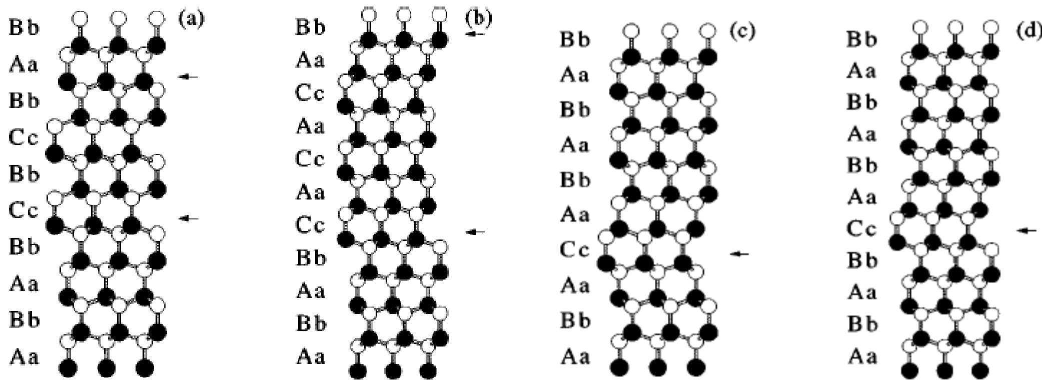

Fig. 2-12 Four types of stacking faults in ZnO: (a) type I, (b) type II, (c) type III, and (d) extrinsic. The arrows indicate the position of the stacking faults and the black and white circles denote zinc and oxygen atoms, respectively.

Depending on the type of error in stacking sequence or equivalently the displacement vector *R* defines the relative displacement between the unfaulted lattices above and below the fault. In wurtzite crystal structure the displacement vectors associated with the I_1, I_2 and Extrinsic type of BSFs are $\frac{1}{6}\langle 2\bar{2}03 \rangle$, $\frac{1}{3}\langle 1\bar{1}00 \rangle$, and $\frac{1}{2}\langle 0001 \rangle$, respectively; [11-13] but the type-III BSF has no displacement vector. From the TEM image of a crystal, the intensity of the electron beam diffraction could be described as following:

$$\phi_g = \frac{\pi i}{\xi_g} \int_0^t e^{-2\pi i \vec{g}\cdot\vec{R}} e^{-2\pi i s z} dz \; .$$

In this formula, the part of the phase factor is as the following:

$$e^{-2\pi i \vec{g}\cdot\vec{R}} \; .$$

According to this formula, a stacking fault will be out of contrast if the dot product of its displacement vector R with the diffraction vector g used for imaging equals to 2πn, where n = 0, ±1, ±2, …. [14, 15] Consequently, all three types of stacking faults are visible in image with $g = (10\bar{1}1)$ and out of contrast as g = (0002). In the case of $g = (10\bar{1}0)$, only intrinsic stacking faults of types I_1 and I_2 are in contrast. Table 1 shows the visibility of the stacking faults with different g vectors.

	(0002) $\{11\bar{2}0\}$	$(10\bar{1}1)$	$(10\bar{1}0)$
Type-I	Invisible	Visible	Visible
Type-II	Invisible	Visible	Visible
Extrinsic	Invisible	Invisible	Visible

Table. 1 The visibility of the BSFs in TEM dark-field imaging with different selected g vectors.

2.5 Atomic force microscopy

Atomic force microscopy (AFM) is a very high-resolution type of scanning probe microscopy with demonstrated resolution on the order of fractions of a nanometer. The

brief setup of the AFM is shown in Fig. 2-13. The AFM consists of a cantilever with a sharp tip (the radius of curvature is on the order of nanometers), which is used to scan the specimen surface. When the tip is brought into the vicinity of the specimen surface, the forces between the tip and the surface deflects the cantilever according to Hooke's law. Depending on the scanning modes, the forces that are measured in AFM include mechanical contact force, van der Waals force, electrostatic force, magnetic force, etc. Along with force, additional quantities may simultaneously be measured through the use of specialized types of probe. Typically, the deflection of the cantilever is measured by using the photodiode to detect the laser spot reflected from the surface of the cantilever. The sample is mounted on a piezoelectric device to move the sample in the z direction for maintaining a constant force, and in the x and y directions for scanning the sample.

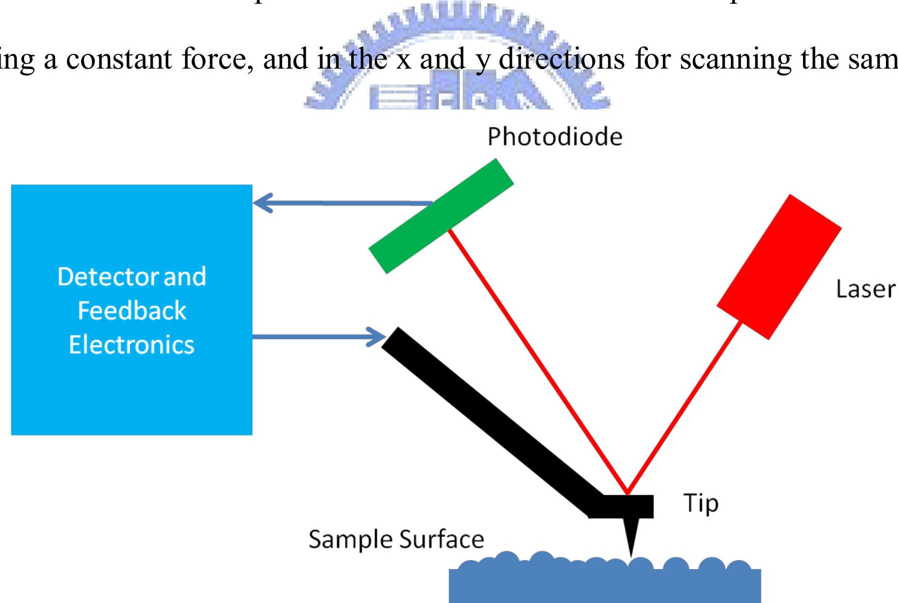

Fig. 2-13 The measurement setup of the atomic force microscope.

References

[1] U. Ozgur, Ya. I. Alivov, C. Liu, M. A. Reshchikov, S. Dogan, V. Avrutin, S.-J. Cho, and H. Morkoc, J. Appl. Phys. 98, 041301 (2005)

[2] S. Yang, C. C. Kuo, W.-R. Liu, B. H. Lin, H.-C. Hsu, C.-H. Hsu, and W. F. Hsieh, Appl. Phys. Lett. 100, 101907 (2012)

[3] J.-R. Chen, T.-C. Lu, Y.-C. Wu, S.-C. Lin, W.-F. Hsieh, S.-C. Wang, and H. Deng, Opt. Express 19, 4101 (2011)

[4] Y. Yan, G. M. Dalpian, M. M. Al-Jassim, S.-H. Wei, Phys. Rev. B. 70, 193206 (2004).

[5] Y. T. Rebane, Y. G. Shreter, M. Albrecht, Phys. Status Solidi A 164, 141 (1997).

[6] Elza Bontempi's Science Page from http://dimgruppi.ing.unibs.it/

[7]http://inano.au.dk/research/competences-and-facilities/nanotools/transmission-and-scanning-electron-microscopy/

[8] http://www.microscopy.ethz.ch/

[9] http://www.tf.uni-kiel.de/matwis/amat/def_en/kap_5/backbone/r5_4_1.html

[10] C. Stampfl and Chris G. Van de Walle, Phys. Rev. B. 57, R15052 (1998).

[11] Stampfl, C.; Van de Walle, C. G., Phys. Rev. B 1998, 57, R15052.

[12] Gerthsen, D.; Litvinov, D.; Gruber, T.; Kirchner, C.; Waag, A., Appl. Phys. Lett. 2002, 81, 3972.

[13] Vennegues, P.; Chauveau, J. M.; Korytov, M.; Deparis, C.; Zuniga-Perez, J.; Morhain, C., J. Appl. Phys. 2008, 103, 083525.

[14] Wang, X. Q.; Iwaki, H.; Murakami, M.; Du, X. L.; Ishitani, Y.; Yoshikawa, A., Jpn. J. Appl. Phys. 2003, 42, L99.

[15] Chen, Y. F.; Bagnall, D. M.; Koh, H. J.; Park, K. T.; Hiraga, K.; Zhu, Z. Q.; Yao, T., J. Appl. Phys. 1998, 84, 3912.

[16] A. Ashrafi and C. Jagadish, J. Appl. Phys. 102, 071101 (2007)

[17] B. Cull, Y. Shi, S. Kumar, r. Shih, and J. Mann, Phys. Rev. E 51, 526 (1995)

1896

Chapter 3 Experiments

3.1 Atomic Layer Deposition System and Growth Procedure

The substrates are cleaned by sequential D.I. water/acetone/D.I. water rinse for 5min/5min/5min and then blew dry with N_2 gas. The cleaned substrates are then loaded into the ALD reactor (SYSKEY Ltd., Taiwan), heated to 200°C, and held at this temperature for 30 min. Diethylzinc (DEZn with chemical formula of $Zn(C_2H_5)_2$ and purity 4N8) and H_2O (D. I. water of resistivity 18 MΩ·cm), kept in reservoirs at 25°C, are used as zinc and oxygen precursors, respectively. The growth cycle consists of precursor exposures and N_2 purge, which follows the sequence of DEZn/N_2/H_2O/N_2 with corresponding duration of 5s/15s/5s/15s. After each N_2 purging, the reactor is pumped down to ~ 1×10^{-2} torr by a mechanical pump. Precursor introduction is done by opening the inlet valve between the reservoir and reactor chamber while the outlet valve is closed; no carrier gas was employed. The pressures of the DEZn and H_2O in the reactor chamber were approximately 7 and 17 torr, respectively, monitored by a vacuum gauge. The substrate temperature was maintained at 200°C under the vacuum of 1~2 torr during the deposition. The reaction repeated 200 ~ 400 times for all the studied samples. Ideally, two cycles of reaction yield a unit cell of ZnO along the *c*-axis which means the 200 cycles would lead to 100 unit cells along the growth direction equivalent to a thickness of about 52 nm. Thermal annealing was performed at temperatures varying from 300 to 800°C for 1.5 hrs in pure oxygen gas at 1 atm.

3.2 X-ray Diffraction

The X-ray measurements were conducted using a four-circle diffractometer at

beamline BL13A of National Synchrotron Radiation Research Center (NSRRC) Taiwan with incident wavelength 1.02473 Å, which is shown in Fig. 3-1. Two pairs of slits located between the sample and a NaI scintillation detector were employed and yielded a typical resolution of better than 1×10^{-3} $Å^{-1}$.

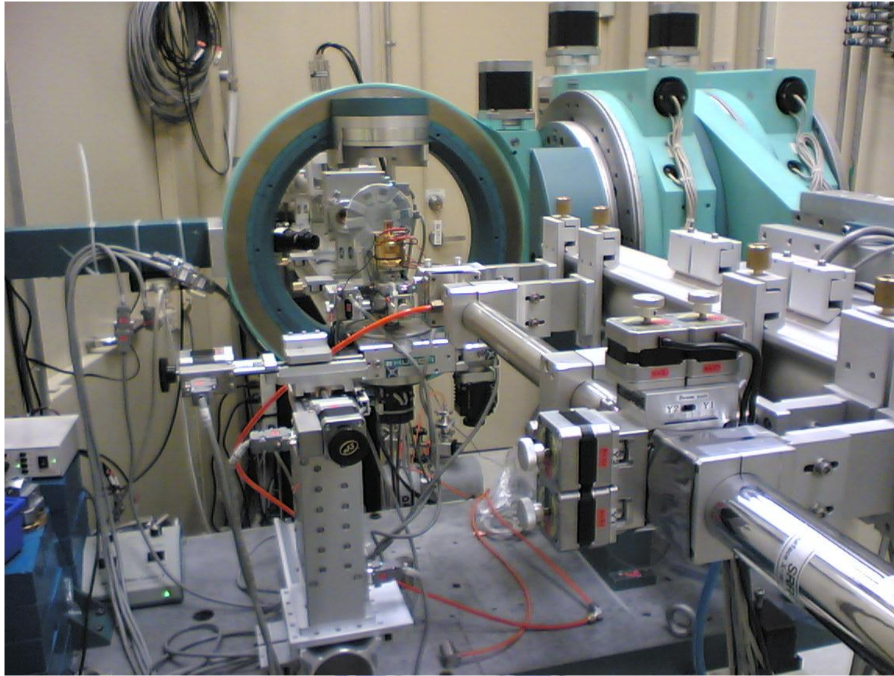

Fig. 3-1 The four-circle diffractometer in NSRRC at beamline BL13A.

3.3 Atomic Force Microscope

Surface morphology and roughness of the ZnO layer were measured by the commercial Scanning Probe Microscope (Veeco Dimension 5000), which is shown in Fig. 3-2. The surface morphology images of the ZnO layers were scanned by the tapping mode, and the roughness values were estimated by analyzing the images of morphology.

Fig. 3-2 Veeco Dimension 5000 Scanning Probe Microscope

1896

3.4 Transmission Electron Microscopy

Cross sectional TEM specimens with thickness of about 90±10 nm were prepared by focused ion beam (FIB) shown in Fig. 3-3(a). TEM images were taken with a Philips TECNAI-20 field emission gun type TEM, which is shown in Fig. 3-3(b). The structural defects of the ZnO thin films were analyzed using transmission electron microscopy (TEM). TEM specimens with a thickness ~80 nm were prepared by using a focused ion beam (FEI Helios 400S). High resolution TEM (HR-TEM) images were captured by using the JEOL JEM-2100F TEM with accelerating voltage 200 kV and the selected area electron diffraction (SAED) patterns were taken with a camera length of 300 mm and electron beam focused at the interface between ZnO film and sapphire substrate.

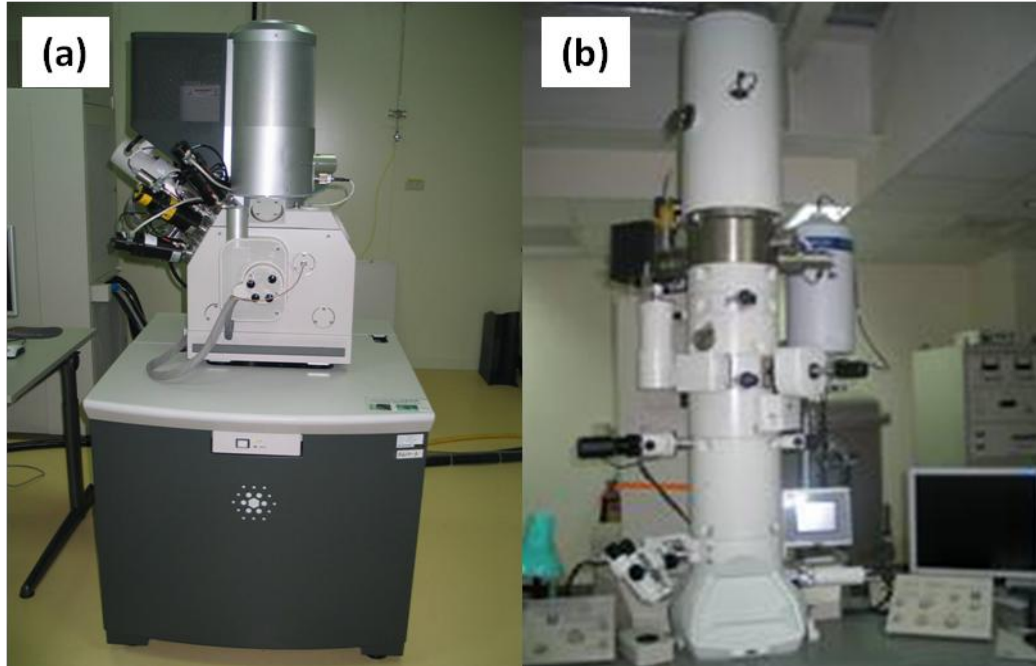

Fig. 3-3 The TEM measurement instruments: (a) the focused ion beam and (b) Philips TECNAI-20 field emission gun type TEM.

3.5 Photoluminescence

3.5.1 Low Temperature Photoluminescence

The PL measurements were carried out by using a He-Cd laser at 325 nm as the excitation source, and the sample is placed in a closed cycle cryogenic system. The laser beam is introduced onto the sample by using the mirror while the emission light is collected by using a convex lens. The emission is then conducted into a spectrometer (TRIAX 320) equipped with a photo-multiplier tube. The sketch of this setup is shown in Fig. 3-4.

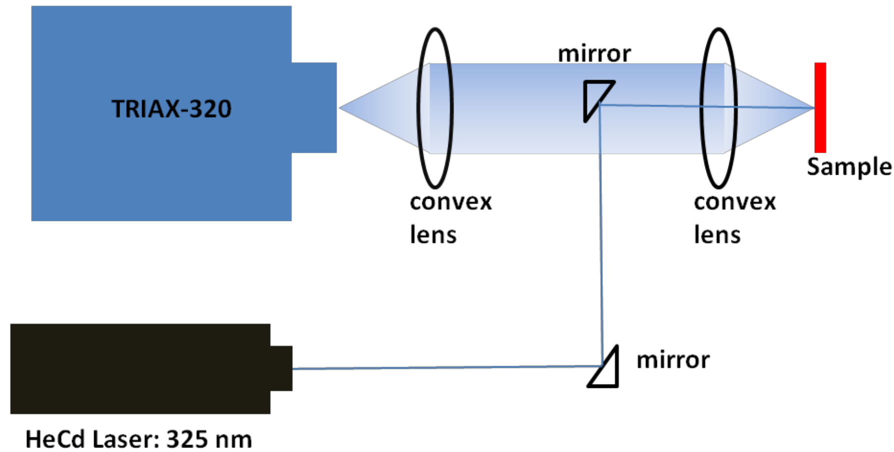

Fig. 3-4 The sketch of the photoluminescence measurement setup.

3.5.2 Time Resolved Photoluminescence Measurement

Stationary PL spectra were measured with the fourth harmonic (λ_{exc} = 266 nm) of a continuous wave Nd:YVO_4 laser as the excitation source. The PL signal was dispersed by a 0.55 m monochromator and detected by a UV enhanced liquid-nitrogen-cooled charge coupled device camera. For the transient PL measurements the third harmonic (λ_{exc} = 266 nm) from a Ti:sapphire femtosecond pulsed laser (pulse length 150 fs) was employed. The PL transients were detected by a UV sensitive Hamamatsu streak camera system with a temporal resolution better than 20 ps. The samples were placed in a variable-temperature cryostat for measurements in the temperature range 2–300 K. The setup of the TRPL system is shown in Fig. 3-5.

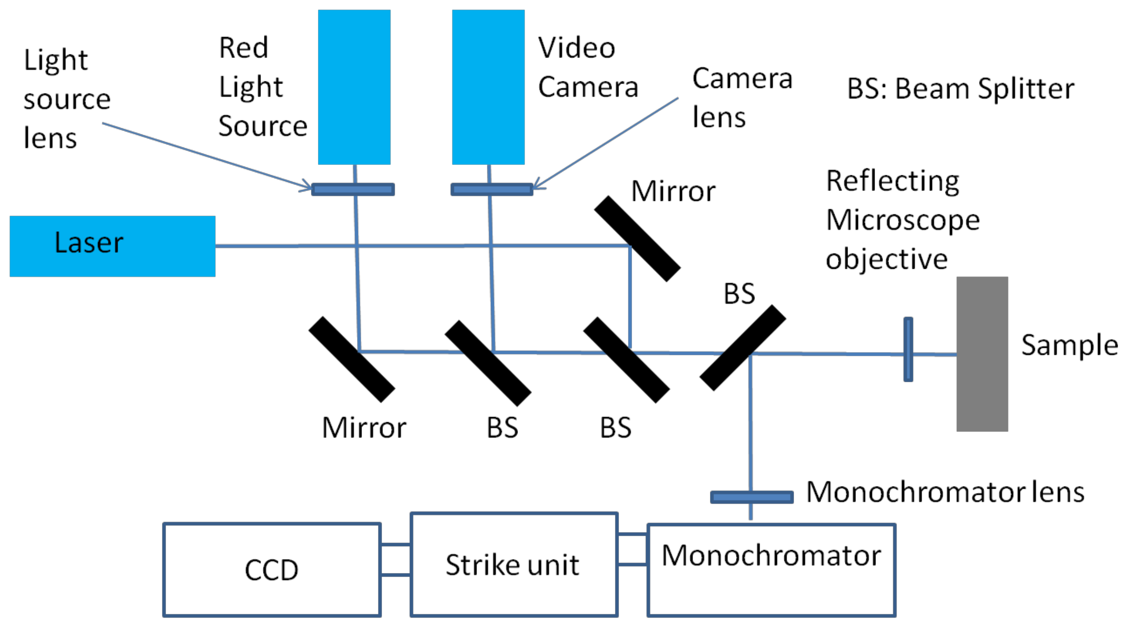

Fig. 3-5 The sketch of the TRPL measurement setup.

Chapter 4 c-plane ZnO grown on c-plane Sapphire by ALD

The c-plane sapphire (α-Al_2O_3) with a rhombohedral crystal structure and lattice constants a = 4.759 Å and c = 12.992 Å is commonly adopted as the substrate for ZnO growth because the reasonable costs and good quality of the ZnO obtained. On c-sapphire, ZnO preferentially grows with its c-axis aligned with the c-axis of substrate. Molecular beam epitaxy (MBE), metal organic chemical vapor deposition (MOCVD) [6, 10] and pulsed laser deposition (PLD)[11-13] have been widely employed to grow ZnO epitaxial films with high structural quality. Recently, atomic layer deposition (ALD) has attracted much attention for its application in ZnO growth. [14-21] ALD is a technique based on the sequential use of self terminating gas-solid reactions that bear many practical advantages such as large-area deposition, high uniformity, high reproducibility, high covering ratio, low growth temperature, and the ability of producing sharp and tailored interfaces. [22] Moreover, the merit of accurate thickness control renders ALD particularly suitable for the fabrication of high quality multi-quantum-well (MQW) structures. In this chapter, we will discuss their crystal structure and optical properties of ZnO epi-films on c-plane sapphire fabricated in use of ALD.

4.1 XRD Measurements

4.1.1 2θ/θ Scan

Figure 4-1 Illustrates the radial scan (θ-2θ scan) along surface normal of an as-deposited ZnO layer and the samples annealed at 300, 700, and 800°C.

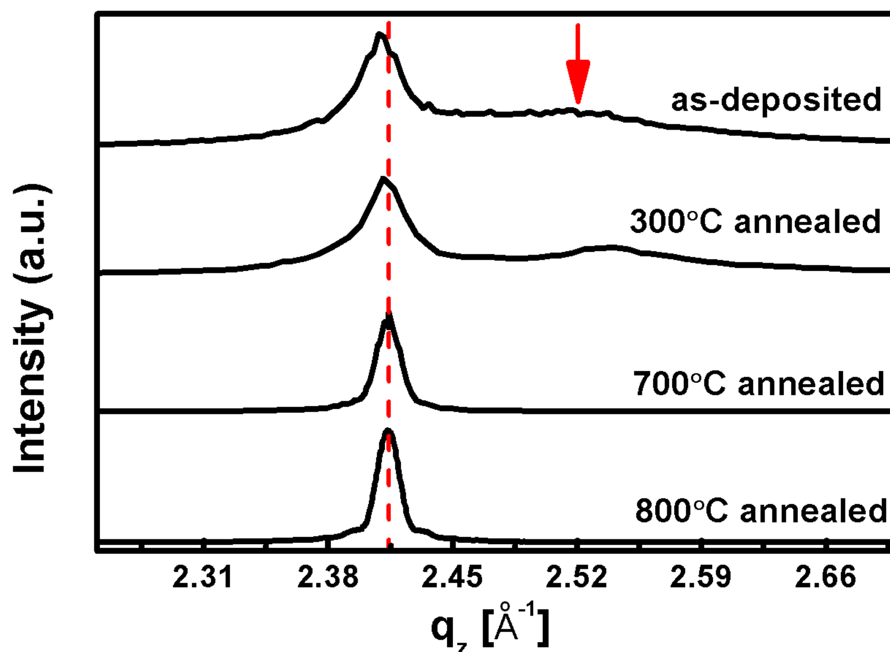

Fig. 4-1 The radial scans (θ-2θ scan) along surface normal of the as-deposited ZnO and those annealed at 300°C, 700°C, and 800°C. The red broken line marks the position of bulk ZnO (0002) reflection. The arrow indicates the location corresponding to the inter-planar spacing of ZnO $(10\bar{1}1)$.

The pronounced peak centered at q_z, momentum transfer along surface normal, ~ 2.409 Å^{-1} observed in the as-deposited sample yields an interplanar spacing ~ 2.608 Å. This value is 0.24% larger than the d spacing of bulk ZnO (0002) planes, d_{0002}; we assigned this peak to ZnO (0002) reflection. At higher q_z side, a broad shoulder centered at ~2.53 Å^{-1} is attributed to the ZnO $(10\bar{1}1)$ reflection. Besides the reflections from sapphire substrate, no other peak originated from ZnO was observed, indicating the as-deposited ZnO layer is predominantly c-plane oriented with a minor $(10\bar{1}1)$ orientation coexisting. It is worth mentioning that the $(10\bar{1}0)$ plane was reported to be the preferential surface orientation in many ALD grown ZnO films, especially those

grown on substrates such as Si(001)[15, 16] and fused silica glass [23] or deposited at low temperatures. [19] No trace of the $(10\bar{1}0)$ orientated grains was detected in our samples which is attributed to the hexagonal symmetry of the *c*-sapphire, which strongly favors the growth of *c*-plane ZnO with compatible symmetry. [17-18] The other factor in favor of the growth of high quality *c*-plane ZnO is the long purging time used in our case. The simultaneous enhancement of (0001) growth and improvement of crystalline quality with prolonged purging time was reported by A. Wojcik *et. al.*. [19] Longer purging time provides not only more complete removal of physically adsorbed surface species and volatile by-product but also longer time for element diffusion to prepare a better surface for subsequent reaction.

Upon thermal annealing, the ZnO $(10\bar{1}1)$ reflection disappears in company with the sharpening up and intensity enhancement of the ZnO (0002) reflection, a sign of increasing structural coherence along the growth direction. Moreover, the lattice parameter along the c axis systematically decreases with increasing annealing temperature as revealed by the shift of the (0002) reflection to the higher q_z side and approaches the bulk value, as marked by the dashed line, to within 0.02% after 800°C annealing.

4.1.2 Rocking Curve

The ZnO (0002) rocking curves of the as-deposited and annealed samples, with the intensity normalized to corresponding peak intensity, are illustrated in Fig. 4-2(a).

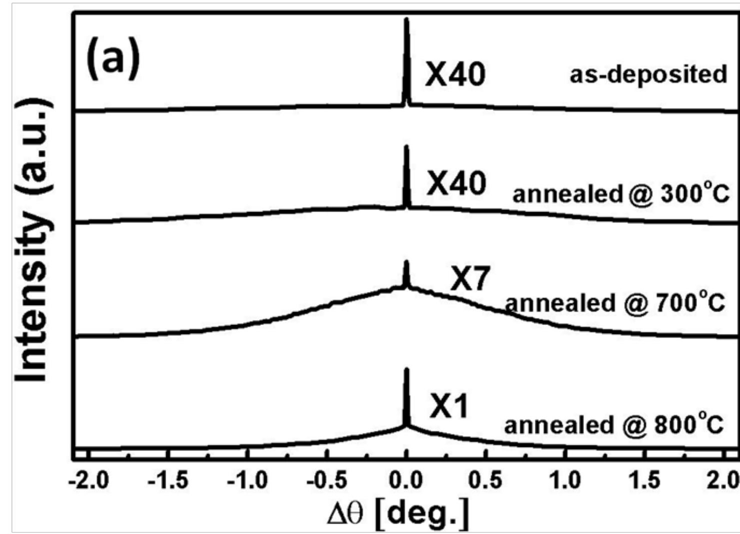

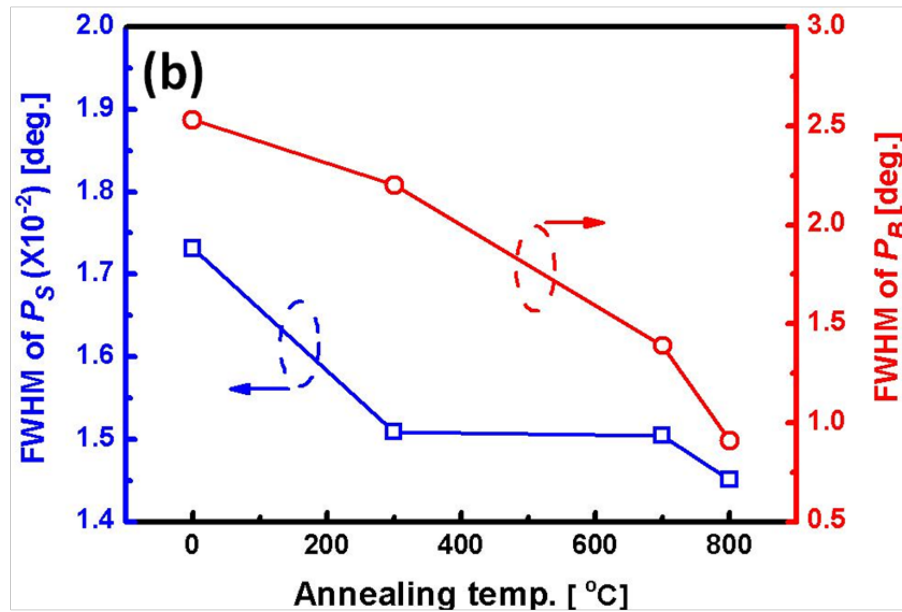

Fig. 4-2 The θ-rocking curves of (a) the as-deposited and annealed ZnO layers and (b) the variation of the FWHM of P_S and P_B as a function of annealing temperature. Each curve is a superposition of a sharp (P_S) and a broad peak (P_B).

All the curves are composed of a shape peak (P_S) with typical full width at half maximum (FWHM) of less than 0.02° superimposed with a broad peak (P_B) whose line

width is two orders of magnitude larger than the central sharp peak. The broad component is attributed to the diffuse scattering from the structural defects, such as dislocations, and misoriented grains. Such a pronounced diffuse component has hardly been observed in ZnO epi-layers grown by PLD or MOCVD and indicates the intrinsic difference between the structural characteristics of the ZnO layers grown by ALD and other methods. Upon annealing the FWHM of the sharp component showed mild improvement from 0.017° to 0.015°, as shown in Fig. 4-2(b). Such a sharp peak has also been reported in sample grown by the MBE method having FHWM of about 0.005°. [59] These values are comparable to the FWHM of sapphire (0006) reflection, 0.013°. In contrast, the FWHM of broad component exhibits a monotonic reduction from 2.53° for the as-deposited film to 0.91° for the 800°C-annealed sample and their integrated intensity also drastically decreases with elevated annealing temperature, evidencing the significant improvement of structural perfection by the thermal treatment. The ZnO layer was also reported grown on GaN substrate by ALD with small lattice mismatch and the FWHM of the rocking curve data is estimated to be 0.09º. [60]

4.1.3 Azimuthal Cone Scans

In order to determine the epitaxial relationship between the ZnO layers and the substrates, we performed azimuthal cone scans (ϕ -scans) across the off-normal ZnO $\{10\bar{1}1\}$ and sapphire $\{11\bar{2}6\}$ reflections, as illustrated in Fig. 4-3. For both as-deposited and annealed ZnO layers, the scans across the ZnO $\{10\bar{1}1\}$ reflections show six fold symmetry, confirming the hexagonal symmetry. The angular positions of these peaks are offset from that of the six sapphire $\{11\bar{2}6\}$ reflections by 30° and yield the in-plane relationship of $\{10\bar{1}0\}_{ZnO} \parallel \{10\bar{1}0\}_{Al_2O_3}$, the “aligned orientation”.

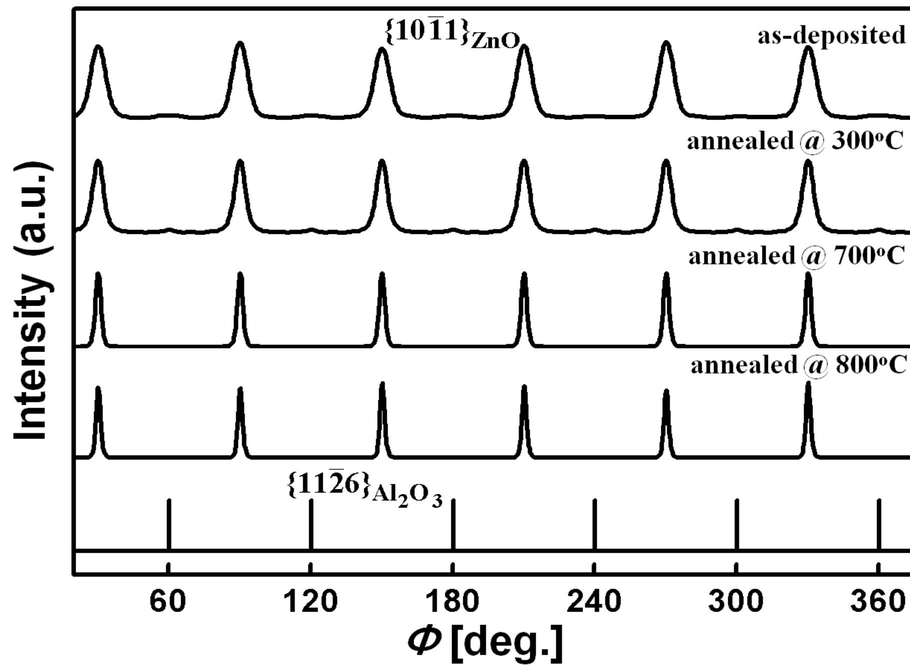

Fig. 4-3 The ϕ-scan across the off-normal ZnO $\{10\bar{1}1\}$ reflection of as-deposited and annealed ZnO layers, together with the ϕ-scan across sapphire $\{11\bar{2}6\}$ shown at the bottom.

It is also noticed that the FWHM of the ZnO $\{10\bar{1}1\}$ peaks drastically decreases from 6.75° for the as-deposited sample to 2.48° for the sample after 800°C thermal treatment, again indicating the significant improvement in twist deformation upon annealing. Carefully examining the ϕ-scan of the as-deposited sample, we found another set of weak peaks with six-fold symmetry appearing at the same angular position as sapphire $\{11\bar{2}6\}$. This observation reveals the existence of a small fraction of c-plane ZnO has $\{10\bar{1}0\}_{ZnO} \parallel \{11\bar{2}0\}_{Al_2O_3}$ orientation, the "twisted orientation". Determined from the integrated intensity, the fraction of the minor twisted orientation decreases with annealing temperature from ~4.2% for as-deposited film to less than

0.03% after 800ºC thermal annealing.

The twisted orientation, in which the lattice of ZnO is aligned with the oxygen sub-lattice in sapphire, is most commonly observed for ZnO epi-films grown on *c*-sapphire. [11, 24-26] Its lattice mismatch with sapphire, 18.3%, is smaller than the 31.8% of the aligned orientation, in which the ZnO lattice is aligned with the Al sublattice in sapphire. Intuitively, the twisted orientation is energetically favorable and indeed most of the ZnO epi-layers grown on *c*-plane sapphire by PLD and MOCVD, VPE have this orientation. [10, 25, 26] The aligned in-plane orientation has been reported on ZnO epi-films grown by PLD and magnetron sputtering at low deposition temperatures ($T < 600°C$). [27-30] In those works, the fraction of the domains with the aligned orientation increases with decreasing growth temperature and/or lower deposition rate.

The orientation of the epi-films is a result of the competition between the interfacial bonding, elastic energy and surface energy. In view of the energy of interfacial bonding, the much larger bond energy of Al-O (511 kJ/mol) bond than the Zn-O bond (271 kJ/mol) favors the O-Al–O-Zn configuration, i.e., the O in ZnO bonds with the Al in sapphire substrate, and leads to the alignment of Zn terminated ZnO lattice with Al sublattice. [27] However, from the aspect of smaller lattice mismatch and higher thermodynamic stability of O-terminated ZnO surface,[31] the configuration with twisted orientation is preferred. I. Ohkubo *et al.*, attributed the prevalence of the aligned orientation at low temperatures to Al termination of sapphire surface and the dominance of local interface energy when the growth process in kinetics limited. [24, 26] According to this argument, the low operation temperature of ALD favors the formation of observed aligned orientation but the interfacial bonding mechanism should be different because of the alternative formation of Zn and O atomic layers during two separate half reactions.

The topmost surface of a sapphire wafer after wet-cleaning is terminated by hydroxyl groups due to its high stability. It is a known difficulty of creating an OH free sapphire surface not mentioning the surface prepared by wet-cleaning and mild heating pretreatment adopted in our process. [32] According to the ALD growth sequence, the zinc precursor DEZn with the chemical structure of CH_3-CH_2-Zn-CH_2-CH_3 is first supplied onto the substrate surface. One ethyl of the DEZn reacts with the hydroxyl at the sapphire surface and leaves the zinc atom bonded with the oxygen at the substrate surface. Volatile organic by-product Ethane is pumped away and the residual functional group ethyl prevents the continuous growth of deposited material due to the self-limiting effect. Subsequently introduced H_2O reacted with ethyl group and form -Zn–O-H terminated surface. [25] After this point, the rest of the film growth can be considered as homoepitaxy. The initial bonding of DEZn to sapphire, -Al–O-Zn-CH_2-CH_3, anchors the orientation of the ZnO layer, which follows the atomic arrangement of the Al sublattice in sapphire and yields the observed aligned orientation, i.e. $\{10\bar{1}0\}_{ZnO} \parallel \{10\bar{1}0\}_{Al_2O_3}$.

4.2 TEM Analysis

It is well known that structural properties obtained by XRD are an ensemble average over the macroscopic illuminated volume, typical of mm^3. On the contrary, microscopy probes microscopic features over a much more localized region. As a complementary, we also performed TEM measurements on the ZnO epi-layers. Illustrated in Fig. 4-4 (a) is a cross sectional TEM image taken along the $[11\bar{2}0]_{Al2O3}$ zone axis, in which ZnO grains with planes of 5.2 Å interplanar spacing parallel to the interface can be well resolved.

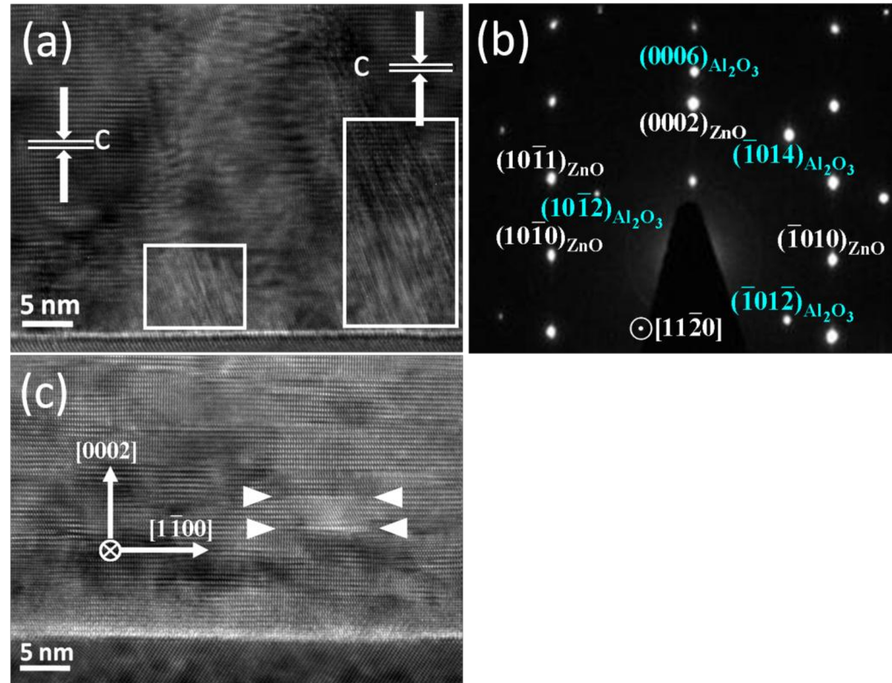

Fig. 4-4 The cross sectional TEM image of (a) the as-deposited ZnO epi-layer along the $[11\bar{2}0]$ zone axis, (b) the SAED pattern, and (c) the image of 800°C annealed sample taken under the same pole.

1896

The selected area electron diffraction (SAED) pattern (Fig. 4-4(b)) confirmed the $(0001)<1\bar{1}00>_{ZnO}||(0001)<1\bar{1}00>_{Al2O3}$ orientation in agreement with XRD observation. However, numerous misoriented grains, as enclosed by the rectangles in Fig. 4-4(a) and defects of various kinds distribute throughout the grown film. Figure 4-4(c) is the micrograph of the 800°C annealed sample taken under the same pole, which exhibits drastic structural improvement. Moreover, many contrast lines lying in the basal planes with lateral extension of the order of 10 nm (some of them are marked by arrows) were observed. These lines were verified to be basal plane stacking faults as described below and represented the majority of structural defects found in annealed ALD grown *c*-ZnO

epi-films.

To characterize the nature of the lateral lines, we performed diffraction contrast analysis on the images of the 800°C annealed sample. The bright field images of the same region taken along $[11\bar{2}0]$ pole and with diffraction vector g set to $(10\bar{1}1)$, (0002), and $(10\bar{1}0)$ are shown in Fig. 4-5 (a), (b) and (c), respectively.

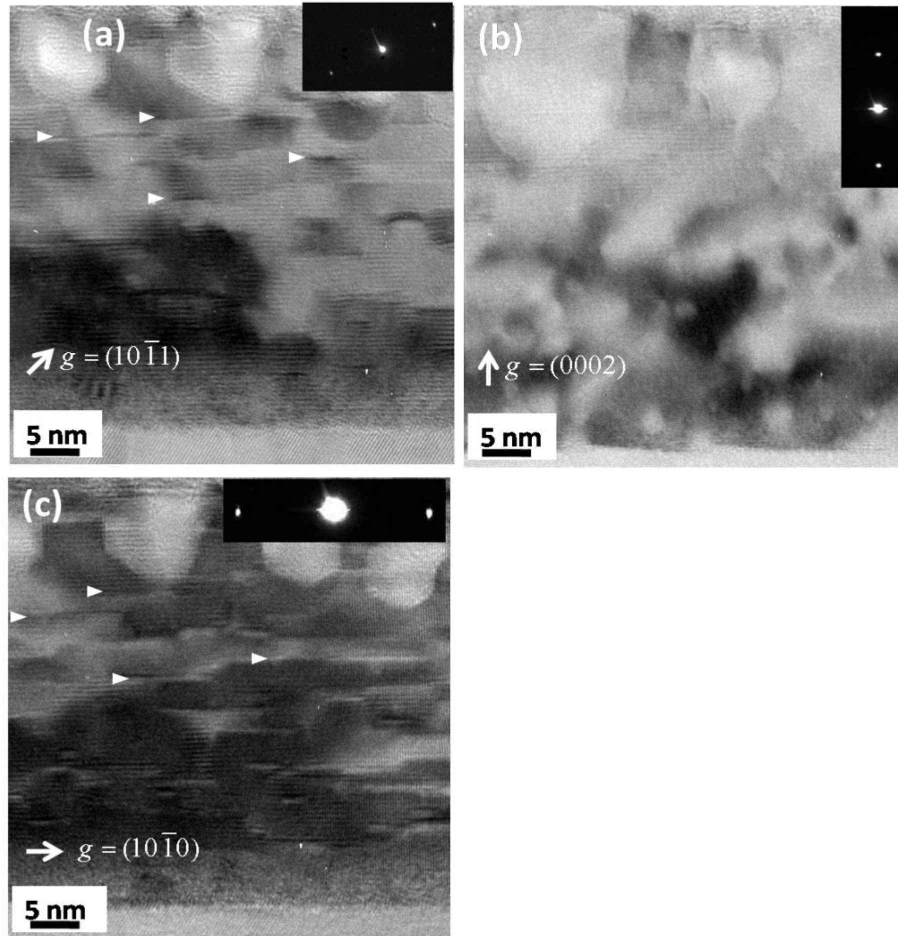

Fig. 4-5 The bright-filed images of the ZnO layer annealed at 800°C with diffraction vector g set to (a) $(10\bar{1}1)$, (b) (0002), and (c) $(10\bar{1}0)$. The insets show the corresponding diffraction peaks used under two-beam condition.

Depending on the type of error in stacking sequence or equivalently the displacement

vector R, which defines the relative displacement between the unfaulted lattices above and below the fault, the basal plane stacking faults in wurtzite crystal structure are generally divided into three types: two intrinsic ones named I_1 and I_2 and an extrinsic one named E. The displacement vectors associated with the I_1, I_2 and E type of basal plane stacking faults are $\frac{1}{6}\langle 2\bar{2}03 \rangle$, $\frac{1}{3}\langle 1\bar{1}00 \rangle$, and $\frac{1}{2}\langle 0001 \rangle$, respectively. [33-35] According to the extinction rules for stacking faults in TEM image, a stacking fault will be out of contrast if the dot product of its displacement vector R with the diffraction vector g used for imaging equals to $2\pi n$, where $n = 0, \pm1, \pm2, \ldots$ [34, 35] Consequently, all three types of stacking faults are visible in image with $g = (10\bar{1}1)$ and out of contrast as $g = (0002)$. In the case of $g = (10\bar{1}0)$, only intrinsic stacking faults of types I_1 and I_2 are in contrast. Examining the images taken under different diffraction vectors, we found about all the lateral lines visible in Fig. 4-5 (a) with $g = (10\bar{1}1)$ become out of contrast in Fig. 4-5 (b) with $g = (0002)$, confirming that basal plane stacking faults are indeed the major structural defects in the 800°C annealed sample. Furthermore, the absence of obvious difference in the spatial distribution of the lines found in images taken under $g = (10\bar{1}1)$ and $(10\bar{1}0)$, shown respectively in Figs. 4-5(b) and (c), reveals that the stacking faults belong to intrinsic type. Unfortunately, we cannot further verify which type of those stacking faults, I_1 or I_2. These lines are due to limited accessible diffraction vector under experimental geometry.

Unlike the ZnO epi-layers grown by PLD [12] and p-MBE [26] on *c*-sapphire where edge-type threading dislocations are the dominant structural defects in the film bulk, basal plane stacking faults are the majority of structural defects found in ALD grown *c*-ZnO epi-films. This also explains the small line width in θ-rocking curve of ZnO (0002)

reflection, which is not sensitive to the basal plane stacking faults. The diversity in characteristic structural features is related to the fundamental difference in the growth mechanism of those methods. In the case of PLD deposition, a plume of materials liberated from the target, consisting of a variety of energetic species, such as atoms, ions and small clusters of the ZnO are deposited on the surface and the growth of ZnO film on *c*-sapphire proceeded via island nucleation followed by lateral extension. [36] Such a growth mode results in a film of a columnar structure surrounded by grain boundaries with high density of threading dislocations. [12] In contrast, the intrinsic layer-by-layer growth nature of the ALD method unfavors the initial island nucleation and suppresses the formation of threading dislocations. Apparently, 800°C annealing results in the grain growth and stimulates the precipitation of point defects such as vacancies or interstitials and/or the dissociation of dislocations together with the slip of partial dislocations, which are known as the most likely mechanisms for the generation of basal plane stacking faults. [34]

4.3 AFM Measurements

In additional to crystalline structure, we also studied the effect on the surface morphology by thermal treatment. Voids were found in some areas near the film/air interface in the cross section TEM micrographs of the annealed sample (not shown). This explains the increase of surface roughness and the decrease of mass density near the film surface region in the annealed samples as revealed by x-ray reflectivity measurements. Figures 4-6(a) and (b) show, respectively, the surface morphology before and after 800°C annealing measured by AFM; Figs. 4-6(c) and (d) are the corresponding section profiles

of the scans along surface. Grain growth and the development of voids between the grains are induced by thermal treatment and lead to the increase of root-mean-square roughness from 1.64 to 5.75 nm. Similar variation of the morphology and increase of grain size resulted from the post annealing have also been reported by other groups and are attributed to the recrystallization of the ZnO grains. [16-18]

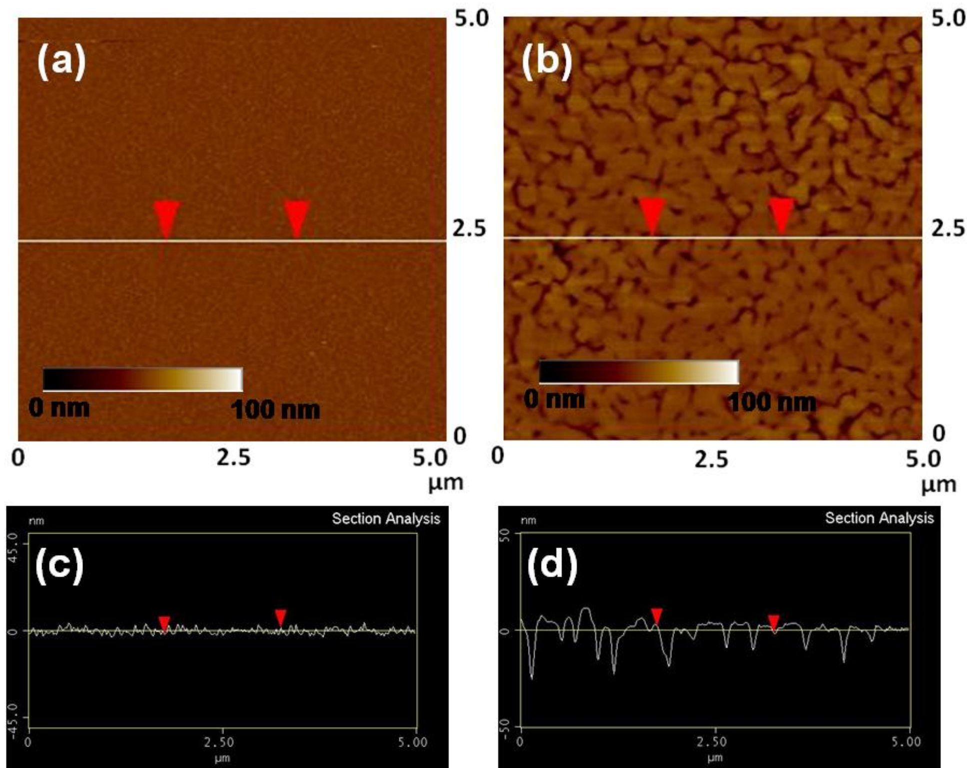

Fig. 4-6 The AFM images of the (a) as-deposited and (b) annealed ZnO layers with the scan image profiles of the as-deposited and annealed samples shown in (c) and (d), respectively.

4.4 Photoluminescence

To examine the optical properties of the ZnO layers, we performed low temperature

(10 K) PL measurements. The PL spectra are illustrated in Fig. 4-7(a). For comparison a spectrum taken from a 200 nm thick PLD-grown *c*-plane ZnO film with the BSF density about 4×10^{5} cm^{-1} is plotted in Fig. 4-7(b).

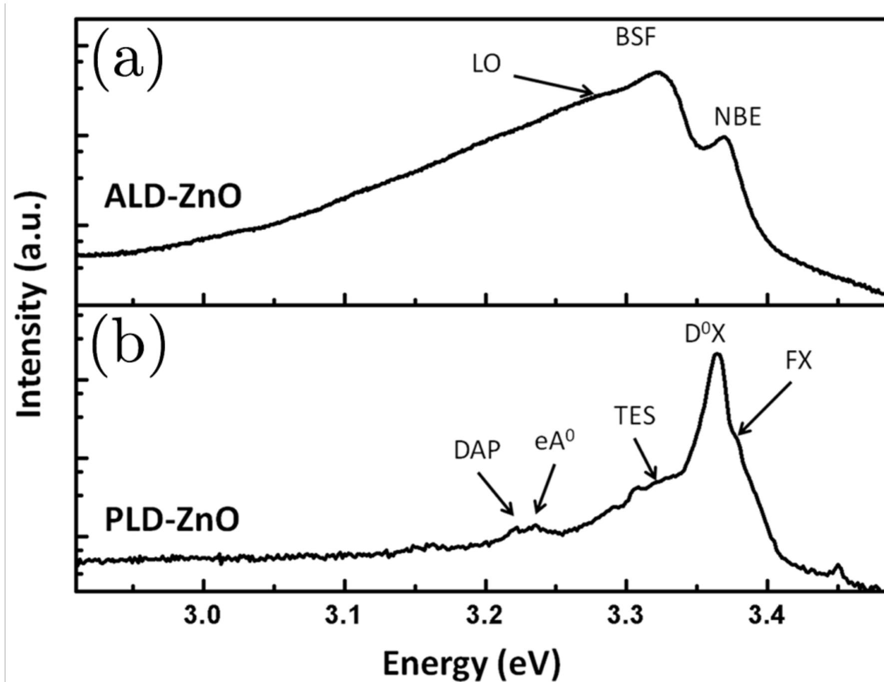

1896

Fig. 4-7 Low temperature PL spectra taken at 10 K of the ZnO films grown by (a) ALD and (b) PLD methods. The PLD grown ZnO with 200 nm thickness was deposited on *c*-plane sapphire at growth temperature of 600ºC. The ALD grown ZnO was deposited at 200°C and annealed at 800°C in oxygen for 1.5 hr.

The most intense peak of the PLD-grown sample is the near band edge (NBE) emission originating from D^0X and free-exciton (FX). The other pronounced peaks centered at ~3.330 eV is attributed to the two-electron satellite (TES) and/or the electrons bound by the stacking faults. [37] The two peaks centered at ~3.23 eV were assigned to DAP and free-electron to acceptor (eA^0) emissions, respectively. In contrast, the

spectrum of the ALD grown ZnO shows distinct features. Three peaks, (1) NBE emission at ~3.37 eV, (2) BSF emission at ~3.321 eV, and (3) "LO" emission at 3.28-3.29 eV, were observed. Because the much larger density of BSFs is the dominant difference in structural properties between the ALD- and PLD-grown ZnO films, the observed spectral difference in Fig. 4-7 may be attributed to the high density of BSFs. To verify this argument, we conducted the following studies.

4.4.1 Temperature Dependent Photoluminescence

Figure 4-8(a) displays the PL spectra of ALD-grown ZnO taken at temperatuares between 10 and 280 K. The NBE emission has a rather large line width (FWHM ~ 22 meV) as compared with those of the PLD-grown ZnO films (FWHM ~ 10 meV and typical 9 ~ 15 meV). [12,13] The broad spectra could be caused by defects which reduce the exciton lifetime and thus broaden the FWHM of the exciton transition. [38] Such broadening increases the difficulty to distinguish D^0X from FX emission in the NBE emission. Peak energies of NBE (inculding both D^0X and FX), BSF, and LO emissions are plotted as a function of temperature in Fig. 4-8(b). These peak energies decrease monotonically with increasing temperature that can be fitted by the Varshni's formula, $E(T) = E(0)-aT^2/(T+\Theta_D)$, where E(0) is the energy at T = 0 K, a is a fitting parameter and Θ_D denotes the Debye temperature, which is set to 920 K according to Refs. 23 and 24. The best fit of the NBE emission energy for temperatures above 100 K, depicted by the dashed curve in Fig. 4-8(a), yields E(0) = 3.374 eV and a = 1.4 meV/K, which agree well with the FX emission of wurtizte ZnO. [39-41] The deviation of the experimental data from the fitting curve for temperatures below 100 K is attributed to the contribution of D^0X, which dominates over FX at low temperatures. The weak LO band emission at

3.28~3.29 eV, whose peak position varies complying with the Varshni's formula, is the typical longitudinal optical phonon replicas of the D^0X emission with the phonon energy about 72 meV. The energy of the BSF emission exhibits a different behavior as a function of temperature; it progressively blue shifts from 3.321 to 3.331 eV as the temperature increases from 10 to 88 K and then red shifts with further temperature increase. Fitting the peak energy of the BSF emission above 88 K by the Varshni's formula yields E(0) = 3.34 eV, which gives a blue shift of ~19 meV with respect to the measured 3.321 eV at 10 K. This phenomenon indicates that the BSF emission could be associated with an exciton transition with energy of 3.34 eV and coupled with a local trap with 19 meV trapping energy.

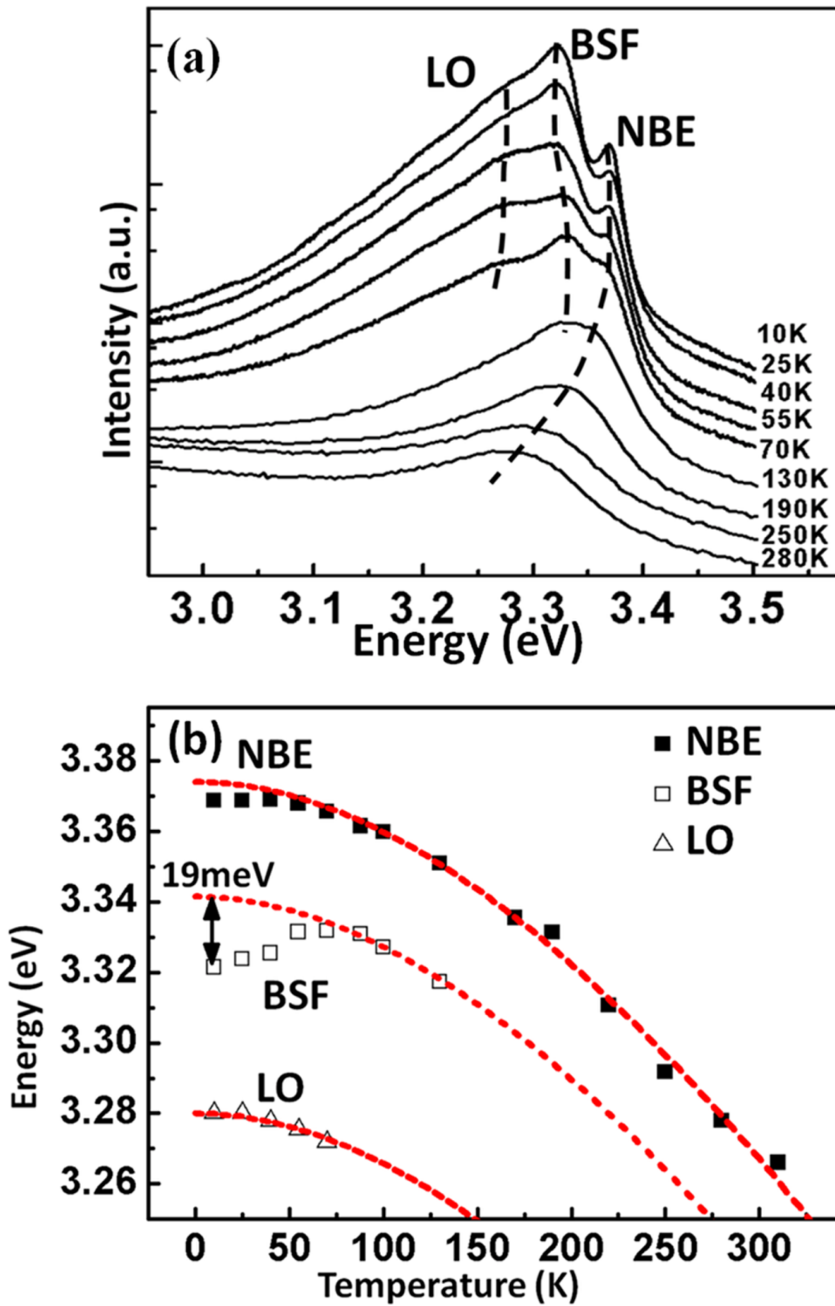

Fig. 4-8 Temperature dependent PL spectra of (a) the ZnO film taken between 10 and 280 K and (b) the energy versus temperature plot of the BSF and NBE emissions. The dash lines depict the fitting results to the Varshni's law.

4.4.2 Power Dependent Photoluminescence

The emission at ~3.321 eV has also been assigned to the DAP transition in ZnO with intentionally doped acceptors, such as N, P, As, and Sb. [42-45] To clarify the nature of the BSF emission in our ZnO epitaxial films, we performed power dependent PL measurements at 10 K; the spectra are plotted in Fig. 4-9.

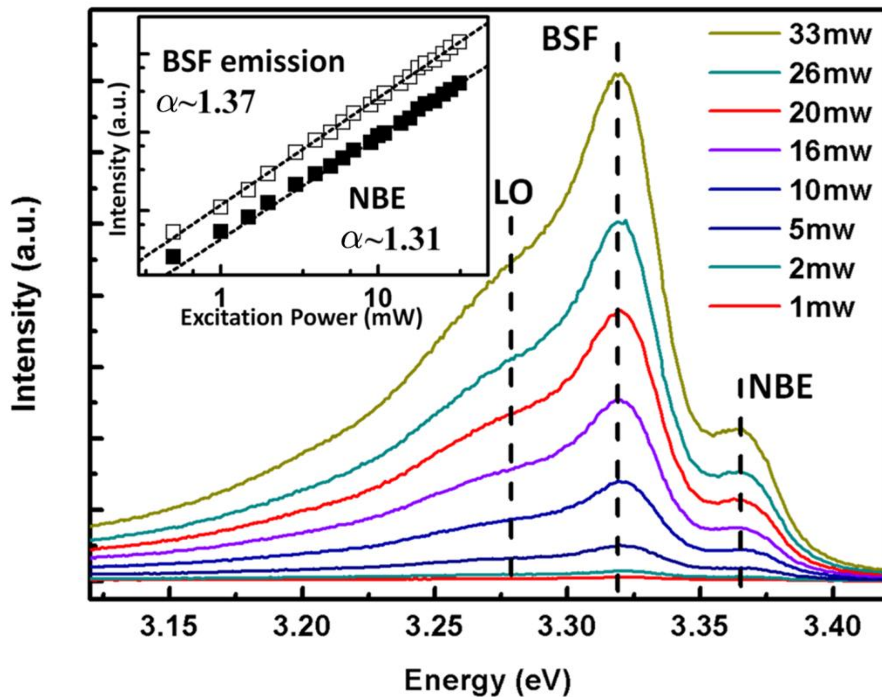

Fig. 4-9 The power dependent PL spectra recorded at 10 K of the ZnO film grown by ALD and annealed at 800°C. The emission intensity versus the excitation power together with the power law fitting results (dash lines) of the BSF and NBE emissions are shown in the inset.

The intensities of the NBE and BSF emissions as a function of excitation power P are depicted in the inset. The peak energy of the BSF emission remains un-shifted even though its intensity rises with increasing excitation power. For both the NBE and BSF

emissions, their curves of emission intensity versus excitation power nicely follow a power law: $I \propto P^{\alpha}$ with the exponents $\alpha = 1.31$ and 1.37, respectively. For a free exciton or bound-exciton emissions, the value of the exponent α should fall in the range of $1 \leqq \alpha \leqq 2$, but for the DAP transitions, α should be less than 1. [46-48] The obtained exponent 1.37 of the BSF emission excludes the mechanism of DAP transition. Together with the absence of peak energy shift with excitaiton power, the results reasonably infer the BSF emission is associated with excitonic transition.

From the point of atomic stacking sequence, a I_1 and I_2 type BSF in wurtzite structure can be considered as a thin layer of zinc blend structure with a thickness of, respectively, 1.5c (0.78 nm) and 2c (1.04 nm), where c is the lattice parameter along the *c*-axis, sandwiched by the wurtzite barriers. According to the *ab initio* calculation, [49] the BSF forms a quantum-well-like region with negative band offsets in the conduction band minimum (CBM) and the valance band maximum (VBM) with respect to those of the wurtzite barriers. This means that the BSF structure would act as a potential well in the conduction band and a potential barrier in the valence band. Therefore, the obtained E(0) of 3.34 eV by fitting the BSF emission could result from the recombination of the confined indirect excitons in BSF (BSF-EX) which were composed of the electrons captured in the potential wells of the BSF and the holes confined at the interface of BSF and wurtzite structure via attractive Coulomb interaction. [50] The 19 meV red shift of the BSF emission from 3.34 eV at temperature about 10 K could be ascribed to the localization effect applied onto the BSF-EX. The localization effect could be attributed to the extrinsic donors (which would bind the BSF-EX) formed by the point defects in or in the vicinity of the quantum well structures. Moreover, the multiple BSFs could be considered as a coupled quantum-wells structure in which the coupling effect of the

electron wave function may be responsible for the localization effect. To consider the reasonableness, the probability density of the electron wave function in single QW (BSF) is estimated about 10% at a penetration length of ~3 nm by using a single QW structure with the dimension and potential heights derived from the *ab initio* calculation. [49] As illustrated in Figs. 4-4 and 4-5, the BSF are distributed in the entire ZnO film with a separation of 2~10 nm along the growth direction (*c*-axis). They could form coupled quantum-wells structure and lead to the localization effect. Similar phenomenon of the localization of excitons have been reported in the BSF in GaN epi-layers [51-54] and also observed in the alloy materials such as InGaN, [55] AlGaN, [56] GaInNAs/GaAs single quantum-well, [57] and InGaN/GaN multiple quantum-wells. [58]

4.5 Conclusion

The structural characteristics of the ALD grown ZnO epitaixal films on *c*-plane sapphire together with the influence of thermal annealing were thoroughly studied. The ZnO films are *c*-plane oriented. The *d*-spacing along the growth direction of the as-deposited ZnO layer is 0.24% larger than the bulk value and progressively decreases and approaches the bulk value with increasing annealing temperature. The in-plane epitaxial relationship of $\{10\bar{1}0\}_{ZnO} \parallel \{10\bar{1}0\}_{Al_2O_3}$ is confirmed from the ϕ-scan data of ZnO $\{10\bar{1}1\}$ and sapphire $\{11\bar{2}6\}$ reflections. This orientation is the same as that of ZnO grown on *c*-plane sapphire at low temperatures by PLD method. [27] After annealing at high temperatures, the crystalline quality exhibits drastic improvement. The diffraction contrast analysis of the cross-section TEM images reveals that intrinsic basal plane stacking faults are the dominant structural defects of the annealed ZnO layers, different

from the PLD grown ZnO layers where threading dislocations are the predominant defects. The diversity in the dominant type of structural defects was attributed to the fundamental difference in the growth mechanisms of the two methods.

High density (~1.0 × 10^6 cm^{-1}) of BSF is identified to be the dominant structure defect in the annealed ZnO epitaxial films grown by ALD on *c*-plane sapphire as verified by TEM and XRD measurements. Each BSF in ZnO is composed of a thin layer of zinc blend structure sandwiched by the wurtzite barriers and forms a type-II quantum-well. The dominant emission centered at ~3.321 eV in PL spectra is ascribed to the transition associated with the BSF bounded indirect excitons (~3.34 eV) which could be trapped by the local defects and/or the potential induced bundled BSF quantum wells at low temperatures.

References

[1] Tsukazaki, A.; Ohtomo, A.; Onuma, T.; Ohtani, M.; Makino, T.; Sumiya, M.; Ohtani, K.; Chichibu, S. F.; Fuke, S.; Segawa, Y.; Ohno, H.; Koinuma, H.; Kawasaki, M., Nat. Mater. 2005, 4, 42.

[2] Lim, J. H.; Kang, C. K.; Kim, K. K.; Park, I. K.; Hwang, D. K.; Park, S. J., Adv. Mater. 2006, 18, 2720.

[3] Smith, A., Thin Solid Films 2000, 376, 47-55.

[4] Hao, X. T.; Tan, L. W.; Ong, K. S.; Zhu, F. R., J. Cryst. Growth 2006, 287, 44.

[5] Shukla, R. K.; Srivastava, A.; Srivastava, A.; Dubey, K. C., J. Cryst. Growth 2006, 294, 427.

[6] Jo, J.; Seo, O.; Choi, H.; Lee, B., Appl. Phys. Express 2008, 1, 041202.

[7] Tang, I. T.; Wang, Y. C.; Hwang, W. C.; Hwang, C. C.; Wu, N. C.; Houng, M. P.; Wang, Y. H., J. Cryst. Growth 2003, 252, 190.

[8] Tena-Zaera, R.; Katty, A.; Bastide, S.; Levy-Clement, C., Chem. Mater. 2007, 19, 1626.

[9] Platzer-Björkman, C.; Törndahl, I.; Hultqvist, A.; Kessler, J.; Edoff, M., Thin Solid Films 2007, 515, 6024.

[10] Zhang, B. P.; Wakatsuki, K.; Binh, N. T.; Usami, N.; Segawa, Y., Thin Solid Films 2004, 449, 12.

[11] Ohkubo, I.; Matsumoto, Y.; Ohtomo, A.; Ohnishi, T.; Tsukazaki, A.; Lippmaa, M.; Koinuma, H.; Kawasaki, M., Appl. Surf. Sci. 2000, 159, 514.

[12] Liu, W. R.; Hsieh, W. F.; Hsu, C. H.; Liang, K. S.; Chien, F. S. S., J. Appl. Crystallogr. 2007, 40, 924.

[13] Liu, W. R.; Li, Y. H.; Hsieh, W. F.; Hsu, C. H., Lee, W. C.; Lee, Y. J.; Hong, M.; Kwo, J., Cryst. Growth Des. 2009, 9, 239.

[14] Lin, C. W.; Ke, D. J.; Chao, Y. C.; Chang, L.; Liang, M. H.; Ho, Y. T., J. Cryst. Growth 2007, 298, 472.

[15] Kowalik, I. A.; Guziewicz, E.; Kopalko, K.; Yatsunenko, S.; Wójcik-Głodowska, A.; Godlewski, M.; Dłużewski, P.; Łusakowska, E.; Paszkowicz, W., J. Cryst. Growth 2009, 311, 1096.

[16] Pung, S. Y.; Choy, K. L.; Hou, X.; Shan, C., Nanotechnol 2008, 19, 435609.

[17] Lin, P. Y.; Gong, J. R.; Li, P. C.; Lin, T. Y.; Lyu, D. Y.; Lin, D. Y.; Lin H. J.; Li, T. C.; Chang, K. J.; Lin, W. J., J. Cryst. Growth 2008, 310, 3024.

[18] Lim, J.; Lee, C., Thin Solid Films 2007, 515, 3335.

[19] Wójcik, A.; Godlewski, M.; Guziewicz, E.; Minikayev, R.; Paszkowicz, W., J. Cryst.

Growth 2008, 310, 284.

[20] Alessandri, I.; Zucca, M.; Ferroni, M.; Bontempi, E.; Depero, L. E., Cryst. Growth Des. 2009, 9, 1258.

[21] King, D. M.; Li, J.; Liang, X.; Johnson, S. I.; Channel, M. M.; Weimer, A. W., Cryst. Growth Des. 2009, 9, 2828.

[22] Puurunen, R. L., J. Appl. Phys. 2005, 97, 121301.

[23] Duniop, L.; Kursumovic, A.; MacManus-Driscoll, J. L.; Appl. Phys. Lett. 2008, 93, 172111.

[24] Koyama, T.; Chichibu, S. F., J. Appl. Phys. 2004, 95, 7856.

[25] Wang, X. Q.; Iwaki, H.; Murakami, M.; Du, X. L.; Ishitani, Y.; Yoshikawa, A., Jpn. J. Appl. Phys. 2003, 42, L99.

[26] Chen, Y. F.; Bagnall, D. M.; Koh, H. J.; Park, K. T.; Hiraga, K.; Zhu, Z. Q.; Yao, T., J. Appl. Phys. 1998, 84, 3912.

[27] Ohkubo, I.; Ohtomo, A.; Ohnishi, T.; Mastumoto, Y.; Koinuma, H.; Kawasaki, M., Surf. Sci. 1999, 443, L1043.

[28] Vispute, R. D.; Talyansky, V.; Trajanovic, Z.; Choopun, S.; Downes, M.; Sharma, R. P.; Venkatesan, T.; Woods, M. C.; Lareau, R. T.; Jones, K. A.; Iliadis, A. A., Appl. Phys. Lett. 1997, 70, 2735.

[29] Vinnichenko, M.; Shevchenko, N.; Rogozin, A.; Grötzschel, R.; Mücklich, A.; Kolitsch, A.; Möller, W., J. Appl. Phys. 2007, 102, 113505.

[30] Abouzaid, A.; Ruterana, P.; Liu, C.; Morkoc, H., Superlatt. Microstruct. 2007, 42, 110.

[31] D. Kohla, M. H., and G. Heilanda, Surf. Sci. 1973, 41, 403.

[32] Hass, K. C.; Schneider, W. F.; Curioni, A.; Andreoni, W., Science 1998, 282, 882.

[33] Stampfl, C.; Van de Walle, C. G., Phys. Rev. B 1998, 57, R15052.

[34] Gerthsen, D.; Litvinov, D.; Gruber, T.; Kirchner, C.; Waag, A., Appl. Phys. Lett. 2002, 81, 3972.

[35] Vennegues, P.; Chauveau, J. M.; Korytov, M.; Deparis, C.; Zuniga-Perez, J.; Morhain, C., J. Appl. Phys. 2008, 103, 083525.

[36] Kawasaki, M.; Ohtomo, A.; Ohkubo, I.; Koinuma, H.; Tang, Z. K.; Yu, P.; Wong, G. K. L.; Zhang, B. P.; Segawa, Y., Mater. Sci. Eng. B 1998, 56, 239.

[37] M. Schirra, R. Schneider, A. Reiser, G. M. Prinz, M. Feneberg, J. Biskupek, U. Kaiser, C. E. Krill, K. Thonke, R. Sauer, Phys. Rev. B. 77, 125215 (2008).

[38] T. Koida, S. F. Chichibu, A. Uedono, A. Tsukazaki, M. Kawasaki, T. Sota, Y. Segawa, H. Koinuma, Appl. Phys. Lett. 82, 532 (2003).

[39] V. A. Fonoberov, K. A. Alim, A. A. Balandin, F. Xiu, J. Liu, Phys. Rev. B. 73, 165317 (2006).

[40] D. W. Hamby, D. A. Lucca, M. J. Klopfstein, G. Cantwell, J. Appl. Phys. 93, 3214 (2003).

[41] D. C. Look, D. C. Reynolds, J. R. Sizelove, R. L. Jones, C. W. Litton, G. Cantwell, W. C. Harsch, Solid State Commun. 105, 399 (1998).

[42] Y. R. Ryu, T. S. Lee, H. W. White, Appl. Phys. Lett. 83, 87 (2003).

[43] D. C. Look, D. C. Reynolds, C. W. Litton, R. L. Jones, D. B. Eason, G. Cantwell, Appl. Phys. Lett. 81, 1830 (2002).

[44] F. X. Xiu, Z. Yang, L. J. Mandalapu, D. T. Zhao, J. L. Liu, Appl. Phys. Lett. 87, 252102 (2005).

[45] F. X. Xiu, Z. Yang, L. J. Mandalapu, J. L. Liu, Appl. Phys. Lett. 88, 152116 (2006).

[46] Y. W. Zhang, X. M. Li, W. D. Yu, C. Yang, X. Cao, X. D. Gao, J. F. Kong, W. Z. Shen,

J. L. Zhao, X. W. Sun, J. Phys. D: Appl. Phys. 42, 075410 (2009).

[47] D. Stichtenoth, J. Dürr, C. Ronning, L. Wischmeier, T. Voss, J. Appl. Phys. 103, 083513 (2008).

[48] T. Schmidt, K. Lischka, W. Zulehner, Phys. Rev. B. 45, 8989 (1992).

[49] Y. Yan, G. M. Dalpian, M. M. Al-Jassim, S.-H. Wei, Phys. Rev. B. 70, 193206 (2004).

[50] Y. T. Rebane, Y. G. Shreter, M. Albrecht, Phys. Status Solidi A 164, 141 (1997).

[51] W. Rieger, R. Dimitrov, D. Brunner, E. Rohrer, O. Ambacher, M. Stutzmann, Phys. Rev. B. 54, 17596 (1996).

[52] P. Corfdir, P. Lefebvre, J. Levrat, A. Dussaigne, J.-D. Ganière, D. Martin, J. Ristić, T. Zhu, N. Grandjean, B. Deveaud-Plédran, J. Appl. Phys. 105, 043102 (2009).

[53] Y. J. Sun, O. Brandt, U. Jahn, T. Y. Liu, A. Trampert, S. Cronenberg, S. Dhar, K. H. Ploog, J. Appl. Phys. 92, 5714 (2002).

[54] P. P. Paskov, R. Schifano, B. Monemar, T. Paskova, S. Figge, D. Hommel, J. Appl. Phys. 98, 093519 (2005).

[55] Q. Li, S. J. Xu, W. C. Cheng, M. H. Xie, S. Y. Tong, C. M. Che, H. Yang, Appl. Phys. Lett. 79, 1810 (2001).

[56] S. J. Chung, M. Senthil Kumar, H. J. Lee, E.-K. Suh, J. Appl. Phys. 95, 3565 (2004).

[57] L. Grenouillet, C. Bru-Chevallier, G. Guillot, P. Gilet, P. Duvaut, C. Vannuffel, A. Million, A. Chenevas-Paule, Appl. Phys. Lett. 76, 2241 (2000).

[58] K. S. Ramaiah, Y. K. Su, S. J. Chang, B. Kerr, H. P. Liu, I. G. Chen, Appl. Phys. Lett. 84, 3307 (2004).

[59] Y. Chen, D. M. Bagnall, H.-J. Koh, K.-T. Park, K. Hiraga, Z. Zhu, and T. Yao, J. Appl. Phys. 84, 3912 (1998)

1896

[60] C.-W. Lin, D.-J. Ke, Y.-C. Chao, L. Chang, M.-H. Liang, and Y.-T. Ho, J. Cryst. Growth 298, 472 (2007)

Chapter 5 *m*-plane ZnO grown on *m*-plane Sapphire by ALD

C-plane sapphire is widely employed as the substrate to grow ZnO epitaxial films with good quality and reasonable cost. Nonetheless, strong spontaneous polarization and piezoelectric polarization at the interfaces of ZnO based heterostructures induce a large internal electric field along the *c*-axis that results in the quantum-confined Stark effect leading to a spectral red-shift and a dramatic decrease in the luminous efficiency. In order to avoid this problem, many efforts has been put to enhance the luminous efficiency by taking advantage of the non-polar *m*-plane orientated ZnO layers through several growth methods such as molecular beam epitaxy (MBE), [3-6] metal organic chemical vapor deposition (MOCVD), [7,8] and pulsed laser deposition (PLD) [9,10]. Unfortunately, to fabricate *m*-plane ZnO epi-films with high structural perfection and smooth surface morphology is still very difficult. One common problem is the coexistence of minor domains with $(10\bar{1}3)$, [3,6,7] (0002), [6] or $(11\bar{2}2)$ [6] orientations. In particular, the $(10\bar{1}3)$ oriented domains are often observed and difficult to eliminate. Moreover, surface morphologies of the deposited *m*-plane ZnO films on foreign substrates often exhibit stripe features elongated along a direction either parallel or normal to the ZnO *c*-axis depending on the growth conditions. [7,8,11] These features strongly hamper the application of ZnO-based heterostructures. Different from other growth methods, the growth mechanism of atomic layer deposition (ALD) relies on the sequential self-terminated chemical reactions and leads to layer-by-layer growth with the advantages of accurate thickness control, high uniformity, high reproducibility, high

covering ratio, and low growth temperature. The epitaxial *m*-plane ZnO films with the absence of minor domains could be grown on *m*-plane sapphire, [12] however, the crystal quality of epitaxial films needs to be further improved and the correlation between structural and optical properties should be explored in depth.

In this chapter, ALD method was employed to grow *m*-plane oriented ZnO epitaxial films with single crystallographic orientation and smooth surface morphology. By taking advantage of thermal annealing treatment we further improved the crystallinity and morphology of these *m*-plane ZnO layers.

5.1 XRD measurements

5.1.1 2θ/θ scan and ω-rocking curve

To examine the structure characteristics of the ZnO layers, we performed XRD measurements on the as-deposited and the 800°C annealed samples. Besides the intense sapphire $(30\bar{3}0)$ Bragg reflection, only the ZnO $(10\bar{1}0)$, $(20\bar{2}0)$, and $(30\bar{3}0)$ reflections are observed in the radial scans along surface normal of both samples, as illustrated in Fig. 5-1(a). The absence of other diffraction peaks manifests the ZnO films are of single crystallographic $(10\bar{1}0)$ orientation, i.e., *m*-plane orientation. Upon annealing, the peak widths of all the ZnO reflections significantly decrease. For example, the full width at half maximum (FWHM) of the ZnO $(10\bar{1}0)_{ZnO}$ reflection decreases from 9.38×10^{-3} to 5.36×10^{-3} Å^{-1}, manifesting the increase of the structural coherent length and the improvement of crystalline quality of the ZnO layers.

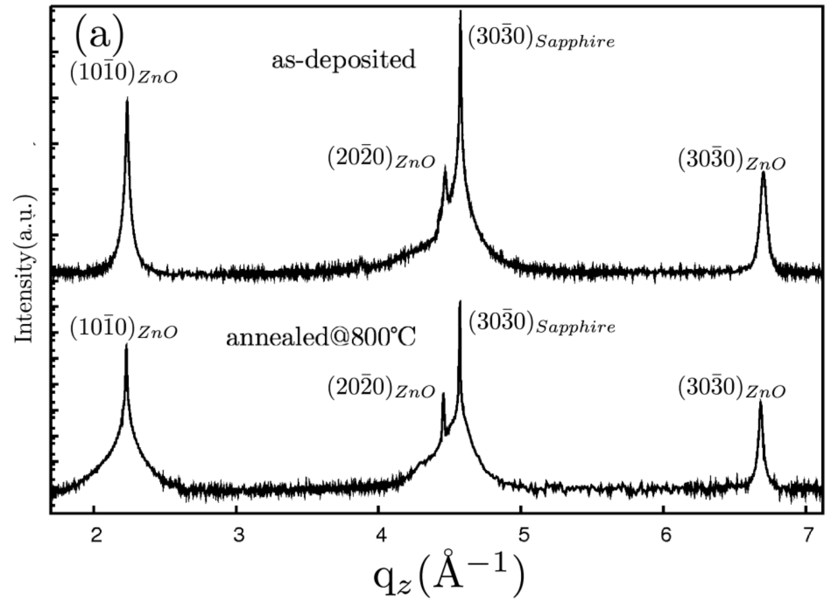

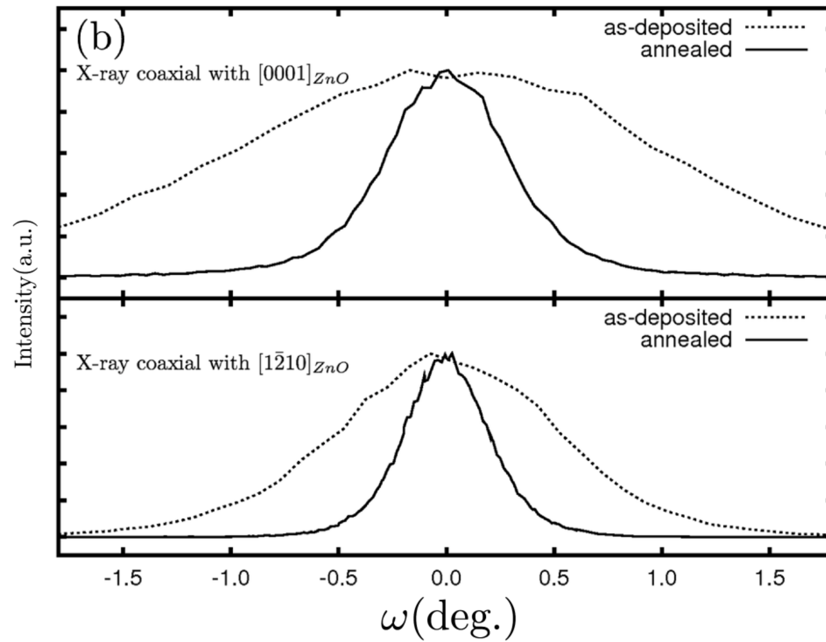

Fig. 5-1 XRD radial scans along the surface normal (θ-2θ scan) of (a) an as-deposited ZnO film and a 800ºC annealed sample, and (b) the ω rocking curves across the $(10\bar{1}0)_{ZnO}$ specular reflection with impinging X-rays aligned with (top panel) ZnO c-axis and (bottom panel) $[11\bar{2}0]_{ZnO}$ a-axis, respectively. The abscissa q_z denotes momentum transfer along the surface normal.

Figure 5-1(b) displays the rocking curves of the $(10\bar{1}0)_{ZnO}$ specular reflection of the samples with the directions of incident X-rays along two orthorgonal directions, either aligned or perpendicular to the ZnO *c*-axis. The dotted and solid curves were, respectively, taken before and after thermal treatment. Along both directions, the peak widths show drastic reduction after thermal annealing revealing the decrease of the tilt angle of the ZnO layer. Moreover, the FWHM measured with X-ray along the $[0001]_{ZnO}$ *c*-axis is always much larger than that along the $[1\bar{2}10]_{ZnO}$ *a*-axis that are 2.489° *vs.* 1.219° before annealing and 0.679° *vs.* 0.464° after thermal annealing. This observation reveals the higher structural perfection of the obtained *m*-plane ZnO film along the *a*-axis as compared with that along the *c*-axis. As a comparison, , the XRD peak FWHM along the $[0001]_{ZnO}$ and $[1\bar{2}10]_{ZnO}$ directions of the samples grown by RF-sputtering are 0.445° and 0.392° [23] and of those grown by MBE are 1.0° and 0.5°, respectively. [6]

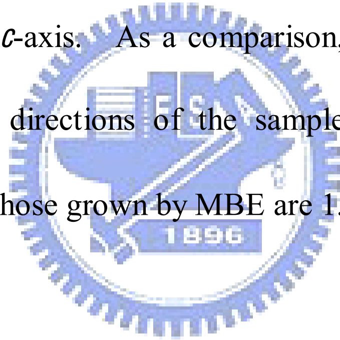

5.1.2 Azimuthal cone scans

To examine the epitaxial relationship between the ZnO layer and the sapphire substrate, we performed azimuthal cone scans (ϕ-scan) across the off-normal $\{10\bar{1}2\}_{ZnO}$ and $\{03\bar{3}0\}_{Al_2O_3}$ reflections, as illustrated in Fig. 5-2. All the ϕ-scans show a 2-fold symmetry and the angular positions of $\{10\bar{1}\pm2\}_{ZnO}$ reflections coincide with that of the $(03\bar{3}0)_{Al_2O_3}$ and $(3\bar{3}00)_{Al_2O_3}$, which yield the in-plane relationship of $[0001]_{ZnO} \parallel [1\bar{2}10]_{Al_2O_3}$ with an uncertainty of the polarity of the ZnO layer.

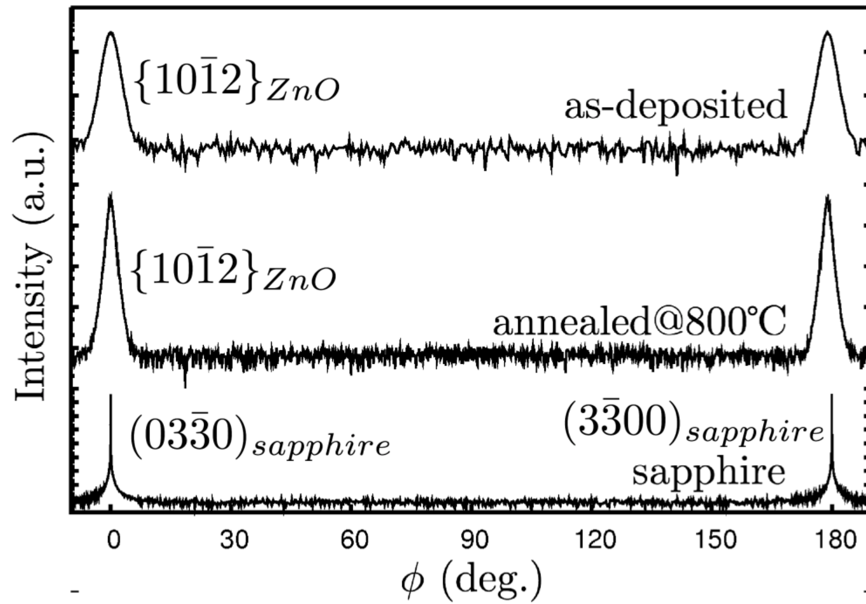

Fig. 5-2 The azimuthal reflection scan across the $\{10\bar{1}2\}_{ZnO}$ and $\{30\bar{3}0\}_{Al_2O_3}$ planes. The in-plane relationship of the ZnO film and the sapphire substrate has determined as $\{0002\}_{ZnO} \parallel \{11\bar{2}0\}_{Al_2O_3}$ and $\{0002\}_{Al_2O_3} \parallel \{11\bar{2}0\}_{ZnO}$. The thermal annealing treatment improved the edge and screw dislocations of the as-deposited ZnO film as the FWHM decreasing from 1.39° to 0.68°.

Under this configuration, the lattice mismatches between ZnO and the underneath sapphire are 0.06% and 9.4% along ZnO *a*- and *c*-axes. Similar reduction in the FWHM of the $\{10\bar{1}2\}_{ZnO}$ peaks from 1.39º to 0.68º upon annealing was also noticed that manifests the decrease of twist angle. Such a decrease in both tilt and twist angles is often attributed to the reduction of both the edge and screw dislocation densities. [13] From the angular positions of diffraction peaks, we deduced the inter-planar spacings along three orthogonal axes, i.e., the surface normal *m*-axis and the two lateral directions,

a-axis and *c*-axis. The as-deposited ZnO film has spacings 5.630, 3.253, and 5.214 Å along the *m*-, *a*- and *c*-axes, respectively. After thermal annealing, the variation of the inter-planar spacings are all within 0.2% or less, indicating the deposited layer is nearly strain free. The FWHM of $\{10\bar{1}2\}_{ZnO}$ peaks is about 0.9652º for the RF-sputtering grown m-ZnO. [23]

5.1.3 X-ray Reflectivity

The data of X-ray reflectivity (XRR) measurements of the as-deposited ZnO layer and the samples annealed at 400, 600, and 800 ºC are shown in Fig. 5-3. The critical angles do not reveal obvious change after thermal annealing represents the weak influence of the thermal annealing on the electron density, the material density. From the periodicity values (ΔQ) of the interference fringes the thickness of the ZnO layers were estimated about 133 nm, which are close to the thickness of 200 unit cells along the $[11\bar{2}0]_{ZnO}$ direction as 112.5 nm. Besides, by fitting the refletivity curve, we estimated the R_{rms} values of the film surface are 1.342, 1.602, 0.967, and 0.703 nm for the samples of as-deposited, annealing at 400, 600, and 800 ^{o}C, respectively. The flatness of the ZnO layer was improved by annealing action, except for annealing at 400 ºC. Besides, the estimated density values are ~5.69 g/cm^3 of as-deposited film and ~5.85 g/cm^3 for samples annealed at temperature of 600 and 800 ºC. Such observation implies that there could be organic residuals produced in the depositing procedure, and these organic residuals could be eliminated by annealing at 400 ºC accompanied by the surface morphology degradation. Annealing at temperatures higher than 600 ^{o}C could lead to recrystallization and thus increase the film density, decrease the surface roughness, and

improve the crystalline quality. On the other hand, the estimated R_{rms} values of the interface between the ZnO film and sapphire substrate are ~0.215 nm, which does not show obvious variation as annealing temperature increases.

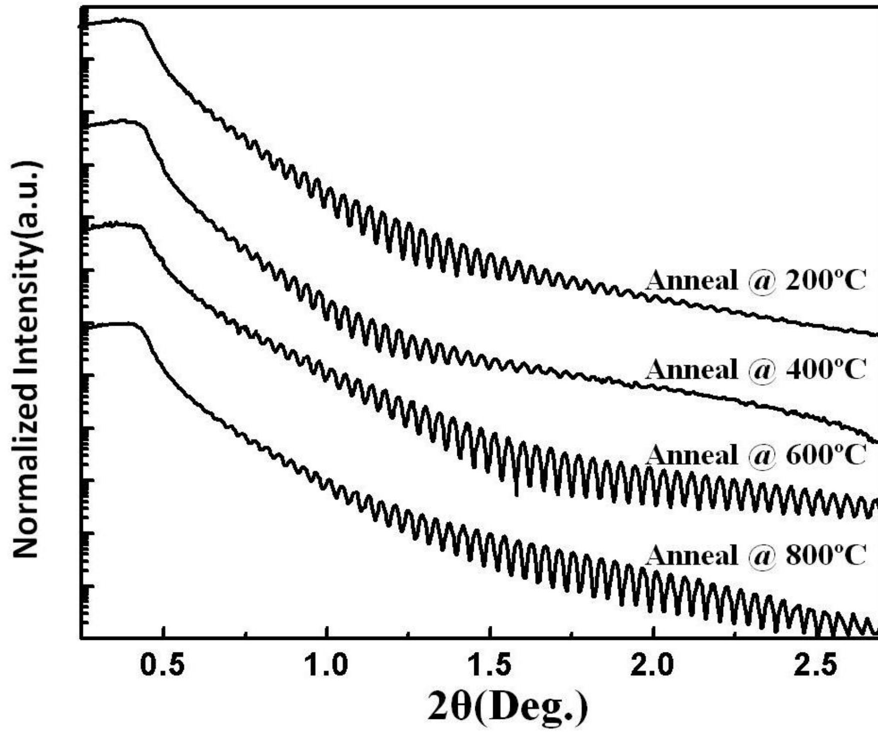

Fig. 5-3 X-ray reflectivity of the as-deposited ZnO film and that after annealed at 400, 600, and 800 ºC.

5.2 TEM

5.2.1 Cross Section Images with Zone Axis $[\bar{1}2\bar{1}0]_{ZnO}$

Figure 5-4(a) shows the cross sectional TEM images taken along the $[\bar{1}2\bar{1}0]_{ZnO}$ zone axis of the 800°C annealed sample. The corresponding selected area electron diffraction (SAED) patterns are shown in Fig. 5-4(b). The coexistence of the rectangular and hexagonal lattices associated, respectively, with ZnO and sapphire confirms that the

epitaxial relationship is $(10\bar{1}0) < 0001 >_{ZnO} \parallel (10\bar{1}0) < \bar{1}2\bar{1}0 >_{Al_2O_3}$ in agreement with the XRD data. Several contrast lines propagating along the growth direction (marked by triangles) were observed in the TEM image. They are likely due to basal plane stacking faults (BSFs). To further characterize the nature of the contrast lines we performed diffraction contrast analysis on the annealed sample. The contrast lines are clearly visible in the bright field image recorded with diffraction vectors g equal to $(10\bar{1}0)$ in Fig. 5-4(c), but are out of contrast for g equal to (0002) in Fig. 5-4(d), where the insets show the corresponding diffraction peaks which were adopted to form the images. According to the extinction rules, the stacking faults are out of contrast when g·R is equal to an integer.

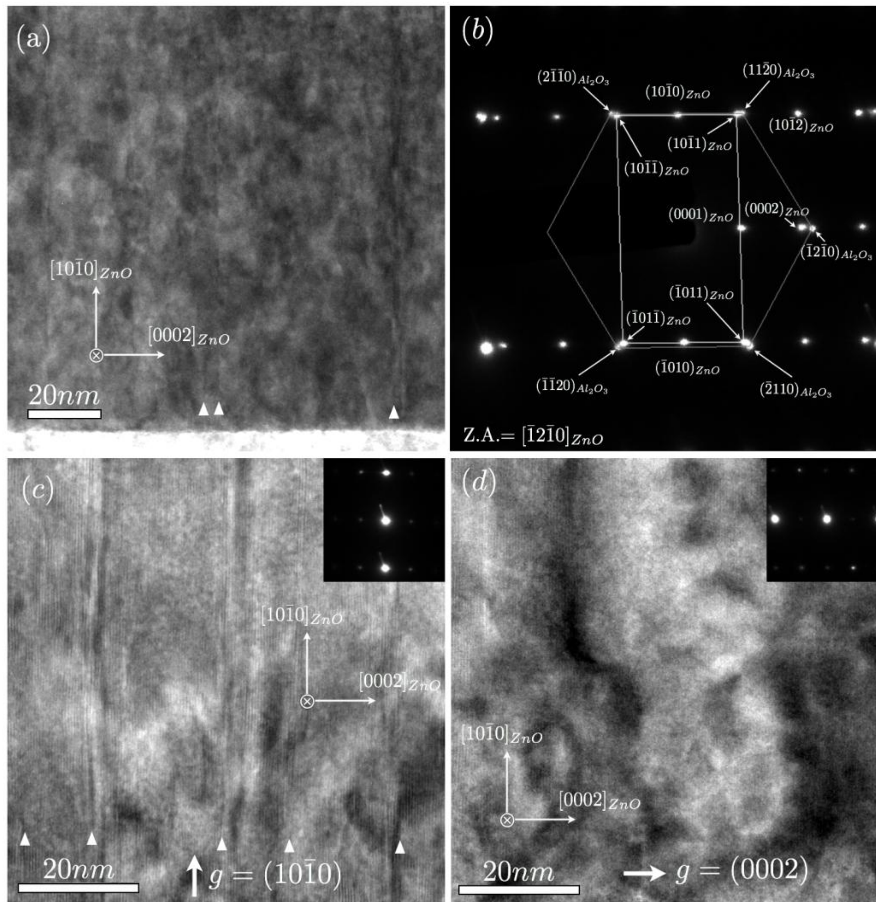

Fig. 5-4 The cross sectional TEM image (a) and the selected area electron diffraction (SAED) pattern (b) taken along the $[\bar{1}2\bar{1}0]_{ZnO}$ zone axis, and the bright field images recorded with diffraction vector g equal to $(10\bar{1}0)_{ZnO}$ (c) and $(0002)_{ZnO}$ (d), respectively. The contrast lines in the images marked by the triangles are identified to be the intrinsic type basal plane stacking faults.

The displacement vectors R associated with three types of BSFs, I_1, I_2, and E are $\frac{1}{6}(2\bar{2}03)$, $\frac{1}{3}(1\bar{1}00)$, and $\frac{1}{2}(0001)$, respectively. The observed variation of g dependent contrast indicates the BSFs in the *m*-plane ZnO film belong to the intrinsic type I_1 and/or

I_2. However, we don't have sufficient information to further distinguish between these two.

5.2.2 Cross Section Images with Zone Axis $[0001]_{ZnO}$

The cross-sectional TEM image taken along the $[0001]_{ZnO}$ zone axis, perpendicular to that of Fig. 5-4, is illustrated in Fig. 5-5(a), where no contrast lines were identified. The associated SAED pattern in Fig. 5-5(b) exhibits the hexagonal ZnO and the sapphire diffraction patterns. The bright field images with g equal to $(10\bar{1}0)_{ZnO}$ and $(\bar{1}2\bar{1}0)_{ZnO}$ are illustrated in Fig. 5-5(c) and 5.5(d), respectively.

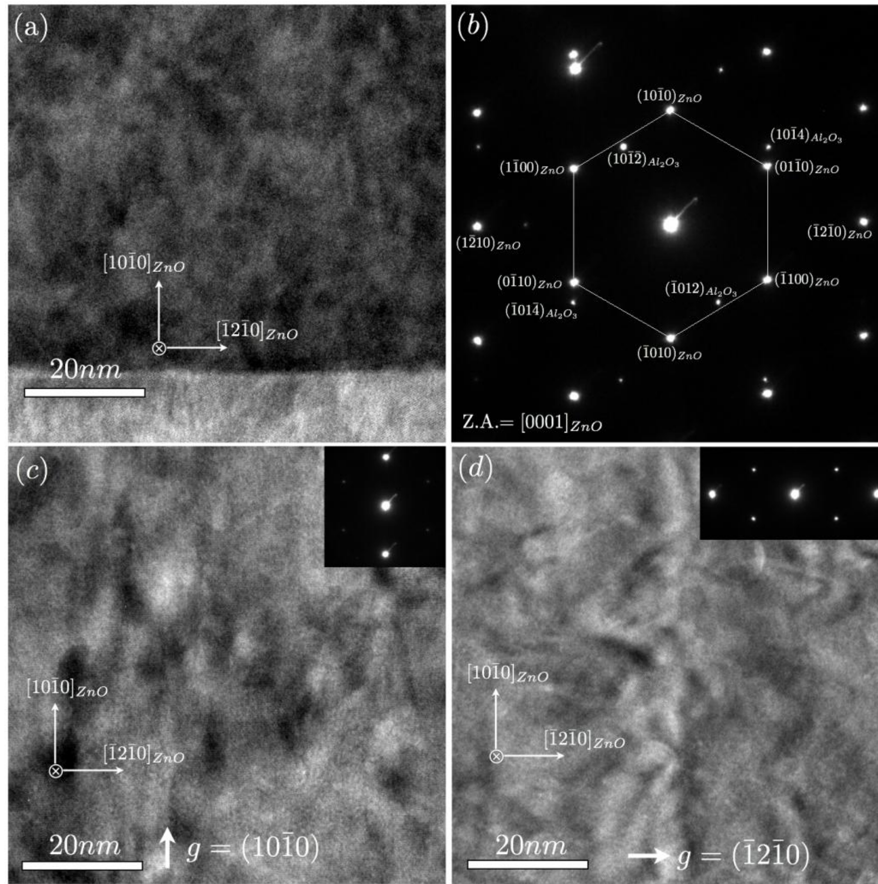

Fig. 5-5 The cross sectional TEM image (a) and the selected area electron diffraction (SAED) pattern (b) taken along the zone axis of $[0001]_{ZnO}$, and the bright field images taken with diffraction vector g equal to $(10\bar{1}0)_{ZnO}$ (c) and $(\bar{1}2\bar{1}0)_{ZnO}$ (d), respectively.

Again, no contrast lines were observed in these images. The absence of the contrast lines in this zone axis supports that the contrast lines observed in Fig. 5-4 are originated from the BSFs, which lie on the planes perpendicular to this zone axis, and rules out the possibilities of threading dislocations. From these TEM images, we found BSF is the

dominant structural defect and its density is estimated to be about ~ 1×10^6 cm^{-1}, which is very close to the value of the high quality *m*-plane ZnO film grown on the lattice-matched $LaAlO_3$ substrate at high growth temperature by PLD. [10]

5.2.3 Fourier Filtered Images Analysis

To observe the lattice matching across the interface, we took high-resolution TEM images near the ZnO/sapphire interface. Shown in Fig. 5-6(a) is the TEM cross sectional image recorded with the $[\bar{1}2\bar{1}0]_{ZnO}$ zone axis. The corresponding Fourier filtered image using $(\bar{1}2\bar{1}0)_{Al_2O_3}$ and $(0002)_{ZnO}$ reflections is shown in the inset, where widely separated misfit dislocations, as represented by additional $(\bar{1}2\bar{1}0)_{Al_2O_3}$ half planes (marked by the triangle) inserted into the sapphire lattice, scatter along the interface as a result of the 9.4 % lattice mismatch across the interface.

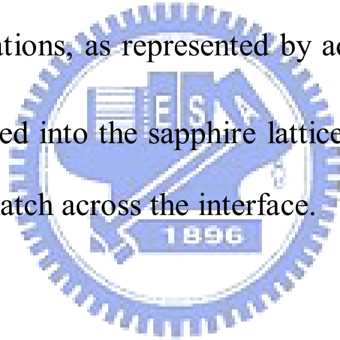

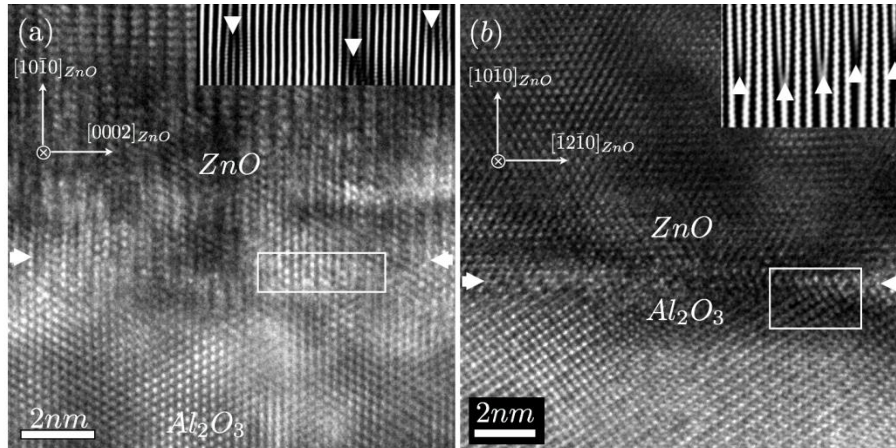

Fig. 5-6 The high resolution images of the interface with the zone axis of (a) $[\bar{1}2\bar{1}0]_{ZnO}$ and (b) $[0001]_{ZnO}$, and the inset in (a) is the corresponding Fourier filtered image using the $(\bar{1}2\bar{1}0)_{Al_2O_3}$ and $(0002)_{ZnO}$ spots; and the Fourier filtered image in (b) is formed by using the $(0006)_{Al_2O_3}$ and $(\bar{1}2\bar{1}0)_{ZnO}$ reflections.

1896

In contrast, Fig. 5-6(b) is the image taken along the $[0002]_{ZnO}$ zone axis, where regularly arranged atomic rows are well resolved. Its Fourier filtered image formed by using $(0006)_{Al_2O_3}$ and $(\bar{1}2\bar{1}0)_{ZnO}$ spots, displayed in the inset, reveals four $(\bar{1}2\bar{1}0)_{ZnO}$ planes match three $(0006)_{Al_2O_3}$ planes along $[\bar{1}2\bar{1}0]_{ZnO}$ direction and each extra $(\bar{1}2\bar{1}0)_{ZnO}$ plane corresponds to a misfit dislocation (marked by the triangles). The nearly evenly spaced misfit dislocations reveal the domain matching epitaxial (DME) [14] at the interface along $[\bar{1}2\bar{1}0]_{ZnO}$ with effective mismatch about 0.06%, which agrees with the reported observation in the sample grown by other method. [5]

5.3 AFM

The surface morphology of the samples before and after annealing measured by atomic force microscopy (AFM) are illustrated in Figs. 5-7(a) and (b), respectively.

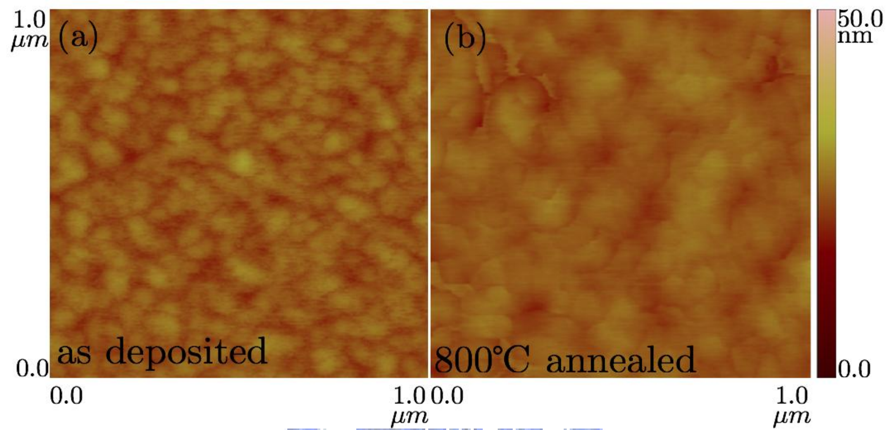

Fig. 5-7 AFM images of the as-deposited (a) and annealed (b) *m*-ZnO films with surface roughness (R_{rms}) of 1.62 and 1.38 nm, respectively.

The surface morphologies of the non-polar ZnO films grown by MOCVD and MBE methods usually exhibit stripe features elongated along a direction either parallel or normal to the ZnO *c*-axis depending on the growth conditions and terminated with specific crystal facets in some cases. [6-8,11,15,16] In contrast, the granular features observed in Fig. 5-7 manifest the absence of preferable lateral growth directions of the ZnO layer grown by ALD. [7,8,11] Such a difference could be attributed to the growth nature and the self-limiting growth mechanism of ALD, for which the adatoms would rather attach to surface lattice site than congregate to clusters and result in smoothly and fully covered layers. But the morphology and the growth rate reveal that the growth

mechanism may not be ideal layer-by-layer growth according to which a monolayer of the ALD-growth material is assumed to form per cycle. In the ALD process, the surface morphology and growth rate depend on the chemical reaction condition on the surface that could be influenced by factors such as steric hindrance and growth temperature. [22] Such chemical reaction condition on the surface is very complex and requires further research. Moreover, both surfaces show very small surface roughness. Upon annealing, the increase of surface feature size accompanied by the decrease of the root-mean-square (rms) roughness from 1.62 to 1.38 nm is observed. In light of the annealing induced roughness degradation observed in *c*-plane ZnO grown on *c*-plane sapphire under similar growth conditions [16] and the (000±1) polar surfaces having the highest surface energies, the improvement of surface roughness upon annealing in this work is ascribed to the low surface energy of the $(10\bar{1}0)_{ZnO}$ terminated surface. [15]

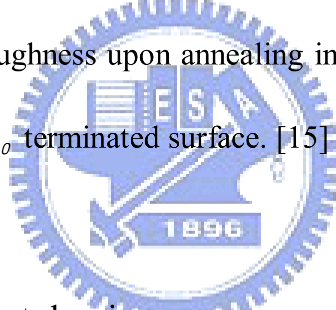

5.4 Photoluminescence

5.4.1 Low-Temperature Photoluminescence

To investigate optical properties of the *m*-plane ZnO and the influence of the annealing effect, we performed time-integrated PL (TI-PL) measurements at 5 K as shown in Fig. 5-8(a). The spectrum of the as-deposited ZnO film shows a broad emission band at energy below 3.35 eV. Upon annealing at 400°C, the emissions below ~3.3 eV are strongly depressed and the broad emission band shrinks to a peak centered at ~3.33 eV (marked as “B band”) with a line width about 12 meV; in the mean while a peak centered at ~3.37 eV with a line width about 6 meV (marked as “NBE”) emerges. The absence of the NBE emission and the presence of the broad emission below 3.3 eV before annealing is likely due to residual organic functional groups which was trapped inside the film and

can be eliminated by annealing. The origin of the NBE band emission is mainly donor bound exciton (D^0X) recombination at low temperature. [17] The B band at 3.325 eV has been observed in ZnO films and identified to be associated with the basal plane stacking faults (BSFs). [18-20] From the results of structure analyses, we found the *m*-plane ZnO films have large density (~10^6 cm^{-1}) of BSFs, much higher than what found in most of the *c*-plane ZnO films. Therefore, it is not surprising that the B emission band is the dominant feature in the low-temperature PL spectra of *m*-plane ZnO films. The small bump located at ~72 meV lower than the B band, as marked by an arrow, is ascribed to the longitudinal optical phonon (LO) replica of the B band. With thermal treatment at elevated temperatures, the intensity ratios of NBE to B band emissions increases from 0.16 to 0.19 and then to 0.76 for annealing temperature of 400, 600, and 800°C, respectively. The increasing intensity ratio implies that the thermal treatment with higher temperatures further eliminates the residual impurities and dislocations.

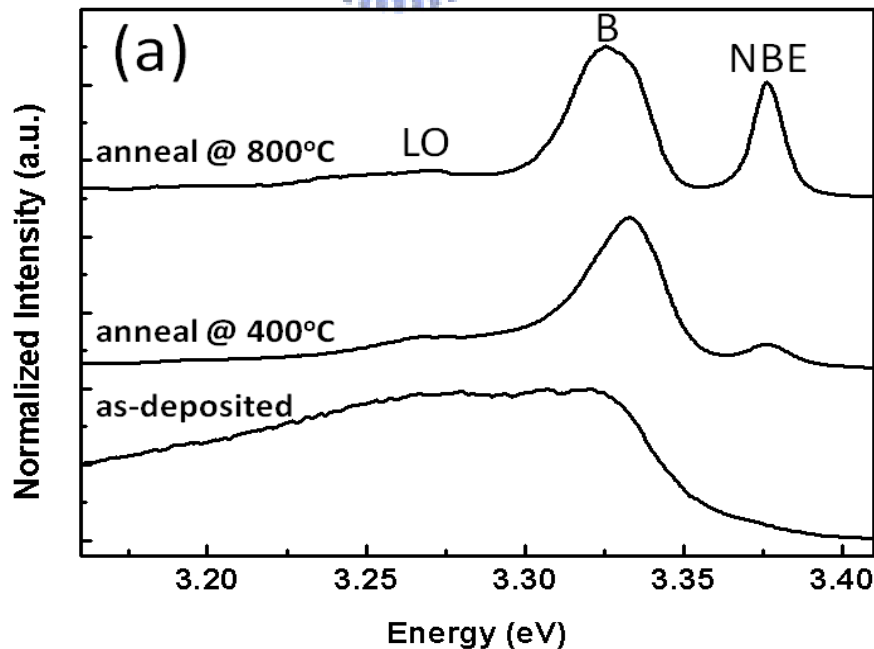

Fig. 5-8 The time integrated photoluminescence at 5 K of the as-deposited sample and sample annealed at 400 and 800°C with the inset of the annealing temperature dependent intensity ratio of NBE band to BSF band.

5.4.2 Time-Resolved Photoluminescence

By analyzing the TR-PL spectra of the 800°C annealed sample recorded at 5 K illustrated in Fig. 5-9, we found that the B band and NBE band decay curves exhibited multi-exponential decay, which implied the complex transition mechanism.

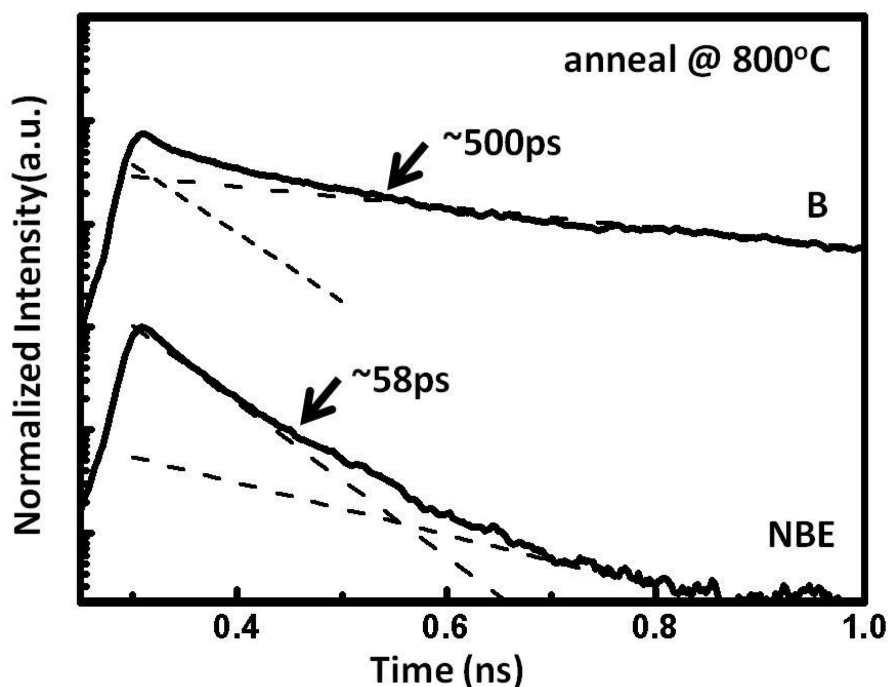

Fig. 5-9 The time resolved photoluminescence at 5 K of the NBE and B band in the sample annealed at 800°C with the dash lines as the fitted bi-exponential decay curves.

Nevertheless, we could fit the decay curves nicely by using the bi-exponential decay model to estimate the decay times. According to the fitting results, we estimated the B band decay times were ~500 ps and ~40 ps with the ~500 ps one dominating. For the NBE band, the decay time were ~58 ps and ~175 ps and the ~58 ps one is dominating. Under such a situation, we take the decay times of the dominating decay curves as the major decay times. The decay time of NBE band is less than the reported lifetime of D^0X transition (~100 ps) [21] that could be ascribed to the large density of BSFs which would frustrate the D^0X transition. By analyzing the TR-PL spectra of the samples annealed at different temperatures (not shown here), we found that the decay time of NBE band increases monotonically from 39, 53 to 58 ps with elevated annealing temperature raised from 400, 600 to 800°C, respectively. The samples annealed at the higher temperature show the longer NBE decay time. The variations of the NBE to B band intensity ratio and the decay time as functions of annealing temperature indicate that the crystalline and optical properties of the as-deposited ZnO film would be strongly and negatively influenced by the residual chemical function group. Thermal treatment effectively eliminates the residual chemical function group by low temperature annealing at 400°C and repairs the defect and dislocations by high annealing temperature, that usually observed in crystalline bulk. However, thermal annealing is not effective in eliminating the BSFs in the ZnO films.

5.5 Conclusion

The ZnO thin films grown on *m*-plane sapphire by ALD are confirmed to be single crystallographic *m*-plane orientated. The epitaxial relationship between the *m*-plane

ZnO film and the *m*-plane sapphire substrate follows $(10\bar{1}0) < 0001 >_{ZnO} \parallel (10\bar{1}0) < \bar{1}2\bar{1}0 >_{Al_2O_3}$ and reveals the DME with the nearly perfect domain matching across the ZnO/sapphire interface along the $[1\bar{2}10]_{ZnO}$ direction. The smooth surface with isotropic granular features manifests the layer-by-layer growth nature of ALD growth. From the PL spectra and the TEM images of the annealed samples, large density (~10^6 cm^{-1}) of intrinsic type BSF are identified as the major defect and could be the origin of the B band emission centered at about 3.325 eV in the PL spectra. From the time resolved photoluminescence, the near-bandedge emission band is identified to be the D^0X transition and its decay time increases with the higher annealing temperatures. It is demonstrated that ALD method is suitable for fabricating high quality *m*-plane ZnO epi-layers on *m*-plane sapphires with high surface flatness. Thermal annealing further improves the crystalline and optical qualities.

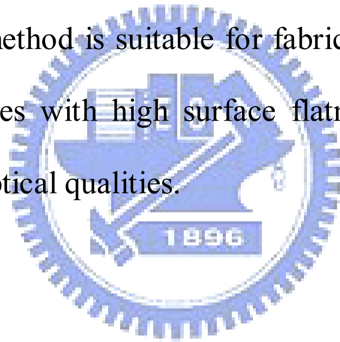

References

[1] Lim, J. H.; Kang, C. K.; Kim, K. K.; Park, I. K.; Hwang, D. K.; Park, S. J., Adv. Mater. 2006, 18, 2720-2724.

[2] Jiao, S. J.; Zhang, Z. Z.; Lu, Y. M.; Shen, D. Z.; Yao, B.; Zhang, J. Y.; Li, B. H.; Zhao, D. X.; Fan, X. W.; Tang, Z. K., Appl. Phys. Lett. 2006, 88, 031911

[3] Lee, J. W.; Kim, J. H.; Han, S. K.; Hong, S. K.; Lee, J. Y.; Hong, S. I.; Yao, T., J. Cryst. Growth 2010, 312, 238–244.

[4] Cagin, E.; Yang, J.; Wang, W.; Phillips, J. D.; Hong, S. K.; Lee, J. W.; Lee, J. Y., Appl. Phys. Lett. 2008, 92, 233505.

[5] Chauveau, J. M.; Vennégués, P.; Laüegt, M.; Deparis, C.; Zuniga-Perez, J.; Morhain,

C., J. Appl. Phys. 2008, 104, 073535.

[6] Kim, J. H.; Han, S. K.; Hong, S. I.; Hong, S. K.; Lee, J. W.; Lee, J. Y.; Song, J. H.; Park, J. S.; Yao, T., J. Vac. Sci. Technol. B 2009, 27, 1625–1630.

[7] Moriyama, T.; Fujita, S., Jpn. J. Appl. Phys. 2005, 44, 7919– 7921.

[8] Chou, M. M. C.; Chang, L.; Chung, H. Y.; Huang, T. H.; Wu, J. J.; Chen, C. W., J. Cryst. Growth 2007, 308, 412–416.

[9] Ho, Y. T.; Wang, W. L.; Peng, C. Y.; Chen, W. C.; Liang, M. H.; Tian, J. S.; Chang, L., Thin Solid Films 2010, 518, 2988–2991.

[10] Wang, W. L.; Ho, Y. T.; Chiu, K. A.; Peng, C. Y.; Chang, L., J. Cryst. Growth 2010, 312, 1179–1182.

[11] Hiroaki Matsui; Hitoshi Tabata, J. Appl. Phys. 2006, 99, 124307.

[12] Ku, C. S.; Lee, H. Y.; Huang, J. M.; Lin, C. M., Cryst. Growth Des. 2010, 10, 1460–1463.

[13] Liu, W.-R.; Hsieh, W. F.; Hsu, C.-H.; Liang, S. K.; Chien, F. S.-S., J. Appl. Cryst. 2007, 40, 924

[14] Narayan, J.; Larson, B. C., J. Appl. Phys. 2003, 93, 278

[15] Zúñiga-Pérez, J.; Muñoz-Sanjosé, V.; Palacios-Lidón, E.; Colchero, J., Appl. Phys. Lett. 2006, 88, 261912.

[16] Yang, S.; Lin, B. H.; Liu, W. R.; Lin, J. H.; Chang, C. S.; Hsu, C. H.; Hsieh, W. F., Cryst. Growth Des. 2009, 9, 5184–5189.

[17] Hamby, D. W.; Lucca, D. A.; Klopfstein, M. J.; Cantwell, G., J. Appl. Phys. 2003, 93, 3214.

[18] Schirra, M.; Schneider, R. ; Reiser, A. ; Prinz, G. M. ; Feneberg, M. ;Biskupek, J. ; Kaiser, U. ; Krill, C. E. ; Thonke, K. ; Sauer, R., Phys. Rev. B 2008, 77, 125215.

[19] Stampfl, C.; Van de Walle, Chris G., Phys. Rev. B 1998, 57, R15052.

[20] Yang, S.; Kuo, C. C.; Liu, W.-R.; Lin, B. H.; Hsu, H. C.; Hsu, C.-H.; Hsieh, W. F., Appl. Phys. Lett. 2012, 100, 101907.

[21] Chichibu, S. F.; Onuma, T.; Kubota, M.; Uedono, A., J. Appl. Phys. 2006, 99, 093505.

[22] Puurunen, R. L., J. Appl. Phys. 2005, 97, 121301.

[23] B. H. Lin, W.-R. Liu, C. Y. Lin, S. T. Hsu, S. Yang, C. C. Kuo, C.-H. Hsu, W. F. Hsieh, F. S.-S. Chien, and C. S. Chang, Appl. Mater. Inter. 2012, 4, 5333

Chapter 6 Recombination Dynamics of Localized Exciton in Basal Stacking Faults

The photoluminescence properties of ZnO are influenced by the structural defects such as impurities, dislocations and basal stacking faults (BSFs). In the non-polar wurtzite ZnO layer, BSFs are usually the dominating defect. Through *ab initio* calculation, BSF having zinc-blend lattice structure is predicted to result in the band profile of type-II quantum-wells (QWs) embedded in wurtzite ZnO. [1] Through the researches, such QWs are considered to bind electrons and to form the emitting band called the BSF-bound excitons, and such emitting band is observed to have higher power-law-value than the one resulted from free-exciton (FX) or donor-bound-exciton (D^0X). [2-6] However, the detail of emitting mechanism resulted from the BSFs is still unclear and need more research. In this chapter, we investigate the transition mechanism of the BSFs in the ALD-grown *m*-plane ZnO layer with post annealing at 600 °C for 1.5 hr by performing time-resolved photoluminescence (TR-PL) and the time-integrated PL (TI-PL) measurements under different temperature and excitation power. For the PL measurements the third harmonic (λ_{exc} = 266 nm) from a Ti:sapphire femtosecond pulsed laser (pulse length 150 fs) was employed. The PL transient spectra were detected by a UV sensitive Hamamatsu streak camera system with a temporal resolution better than 20 ps.

6.1 Temperature Dependent and Power Dependent Photoluminescence

In Chapter 5, we have confirmed that the annealed *m*-plane ZnO layers have BSFs as dominate defect with density of ~10^6 cm^{-1}. The TI-PL spectra of the sample are measured at temperature 5 K with excitation power from 10 to 1020 μW, which are shown in Fig. 6-1(a). The strong emission at ~3.32 eV marked by "BSF" means the emission resulted from the BSFs, and the emission at ~3.37 eV marked by "NBE" is attributed to the near-band-edge emission bands consisting of D^0X and FX. We depict BSF and NBE emission intensities (I) with different excitation power (P) in Fig. 6-1(b).

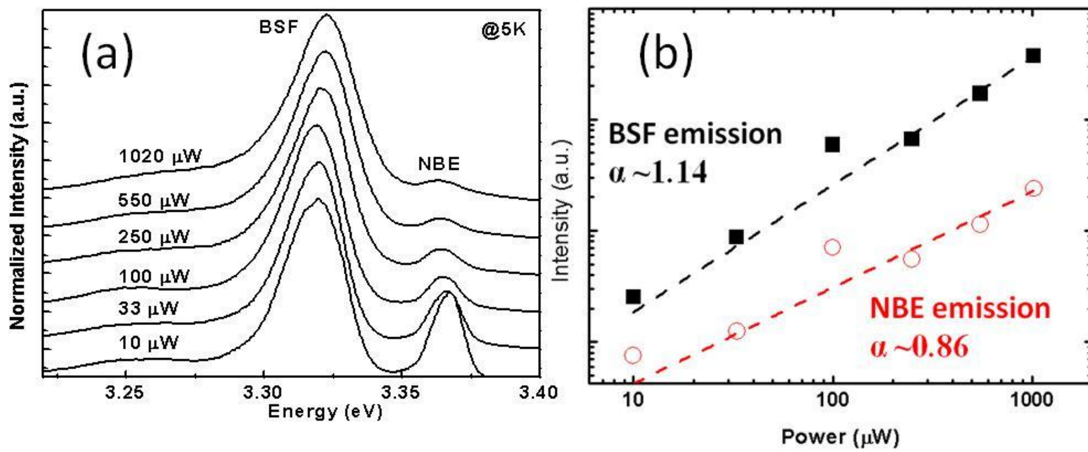

Fig. 6-1 The power dependent TI-PL spectra recorded at 5 K of (a) the ZnO film grown by ALD and annealed at 600°C and (b) the intensity versus the excitation power of the BSF and NBE emissions. The dash lines represent the results of the power-law fitting work.

The NBE and BSF emissions nicely follow the power law: $I \propto P^{\alpha}$ with $\alpha = 0.86$ and 1.14, respectively. For free exciton or bound-exciton emissions, the exponent α should fall in the range of $1 \leqq \alpha \leqq 2$, whereas for the DAP transitions, α should be less than 1. [7]

The value α of the NBE emission slightly less than the normal range is possible due to the influence of the BSFs of high density; the localization ststes of BSFs are considered to interfere with the NBE states. By considering the QWs structure formed by the BSFs, such interference could be attributed to the competition of excited carriers trapping by the BSFs over the NBE states that result in the α value of the BSF emission than for the NBE emission.

The TI-PL spectra measured at the temperature ranging from 10 to 200 K were shown in Fig. 6-2(a) at fixed excitation power 100 μW. The NBE emission is consisted of emissions from the donor bound exciton (D^oX, marked by hollow red circles) and free exciton (FX, solid red circles), and the peak energy marked by solid black circles indicates the BSF emission band.

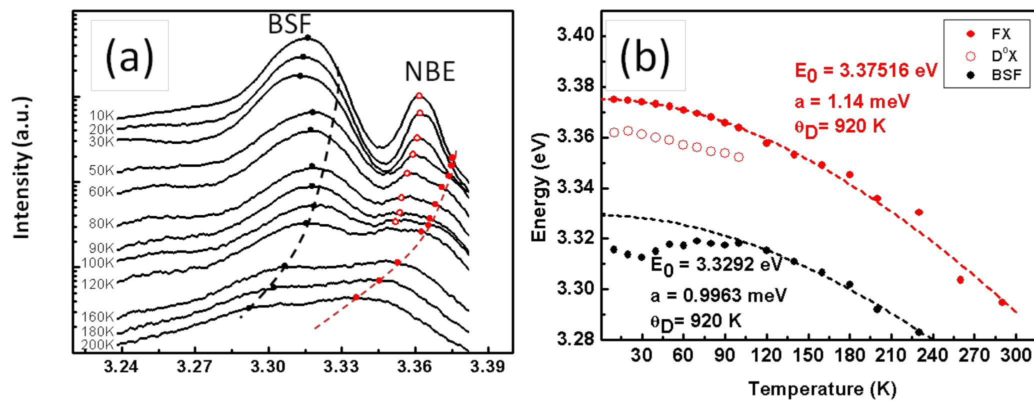

Fig. 6-2 The temperature dependent TI-PL spectra of (a) the ZnO film taken between 10 and 200 K, (b) the energy versus temperature plot of the BSF and NBE emissions. The dash lines depict the fitting results to the Varshni's law.

By fitting the temperature dependent peak energies of the BSF and NBE emission bands to the Varshni's formula in Figure 6-2(b), we determined the transition energy of FX (red dash line) at 0 K is about 3.375 eV. The FX tends to be bounded by donor to be

bounded by donor to form D^oX below 100 K that is consistent with the previous obsverations. [8-10] On the other hand, we obtained the zero-temperature transition energy from the BSFs to be about 3.329 eV by fitting the Varshni's formula to the BSF emission band for T > 100 K (black dash line in Fig. 6-2(b)). However, the observed peak energy of the BSF emission band at 10 K is about 3.315 eV, revealing localized behavior with localization energy of about 14 meV. Furthermore, the BSF emission red-shifts from 3.315 toward 3.313 eV as the temperature increases from 10 to 30 K. It blue-shifts toward 3.319 eV as further increasing temperature to 100 K, then red-shifts again following the Varshni's formula toward the higher temperature. Such "S-shape" behavior is usually observed in the heterostructure multiple QWs and the compound semiconductors attributed to the bounded excitons in the materials due to the potential fluctuation. [2,4,11]

6.2 Time-Resolved Photoluminescence

In order to investigate the localization effect of the BSFs, we compared the dynamics of radiative recombination of the BSFs and NBE through the TR-PL experiments. The TR-PL spectra monitored at temperature of 10 K excited at average power of 100 μW are shown in Fig. 6-3. The spectra are captured for every 6 ps interval and integrated for time interval of 6 ps after a pulse excitation.

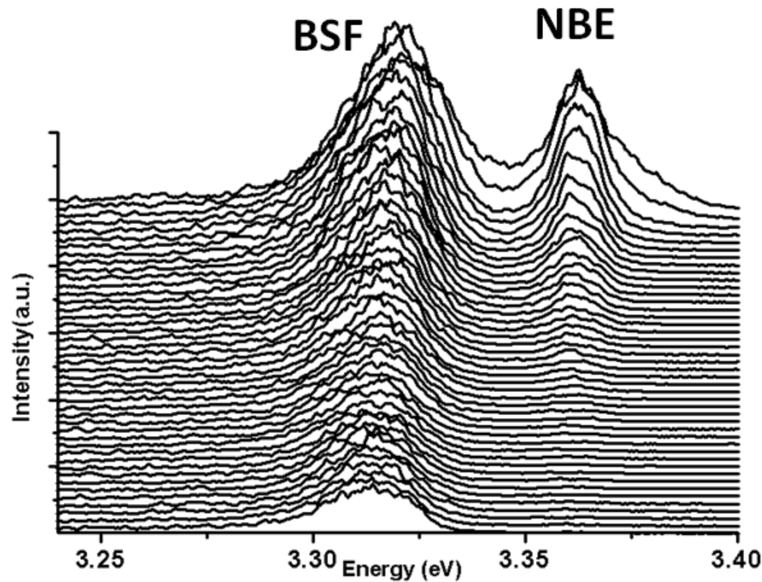

Fig. 6-3 The TR-PL spectra at temperature 10 K with excitation power of 100 μW, and each curve is integrated with time interval of 6 ps after pulsed excitation.

We integrate the intensity in the energy range of 3.280 to 3.345 eV for the BSF emission and 3.345 to 3.397 eV for the NBE emission and plot them as a function of time in Fig. 6-4. By fitting with a single exponential decay, we determine the decay time to be ~60 and ~700 ps for the BSF and NBE emission, respectively. Furthermore, the energy peak of the BSF emission shifts from 3.322 eV toward 3.315 eV in 270 ps after pulse excitation while that of the NBE emission retains at about 3.362 eV. Such observation implies the migration behavior of the BSF-bound excitons through relaxation to lower energy states via phonon scattering and/or tunneling effect. [12] Similar phenomenon are also reported in ZnCdO alloys [13] and InGaN QWs. [14]

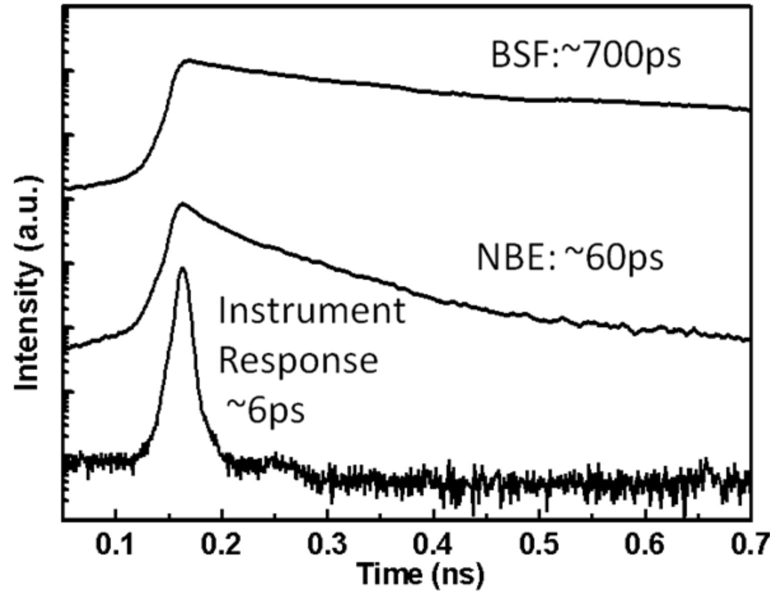

Fig. 6-4 The decay curves of the intensity integrated from the BSF and NBE emissions in energy ranges of 3.280 ~ 3.345 eV and 3.345 ~ 3.397 eV, respectively. The decay curve at the bottom is the response of the Instrument.

6.3 Spectral Dependent Decay Times

Fig. 6-5 presents the PL decay times as the different monitored emission energies with the corresponding TI-PL spectra (solid curves). We found in Fig. 6-5 (a) that the decay time of the BSF emission measured at 5 K and 100 μW excitation monotonically decreases with increasing monitored emission photon energy over an energy range 60 meV in 3.28~3.34 eV; but almost a constant decay time is over the energy range of the NBE emission. Because the migration only occurs in the BSFs but not in W-ZnO matrix, we can rule out the localization effect caused by the alloy fluctuation [13] as shown in Fig. 6-6 in the ternary alloy like $Mg_xZn_{1-x}O$. [17] Besides, for the nature, the thickness of the

BSF formed zincblende ZnO layer is fixed at about 1.5 *c*-axis lattice constant of the wurtzite ZnO preventing the width or depth fluctuation of the QWs. [15]

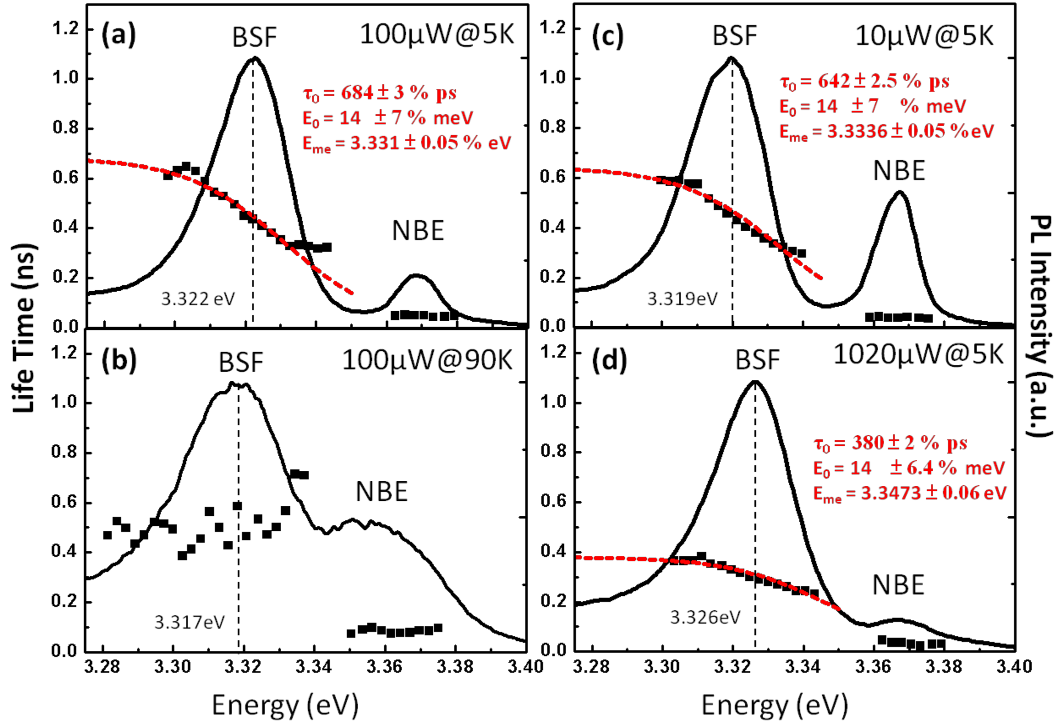

Fig. 6-5 The spectra dependent decay times are the plots with the same excitation power 100μW at different temperature (a) 5 and (b) 90 K, and with different excitation power (c) 10 and (d) 1020 μW at the same temperature 5 K.

The shorter decay time on the high-energy side of BSF emission suggests contribution from nonradiative relaxation or trapping through some decay channels to the localized states should have occurred in BSF regions. We therefore fit the observed lifetime $\tau(E)$ to the following expression to take the nonradiative decay into account, [12]

$$\tau(E) = \frac{\tau_r}{1 + \exp[(E - E_{me}) / E_0]},$$

where $_{r}$ is the radiative lifetime, E_0 represents the characteristic energy of relaxation, which is set equal to the trapping energy of 14 meV obtained from the temperature dependent TI-PL, and E_{me} is the definite energy, which plays a role analogous to a mobility edge. Best fit to Fig. 6-5(a) we obtained as τ_r = ~684 ps and E_{me} = ~3.331 eV. The localized excitons are considered to nonradiatively transfer from the high-energy localized states to the low-energy trapped states through the exciton-phonon interaction and/or the tunneling among QWs. [12] However, as raising temperature to 90 K, we observed decreasing influence of the nonradiative localized states transfer in BSFs with almost constant decay times of the monitored photon energy. Such a the result implies that the localized BSF-bound excitons become untrapped by thermal excitation.

We also performed the TR-PL under 10μW and 1020μW excitation powers at 5K and plotted the decay times versus the photon energy in Figs. 6-5(c) and (d). The best fitting results yield τ_r = ~643 ps (~ 380 ps) and E_{me} = ~3.334 eV (~3.347 eV) with fixed E_0 = 14 meV for excitation power of 10 μW (1020 μW). The shorter decay time τ_r or the faster decay rate for increasing excitation power implies the nonlinear exciton-exciton scattering of high-density may have occurred. The high-density carriers should lead to the screening effect to eliminate the band tilting and to cause blue shift of the energy peak in the BSF emission in Fig. 6-5 (c), (a) and (d) as increasing the excitation power. The band profile of the QWs structure grown along the polar axis should have been tilted by the internal electric field that increases the spatial separation between the wave functions of electron and hole along the growth direction. Such spatial separation decreases the overlap of the wave functions of electron and hole thus increases the decay time of the excitons. Besides, the band-tilting effect also decreases the band gap to red shift the

emission peak energy. The high-density carriers at high excitation power result in screening the internal electric field to reduce the band-tilting effect in turn to increase the band gap that leads the blue shift of the recombination energy of excitons in the QWs.

On the other hand, the multi-QWs are considered to form the mini-band while the width of the barriers is small enough to result in the wave function overlapping, and the excitons bound in the QWs are considered to migrate among the mini-bands. [19]

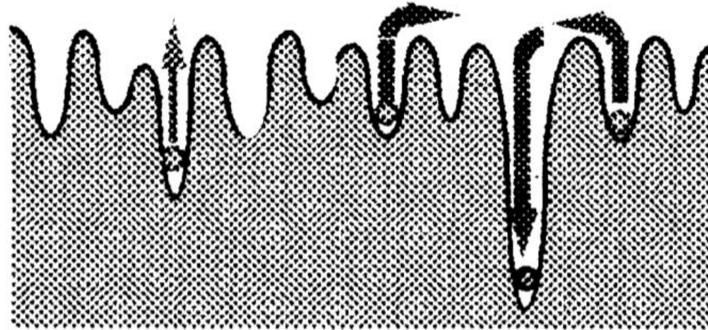

Fig. 6-6 The potential fluctuation due to the fluctuation of alloy density. [17]

From the TEM results, the BSFs distributed in the crystal with the minimum spatial interval about 3 nm are extremely difficult to form the periodical QWs structures for the mini-band, but probably lead to the overlap of electron wave function among the QWs. [2] Such overlap of the wave functions could result from the coupled QWs structures and the localization effect could result from the quantum coupling the BSF-bound excitons among the randomly distributed separation of QWs. [18] As show in Fig. 6-7(a) we take the numerical calculation of the symmetrical double QWs of zinc blend ZnO/wurtzite ZnO as an example, which has the potential barrier width of 3 nm and well width of 0.8 nm. The potential profile is sketched by black line, in which the wave functions of the electrons overlap to lead the interaction due to the Pauli exclusion principle and to split the energy

levels into a lower (E_1) and a higher (E_2) energy levels. As the result of the interaction, the wave function profiles of lower and higher energy levels are also sketched out by Psi_1 and Psi_2. As the potential barrier of the double QWs structure decreases, the energy gap between E_1 and E_2 increase as shown in Fig. 6-7(b), which shows the energy levels E_1 and E_2 varying as the central barrier widths ranging from 1 to 15 nm. Such a result reveals the reasonability of that the localization effect results from the quantum coupling effect of the BSF-bound electrons among with the random potential barrier thickness.

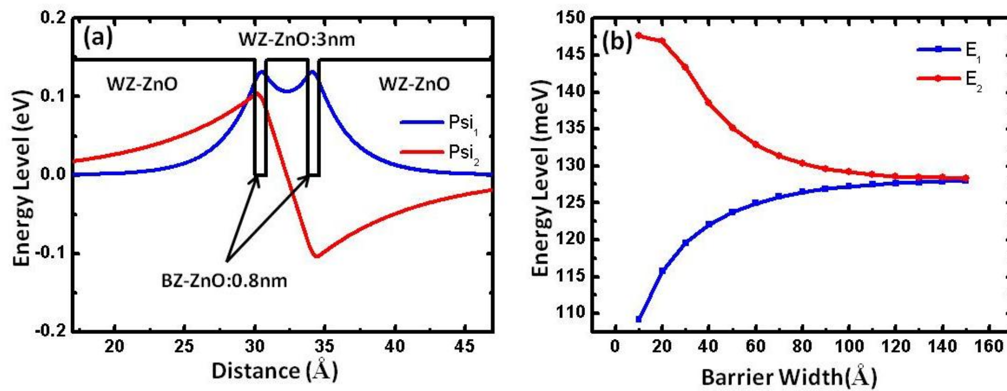

Fig. 6-7 The wave functions of the lowest two energy levels of the symmetric QWs with a central barrier width of 3 nm (a), and the confinement energies of the lowest two states as function of the central barrier width (b).

From the TEM images, the average distance among the BSFs is roughly estimated as ~5 nm and leads to the energy level splitting for ~12 meV as shown in Fig. 6-7(b), which is very close to the trapping energy of ~14 meV obtained from the temperature dependent PL spectra. It reveals that these localization states could be resulted from the QW coupling effect.

The localization effect of such BSF-bound excitons was observed in the materials of wurtzite structure with acceptor doping treatment; it results from the trapping of excitons to the acceptor located in the vicinity of BSF. [16] Obviously, the acceptor trapping can be

excluded in this undoped ZnO film. However, similar to the donor in the vicinity of the I_1-type BSF for the GaN material to cause the band profile tilting as shown in Fig. 6-8 [15], the band profile tilting caused by the donor could occur in our samples. Based on the results of the theoretical calculation [15], the binding energy is about 46 meV for the donor located at far away from the BSF planes; it increase as reducing the distance between the donor and the BSF. The binding energy is calculated to be 73 and 58 meV for the distance of 2.5 and 7.5 nm, respectively. The donors distributed randomly in ZnO film could form local carrier traps with distributed binding energies to capture excitons similar to the situation of donor bound excitons, D^oX. However, determined by the Hall measurement, our annealed *m*-plane ZnO film is n-type with carrier density of ~$5x10^{16}$ cm^{-3} from which the average distance among the donors is roughly estimated as ~27 nm. Such carrier density of the donors could not have enough contribution on forming localization states to be observed.

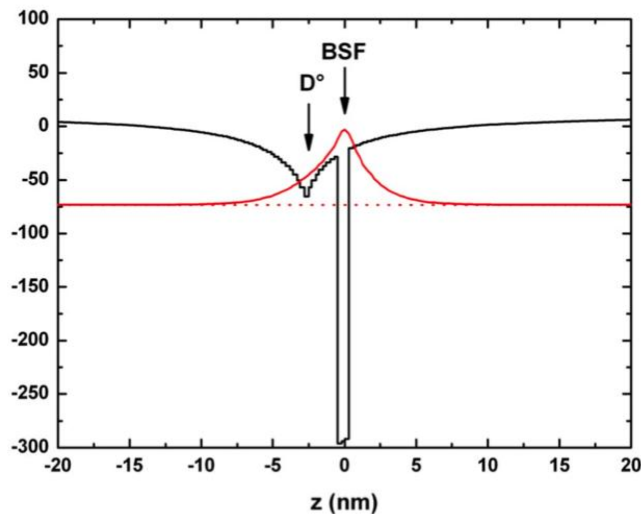

Fig. 6-8 Band profiles (black curve), electron envelope functions (red curve) and energy (dotted red line) for electron confined on a D^0-BSF complex with distance d of 2.5 nm between donor and BSF plane. [15]

6.4 Conclusion

In conclusion, we have used the TR-PL technique to explore the dynamic recombination of the BSF emissions. The results reveal the migration behavior of the BSF-bound excitons toward the localization states with lower energy. Such localization states are attributed to the quantum coupling effect among the various separations of BSFs. The migration of the BSF-bound excitons among the localization states could be attributed to the exciton-phonon interaction and/or the tunneling effect. Furthermore, through the TR-PL spectra with high excitation power, the screening effect is observed in the type-II QWs formed by the BSFs.

References

[1] Y. Yan, G. M. Dalpian, M. M. Al-Jassim, S.-H. Wei, Phys. Rev. B. 70, 193206 (2004).

[2] S. Yang, C. C. Kuo, W.-R. Liu, B. H. Lin, H.-C. Hsu, C. H. Hsu, and W. F. Hsieh, *Appl. Phys. Lett.* 100, 101907 (2012)

[3]W. Rieger, R. Dimitrov, D. Brunner, E. Rohrer, O. Ambacher, M. Stutzmann, *Phys. Rev. B.* 54, 17596 (1996)

[4] P. Corfdir, P. Lefebvre, J. Levrat, A. Dussaigne, J.-D. Ganiere, D Martin, J. Ristic, T. Zhu, N. Grandjean, and B. Deveaud-Pledran, *J. Appl. Phys.* 105, 043102 (2009)

[5] Y. J. Sun, O. Brandt, U. Jahn, T. Y. Liu, A. Trampert, S. Cronenberg, S. Dhar, K. H. Ploog, *J. Appl. Phys.* 92, 5714 (2002).

[6] P. P. Paskov, R. Schifano, B. Monemar, T. Paskova, S. Figge, D. Hommel, *J. Appl. Phys.* 98, 093519 (2005).

[7] T. Schmidt, K. Lischka, and W. Zulehner, Phys. Rev. B. 45, 8989 (1992)

[8] V. A. Fonoberov, K. A. Alim, A. A. Balandin, F. Xiu, J. Liu, *Phys. Rev. B.* 73, 165317 (2006)

[9] D. W. Hamby, D. A. Lucca, M. J. Klopfstein, G. Cantwell, *J. Appl. Phys.* 93, 3214 (2003)

[10] D. C. Look, D. C. Reynolds, J. R. Sizelove, R. L. Jones, C. W. Litton, G. Cantwell, W. C. Harsch, *Solid State Commun.* 105, 399 (1998)

[11] Y. H. Cho, G. H. Gainer, A. J. Fischer, J. J. Song, S. Keller, U. K. Mishra, and S. P. DenBaars, *Appl. Phys. Lett.* 73, 1370(1998)

[12] C. Gourdon, and P. Lavallard, Phys. Stat. Sol. 153, 641 (1989)

[13] I. A. Buyanova, J. P. Bergman, G. Pozina, W. M. Chen, S. Rawal, D. P. Norton, S. J.

Pearton, A. Osinsky, and J. W. Dong, *Appl. Phys. Lett.* 90, 261907 (2007)

[14] Y. Narukawa, Y. Kawakami, S. Fujita, and S. Fujita, *Phys. Rev. B* 55, R1938 (1997)

[15] P. Corfider, P. Lefebvre, J. Ristić, J.-D. Ganière, and B. Deveaud-Plédran, *Phys. Rev. B.* 80, 153309 (2009)

[16] S. Khromov, C. G. Hemmingsson, H. Amano, B. Monemar, L. Hultman, and G. Pozina, *Phys. Rev. B.* 84, 075324 (2011)

[17] Y. Kishimoto, Y. Shiraki, and S. Fukatsu, Thin Solid Films 321, 81 (1998)

[18] Paul Harrison, *Quantum Wells, Wires and Dots: Theoretical and Computational Physics*, New York : John Wiley & Sons (2000)

[19] J. Y. Jen, J. R. Anderson, M. Gorska, *J. Appl. Phys.* 102, 053518 (2007)

Chapter 7 Conclusions and Prospective

7.1 Conclusions

The ALD method shows the success on growing the epitaxial ZnO layers on sapphire substrates. Using *c*-plane sapphire as substrate the ZnO films are grown with *c*-plane orientation and in-plane epitaxial relationship of $\{10\bar{1}0\}_{ZnO} \parallel \{10\bar{1}0\}_{Al_2O_3}$, un-twisted orientation. On *m*-plane sapphire the ALD grown ZnO layers are confirmed to be single crystallographic *m*-plane orientation with epitaxial relationship of $(10\bar{1}0) < 0001 >_{ZnO} \parallel (10\bar{1}0) < \bar{1}2\bar{1}0 >_{Al_2O_3}$. Such a result is attributed to the nearly perfect domain matching across the ZnO/sapphire interface along the $[1\bar{2}10]_{ZnO}$ direction. The thermal annealing treatment exhibits drastic improvement on the crystalline quality, and further confirms intrinsic BSFs as the dominant structural defects in these annealed ZnO layers. The density of BSF is identified to be ~1.0×10^6 cm^{-1}. Comparing to the PLD grown ZnO layers with the threading dislocations as predominant defects, such diversity in the dominant type of structural defects is attributed to the fundamental difference in the growth mechanisms of the two methods. Through the TEM analysis the mis-orientation grains are found in the as-grown *c*-plane ZnO layers and eliminated after the thermal annealing treatment, which leads to the voids at the surface. Such kinds of grains are not found in the as-grown *m*-plane ZnO layers, whose surface roughness decreases after thermal annealing treatment. The difference between the as-grown *c*- and *m*-plane ZnO layers is considered to result from the domain matching epitaxy.

Each BSF in ZnO has the zinc blend structure sandwiched by the wurtzite barriers

and leads to the energy band alignment of type-II quantum-well that results in in-direct excitons consisting of electron in the QW and hole at the vicinity of barrier. From the low-temperature PL spectra of the ZnO layers, the dominant emission centered at ~3.321 eV is ascribed to the transition associated with the BSF-bounded excitons (~3.34 eV) which also further be trapped by the localization states resulted from the local defects and/or the wave function of electrons coupling between bundled BSF quantum wells at low temperature. The transferring of the BSFs-bound excitons among these localization states are observed, which is attributed to the exciton-phonon interaction and/or the tunneling effect, and the thermal energy is able to frustrate the localization effect. Through the TR-PL spectra with high excitation power, the screening effect is observed in the type-II QWs formed by the BSFs.

In these researches, the ALD method shows the features of low temperature growth, high uniformity of large area, thickness controlling in atom scale, high surface flatness, and epitaxial layer growth. These as-grown ZnO layers reveal the residual organic functional groups, which are attributed to the un-completely chemical reaction and able to be eliminated by the thermal annealing treatment with temperature above 400 ^{o}C. Such residual organic functional groups could be the restriction of following fabrication of structures.

1896

7.2 Prospective

So far, the research of the ZnO material has accumulated much research, and based on ZnO material modulating the electronic and optical properties of the material has been also attracting more and more research attention. However, the reports about using ALD to modulate the properties of ZnO material are still rare. The deposition with sequential self-terminating chemical reactions is reasonably considered to be able to deposit the layers of different materials layer-by-layer along growing direction, which is different from the traditional high vacuum deposition technique. Based on these features of ALD, the multi-layer structure consisting of different materials with specific design on thickness and periodicity is expected. Hence, the ALD technique is going to be used for depositing the superlattice structure consists of the ZnO material and other oxide material. By taking the advantage of the thermal annealing technique the alloy material based on ZnO with high concentration which is difficultly obtained through the traditional ways are expected to be fabricated by the ALD.

The observation of the BSFs reveals some attracting emitting properties, which probably belong to the ZB ZnO. The properties of the ZB ZnO could be observed indirectly by taking advantage of the BSFs, but the efficient way for fabricating ZB ZnO layer is still lack. The ALD is expected to fabricate the ZB ZnO layers by using specific substrate such as the ZnS.